VISUALIZATION AND ANALYSIS OF A CONVECTIVE FIELD USING THE SCHLIEREN TECHNIQUE
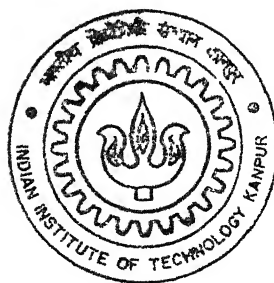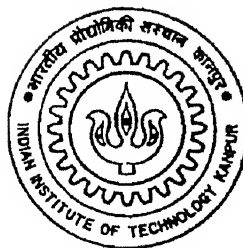
By

Atanu Phukan

DEPARTMENT OF MECHANICAL ENGINEERING

Indian Institute of Technology Kanpur

MARCH, 2003

VISUALIZATION AND ANALYSIS OF A CONVECTIVE FIELD USING THE SCHLIEREN TECHNIQUE

by

Atanu Phukan

DEPARTMENT OF MECHANICAL ENGINEERING
INDIAN INSTITUTE OF TECHNOLOGY KANPUR
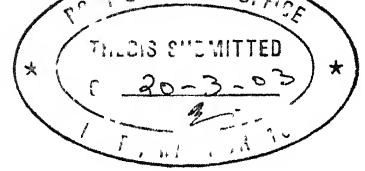March 2003

CERTIFICATE

It is certified that the work contained in the thesis entitled "*Visualization and Analysis of a Convective Field Using the Schlieren Technique*", by **Mr. Atanu Phukan**, has been carried out under our supervision and that this work has not been submitted elsewhere for a degree

K Muralidhar
Professor
Dept of Mechanical Engineering
I I T Kanpur 208016

P K Panigrahi
Asst Professor
Dept of Mechanical Engineering
I I T Kanpur 208016

March, 2003

Dedicated To

my loving MOM and caring DAD
whose constant inspiration and support has enabled me to give the
best out of me.

Abstract

The schlieren technique as both qualitative and quantitative tool for temperature and concentration measurement has been evaluated in this work. Both monochrome laser schlieren and colour schlieren have been implemented and compared with each other. The Rayleigh-Benard convection in a rectangular cavity and the transport phenomena during crystal growth from aqueous solution have been studied. The schlieren technique has been compared with similar optical techniques i e, interferometry and shadowgraph. The numerical simulation has also been carried out to compare with the experiments and provide additional insight about the physics of the problem. The simultaneous comparison of refractive index based technique i e interferometry, schlieren and shadowgraph has not been carried out in the earlier studies. The schlieren technique has primarily been used as a qualitative tool. The development and implementation of quantitative schlieren technique is the primary focus of this work.

For Rayleigh-Benard convection study, a rectangular cavity of 32 16 mm square cross-section and 447 mm length has been used. Both air and water have been used as the working fluid. For air, the Rayleigh number during the experiments are $1\ 40 \times 10^4$, $2\ 70 \times 10^4$, $5\ 10 \times 10^4$, $8\ 50 \times 10^4$, $1\ 13 \times 10^5$ and $1\ 40 \times 10^5$ and for water, the Rayleigh numbers are $2\ 50 \times 10^6$, $4\ 40 \times 10^6$, $2\ 50 \times 10^6$, $2\ 50 \times 10^6$, $2\ 50 \times 10^6$ and $2\ 50 \times 10^6$. Both steady and unsteady convection have been studied. Interferometry has been used more extensively for quantitative analysis. But, its applicability is limited to the strength of the gradient of the scalar field being measured. The schlieren technique has the potential to be a superior toll for high gradient application. However, the accuracy of quantitative schlieren has not been compared till to date which can be evaluated at some intermediate gradient situation when both interferometry and schlieren can be accurate and sensitive. The temperature field during convection in the rectangular cavity could be con-

trolled such that the applicability of both interferometry and schlieren technique is established The accurate comparison between schlieren, interferometry, shadowgraph and numerical simulation has established the success of the schlieren as a quantitative tool The one dimensional colour filter has been developed at different sizes for colour schlieren experiments It is observed that in colour schlieren a wider ranger of resolution is achievable in comparison to that of the monochrome schlieren The diffraction affects are absent in colour schlieren and the temperature boundary layer information can be extracted in a greater detail then the monochrome schlieren The detail flow features can be extracted by suitably adjusting the colour filter and the hardware during the experiments

The quality of crystals obtained from the aqueous solution is dependent on the transport phenomena present during the crystal growth process The growth rate of the crystal is driven by the concentration gradient and therefore the characterization of the concentration boundary layer characteristics is very important during the crystal growth process The schlieren technique has been implemented and tested for the measurement of concentration field during the crystal growth process The relationship between the crystal quality and the concentration profile has been established

Acknowledgement

Contents

Contents

List of Figures

List of Tables

Nomenclature

g	Accelaration due to gravity
h	Height of the cavity
L	Distance traversed by the laser beam through the test cell
n	Refractive index of the fluid
n_o	Reference value of refractive index
ρ	Density of fluid
ρ_o	Reference value of density
ν	Kinematic viscosity
μ	Dynamic viscosity
a_0, b_0	Source dimensions
a_K	Unobstructed light
β	Thermal expansion coefficient
α_T	Thermal diffusivity
α_C	Concentration densification coefficient
T	Temperature
C	Concentration
K	Mass transfer coefficient
D	Diffusion coefficient
N	Flux into the crystal
d	Fraction supersaturation
F	Volume fraction of solute at crystal surface
f	Focal length of lens
ε	Beam deflection angle

Co	Contrast
Gl	Gladstone-Dale constant
H	Hue
S	Saturation
I	Intensity
R,G,B	Red, blue and green components of a coloured image
Nu	Nusselt number
Pr	Prandtl number of the fluid, (ν/α_T)
Ra	Rayleigh number
Sh	Sherwood number
Gr	Grashoff number

Chapter 1

Introduction

Optical measurement techniques have received increased attention in recent years and continue to gain importance in many new fields of application. The rapid improvement in data storing, processing, laser and semiconductor technology contributes to the fast development of optical techniques. Owing to the fact that these techniques are non-intrusive in nature and practically inertia free, the scanning of the cross-section of the region under study generates a large volume of information with no time delay. In a broader sense, the optical techniques that are used in the measurement of flow can be classified into three main categories: (1) direct visualization methods, (2) scattering methods, and (3) index of refraction method.

In direct visualization methods, some type of marker is followed along with the fluid motion. Many substances have been used to visualize the flow of transparent medium like air and water. Smoke, helium bubbles, dust particles, and even glowing iron particles have been used in air, a variety of dyes, particles, neutrally buoyant spheres, and both air and hydrogen bubbles have been employed in water. Streamlines, streaklines, and pathlines are the three curves that describes the flow of a fluid and they can be directly visualized for a flow field

Light scattering is the physical process involving the interaction of light with matter. Due to this interaction, the light incident is partially deflected in directions deviating from the incident direction. In some scattering process, in

addition to change in direction there is also change in frequency The evolution of the scattered light with respect to its intensity and its wavelength often yields valuable information regarding the properties of the scattering matter Thus in the light scattering methods, the scattered light is used in the evaluation of the flow parameters The techniques based on light scattering are (1) laser Doppler-Velocimetry (LDV), (2) particle image-velocimetry (PIV), (3) spontaneous Raman scattering, (4) coherent antistokes Raman spectometry (CARS), (5) absorption spectometry, (6) laser induced-fluorescence (LIF), and liquid crystal thermography (LCT)

In the present study, the refractive index based optical methods have been employed to visualize the thermal and concentration fields In this method, the index of refraction or a spatial derivative of the index of refraction of a medium is measured and from this the properties of the flow are determined. Here the image formation depends on the effects of the refractive index changes on the transmission of the light Although all the three methods depend on variation of the index of refraction in a transparent medium, the quantities measured with each one are quite different Shadowgraph, where the reduction in light intensity on beam divergence is employed, indicates the variation of second derivative (normal to the light beam) of the index of refraction Schlieren , where the light deflection in a variable refractive-index field is captured, indicates the first derivative of the index of refraction (in a direction normal to the light beam) Interferometry, where the image formation is related to the changes in the refractive index with respect to a reference environment, respond directly to the differences in the optical path lengths and gives the index of refraction field within the flow The sensitivities of these three methods are quite different, so they can be used to study a wide variety of systems Thus interferometry is employed to study flows in which density gradients are small, while schlieren and shadowgraph find applications where large density gradients are present in the flow field Since the three optical techniques give the path integral of the information present in the region under study, they are well suited to the measurements in two-dimensional fields, where there is predominantly no change in refractive index of the flow field along the light beam. Of the three methods, the one, which has been used extensively for quantitative measurements is the interferometer Till now the main

use of schlieren and shadowgraph have been to show the position and shapes of the regions of density changes such as those occurring in high speed flows, mixing problems and problems of free and forced convection

1.1   Scope of the Work

Increasing possibilities of computer-aided data processing have caused a new revival of optical techniques in many areas of mechanical and chemical engineering for heat and mass transfer, and fluid dynamics analysis Global experimental information is not sufficient for developing constitutive equations to describe complicated phenomena in fluid dynamics or in transfer process by a computer program Furthermore, a detailed insight with high local and temporal resolution into the thermo- and fluid dynamic situations is necessary

For reliable prediction of the heat transfer, the velocity and temperature field in the boundary layer must be known, or a physically realistic and widely valid correlation describing the turbulence must be available Also, for a better understanding of combustion process it is necessary to know the local concentration and temperature just ahead of the flame and in the ignition zone   Here optical measuring technique provide comprehensive and detailed information Its results may also supply valuable evidence of the formation of phase interfaces, on particle movement, or on the size distribution of droplet swarms Optical techniques also finds its applications in studying high gradients, shocks and in aerodynamics

In the present work refractive index based optical technique is being employed to study the buoyancy-driven convection field in a rectangular cavity which is of fundamental as well as practical importance Buoyancy-driven convection finds application in various engineering fields ranging from cooling of electronic components to material processing applications The schlieren optical technique was mostly used for qualitative visualization of flow fields In this work quantitative evaluation of the schlieren images is carried out to extract more valuable information. Concentration-driven convection fields are also being studied, with

growth of optical crystals from its aqueous solution, taken as the case of interest
These optical crystals are used for frequency conversion of lasers as well as for
nuclear fusion reactions   It have been tried to determine the conditions under
which large crystals of good quality can be grown

1.2   Literature Review

Optical techniques are used extensively for study of convective field   Out of this,
interferometric studies have been proved more suitable for quantitative analysis
The other two optical techniques namely schlieren and shadowgraph have been
employed for qualitative visualization of convective fields   This study attempts to
evaluate the schlieren technique as a prospect for quantitative analysis   The study
of concentration-driven convection currents during crystal growth using schlieren
optical technique has been attempted   The literature for the schlieren technique,
convection in enclosures and crystal growth phenomena have been reviewed in
the following sections

1.2.1   Schlieren

Schlieren has been used extensively for qualitative visualization of flow field   Mod-
ified schlieren arrangement are being used for quantitative visualization   Moubray
(1967) used the schlieren and shadowgraph techniques in the study of flow pat-
terns in density stratified liquids. Brackenridge (1967) did measurement of ther-
mal distributions near a heated vertical plate and near a horizontal cylinder using
a vertical wire at the focal plane   Davis(1970) applied the schlieren technique in
an axisymmetric subsonic turbulent jet   He related the unsteady flow density
gradients to the variation of light intensity in a schlieren image and presented the
fluctuating density gradient across the jet   He (1972) also reported the density
fluctuations in the supersonic axisymmetric turbulent jet using a single beam
schlieren system and presented the difference in the distribution of fluctuating
density between the supersonic and subsonic jet.

Keifer and Hajdak (1990) reviewed the laser schlieren technique for appli-

cations on determination of the net rate of endothermic reaction and primary dissociation parameters like relaxation times and rates of primary dissociation, etc They discussed the accuracy with which the signal generated by differential detector will reproduce the variation of the refractive index gradient in a reactive shock

Kosugi, Maeno, and Honma (1993) measured the gas temperature profiles in the discharge regions of the excimer laser cavity by laser schlieren method The diffraction of the laser beam due to the motion of discharged hot gas was used to measure the temperature distribution Cook (1993) used an iterative theoretical approach to obtain quantitative density data from the focusing schlieren technique Koreeda et al (1995) experimentally investigated the thickness of shock waves and the density profiles at high Mach numbers (between 16 and 34) by means of the laser schlieren technique While analyzing the schlieren signal, they took into account the detector response, which was crucial in the case of strong shock waves (M>16), as the signal must be obtained in a few micro-second Tanda (1995) studied the thermal field and the heat transfer characteristics of a system consisting of two staggered vertical plates cooled by air in free convection The schlieren system employed here makes use of an opaque filament to identify regions of fluid that deflects light rays by the same amount He (1998) also applied this quantitative schlieren technique to study two-dimensional free convection heat transfer

Kleine et al (1997) developed an microscope for in situ quantitative mapping of solute concentration profiles around growing crystals based on a combination of the schlieren technique and the dark field method After calibration, video recording, digitizing and numerical integration of the image, quantitative and detailed concentration maps were obtained Bystrov et al (1998) presented a new approach to the problem of density reconstruction behind a shock front, where the beam diffaction in the non-uniform medium and the distortion of the signals in electric circuits were taken into account They concluded that their approach has better spatial resolution than traditional beam approach and is suitable to investigate the density distribution in the vicinity of shock front where the characteristic length is considerably small compared to the beam diameter S Fu et

al (1998) presented a novel technique of analysis of velocity distribution of a fluid field using image sequence taken from a schlieren apparatus In contrast to PIV techniques, this technique had the advantage in situations where the tracing particles are difficult to be introduced or identified S Garg et al (1998) obtained quantitative flow-field data of instantaneous density gradient in a two-dimensional shear layer spanning an open cavity with an extension of the schlieren method The technique is based on the measurement of light-intensity fluctuations in a real time schlieren image using a photo detector Bredikhin et al (2000) developed a technique based on the optical schlieren method to investigate in situ the growing crystal morphology under real rapid profiling growth conditions Hikmet (2000) did in situ observation of ion concentration profiles in lithium ion-conducting gels He used an schlieren optical set-up devised by Wimberger (1992) to determine density distributions in poly(carbonate)s Using it, the change in the refractive index across the cell was measured and then translated into concentration values Chaseckkin et al (2001) used different schlieren methods (direct shadow, 'slit-knife','slit-thread','natural rainbow'), characterized by high spacial resolution, for visualization of density gradient field He did experimental investigations of fine and macroscopic structures of density and velocity distributions generated by a towing cylinder or a vertical strip in a linearly stratified liquid carried in a rectangular tank

Recently colour schlieren has been used extensively for qualitative and quantitative visualization Howes (1984) discussed the rainbow schlieren method and its applications in measurement of non uniformities in fluids and transparent solids Non uniformity in fluid included medium with a unidirectional refractive-index distribution, axially symmetric distribution and homogeneous isotropic turbulence In transparent solids, thickness variations, deformation, flatness and artistic effects were discussed Settles (1985) discussed colour-coding schlieren techniques for the optical study of heat and fluid flow The characteristics and advantages of this flow visualization tool were discussed in terms of one- and two-dimensional colour-coding, qualitative and quantitative visualizations, and system sensitivity, range and resolution. Greenberg, Klimek and Buchele (1995) discussed colour schlieren method, where an continuously graded rainbow filter is placed in the back focal plane of the decollimating lens A colour CCD camera

and a video digitizer was used to quantify accurately the colour attributes of the resulting image and hence the associated ray deflections They concluded that the rainbow schlieren deflectometry provides sensitivity comparable with that of conventional interferometry, while being less sensitive to mechanical misalignment Al-Ammar et al (1998) used rainbow schlieren deflectometry technique to measure the oxygen concentrations in an axisymmetric helium jet The concentration distributions were inferred from the schlieren image by taking into account the sampling interval and noise in measurements Excellent quantitative agreement was reached between measurements from schlieren and continuous sampling probe Agrawal et al. (1998) presented quantitative rainbow schlieren deflectometry with tomography for measurements of temperature in 3D gas flows The results agreed quite well with the thermocouple measurements Shenoy, Agrawal, and Gollahalli (1998) computed field distributions of species concentration and temperature of an isothermal helium jet and hydrogen jet diffusion flame and compared quantitatively by inverting the experimental schlieren results Their results demonstrated the effectiveness of the rainbow schlieren technique for validating the CFD models of reacting and non-reacting steady flows in axisymmetric systems Agrawal, Albers and Ariffin (1999) presented an Abel -inversion algorithm to obtain mean and RMS refractive index profiles from deflectrometric measurements in time-dependent flows The algorithm was validated by synthetic data and then applied to investigating an oscillating gas jet diffusion flame Albers and Agrawal (1999) investigated the flow structure of a flickering gas-jet diffusion flame using quantitative rainbow schlieren deflectometry They described the flame structure by mean, root mean square (RMS) and probability density function profiles of temperature Their results showed global oscillations in the flow field of the flame at a frequency varying linearly with the operating pressure

1.2.2   Buoyant Convection in Enclosures

Rayleigh-Benard convection can be defined as the motion of the layer of fluid confined between two infinite horizontal walls heated from below and cooled from above, the side walls of the enclosure being adiabatic. This configuration results in an unstable stratification of the fluid layer with cold heavy fluid on top of the

light hot fluid The fluid layer thus has a natural tendency to readjust towards a stable configuration The driving force responsible for the convective motion is buoyancy The non-dimensional parameter Rayleigh number is the relative measure of the strength of the buoyancy force to viscous force More fundamentally, it is the ratio of the work done by buoyancy in the gravity field to the viscous dissipation The Prandtl number is a second dimensionless quantity arising in thermal convection It is a measure of ratio of the molecular diffusivity of momentum to that of thermal energy and is a fluid property Flow transitions are generally documented in terms of Rayleigh number and Prandtl number The Rayleigh number is defined as

$$\text{Ra} = \frac{g\beta \left(\text{T}_{hot} - \text{T}_{cold}\right)\text{h}^3}{\nu \alpha_T} \tag{1 1}$$

and the Prandtl number

$$\text{Pr} = \frac{\nu}{\alpha_T} \tag{1 2}$$

A large amount of literature is available in the field of Rayleigh-Benard convection in rectangular cavities One of the objective of the published research is to identify the critical Rayleigh number when flow undergoes a transition from one configuration to another The critical Rayleigh number for the onset of convection in an infinite fluid layer does not depend on the Prandtl number of the fluid, whereas all subsequent transitions are strong functions of the Prandtl number The critical Rayleigh number at the onset of convection is dependent on the geometry of the cavity It decreases with the increasing aspect ratio The aspect ratio is defined as the ratio of the horizontal width of the cavity to the vertical depth of the fluid layer It is maximum for an infinite fluid layer

When the Rayleigh number is very close to the critical value for the onset of convection, hexagonal cells have been observed both experimentally and numerically. Numerical studies have shown that for liquids, the fluid particles within the hexagonal cells have an upward motion in the center, while for gases the particles have a downward motion in the center

For an increase in Rayleigh number, the formation of stable two dimensic longitudinal rolls are seen The two dimensional rolls slowly deform to th

dimensional rolls For further increase in the Rayleigh number, adjacent rolls start to merge leading to a reduction in the number of rolls The flow switches to a time-dependent regime at higher Rayleigh numbers and slowly approaches the turbulent state

Experimental studies have shown that in an infinite fluid layer case the first transition from conduction to steady cellular convection occurs at a Rayleigh number $Ra_{c_1} = 1707\ 8$ and this value is independent of the Prandtl number of the fluid considered According to the theoretical work of Davis (1967) and Stork and Muller (1972), Ra_{c1} increases from 2×10^3 to 7×10^3 as the aspect ratio is decreased from 5 to 1 These results confirm the experimental works of Oertal (1976) and Catton (1970) which also show the same trend of behavior of the first critical Rayleigh number as the aspect ratio is decreased from infinity

Krishnamurti (1970) has given a diagram delineating the different transitions in a Rayleigh-Benard convection system as a function of Rayleigh number and Prandtl number. This is one of the earliest experimental studies where a number of different fluids were experimented with and a variety of cavity sizes were considered For air (Pr=0 71), the author concludes that at about Ra=5000 the flow changes from steady two-dimensional to steady three- dimensional flow along with the loss of rolls Around Ra=6000 the flow was observed to be time-dependent leading to turbulent state as the Rayleigh number was increased to Ra=10000

The experiments of Gollub and Benson (1980) for small aspect ratio enclosures showed that the initial flow configuration consisted of two symmetric rolls in the steady state This pattern was stable upto a certain value of the Rayleigh number With the further increase in the Rayleigh number, the well- documented phenomenon namely the decrease in the number of rolls occurs Mukutmoni and Yang (1992) numerically investigated the loss of rolls phenomenon in small box (4·2 1) for air The transition from 4 to 3 rolls was observed with an increase in the Rayleigh number The transition sequence showed the typical slanting of the rolls, as well as the thinning and thickening of the distorted rolls in the time sequence Later, Mukutmoni and Yang (1994) showed that there is generation of vertical vorticity specifically a swirl in the transition process For a small aspect

ratio, Davis (1967) and Stork and Muller (1972) showed that only the rolls parallel to the shorter side of the container are stable, but according to Mukutmoni and Yang (1992) rolls parallel to the longer side for small box can be stable below a certain critical Rayleigh number They concluded that the long rolls are metastable and are certainly less stable than the rolls parallel to the shorter side

Michael and Yang (1992) have reconstructed the three dimensional temperature field from its interferometric projections and have seen the presence of rolls in a water filled cavity of aspect ratios 8 7 and 9 0 The two horizontal confining walls of the cavity were made of aluminium The top plate was cooled using constant temperature water flowing over the aluminium sheet The bottom plate temperature was maintained using three electric foil heaters connected in series Two sides of the vertical side walls were made from delrin and the other two sides were made from 25 mm thick optical flats A Mach-Zehnder interferometer with 20 cm optics and a Helium-Neon laser of 10 mW power output were employed for collecting the projection data Wedge fringe setting of the interferometer was used to record the convection pattern inside the cavity

Muralidhar *et al* (1996) have studied the transient convection in a two dimensional square cavity The fluid considered was air Rayleigh numbers in the range of 10^4 to 10^5 were employed The cavity had a width of 74 cm and the aspect ratio considered was unity The horizontal surfaces were developed using brass sheets. The vertical side walls employed were made of a low thermal conductivity material such as perspex The isothermal conditions on the brass sheets were obtained by flowing water at constant temperature through them A Mach-Zehnder interferometer was employed to map the thermal field The experiments showed that the flow was mostly bicellular during the early transient period whereas it became unicellular at steady state The Nusselt number in the cavity was found to be maximum at the steady state

Forbes (1996) have reported a method for inverting the integrated phase-shift data obtained from an axisymmetric refractive index field The method is based on the Onion Peeling Algorithm and determines the refractive index as a function of radius over a series of irregularly spaced, concentric rings whose edges correspond to the fringe location This method is suitable for the analysis of

axisymmetric interferograms

Bhadra *et al* (1997) studied the Rayleigh-Benard convection problem in a cylindrical axisymmetric geometry The Rayleigh number employed was 6872 and diameter-to-height aspect ratio of the test cell was 36 1 A Mach-Zehnder interferometer was used to map the thermal field The experiments were performed at steady state and the projections of the flow field were recorded at four different angles namely 0°, 90°, 180° and 270° The authors established the axisymmetric nature of the flow field at steady state that was achieved after 4 to 5 hours from the start of the experiment The final aim of the work was to reconstruct the three dimensional temperature field from its two dimensional projection data using standard tomographic algorithms

Mishra *et al* (1998) studied the problem of Rayleigh-Benard convection in intermediate aspect ratio enclosures with air as the working fluid The Rayleigh number considered were 13900, 34800 and 40200 The authors concluded that at a Rayleigh number of 13900, the fringes were steady near the boundary walls but mild unsteadiness was present in the central horizontal layers At the higher Rayleigh numbers of 34800 and 40200, the unsteadiness was more pronounced, with flow switching between two well-defined states Apart from this study, the authors contributed notably in the field of tomography and developing a most versatile fringe thinning algorithm

The construction of apparatus used for the study of flow and heat transfer in Rayleigh-Benard convection in the last two decades has been presented in a review paper by de Bruyn *et al* (1996) Non-uniformities of the heat input to the two horizontal plates and the conductivity of the side walls are major concerns while making a convection test cell In most of the experiments reported the top plate temperature was held fixed and the bottom plate temperature was controlled by varying the heat input The experimentalists thus obtained the required temperature difference across the cavity In most experiments the cooling of a surface was produced by passing water at a low temperature over the flat horizontal plates The water temperature was kept constant using a heat removal device For heating, some experiments used an electrical resistance supplied with an electrical input while others passed hot water over the surface Uniformity

and flatness of the two bounding surfaces was another issue where care had to be taken Sagging of the horizontal surfaces was a frequently-faced problem

1.2.3 Crystal Growth

The subject of crystal growth forms a frontier area of research in science and technology, owing to their vivid physical and chemical properties The growth kinetics of a crystal growth process depends on the mass transfer and concentration difference near the growing crystal The following non-dimensional parameters are used to study the crystal growth process Grashof number for concentration differences,

$$\text{Gr}_c = \alpha_C (\text{C}_b - \text{C}_i) \text{g} \frac{\text{L}^3 \rho^2}{\mu^2} \tag{1 3}$$

Rayleigh number,

$$\text{Ra} = \frac{\text{g}\Delta\rho\text{L}^3}{\mu\text{D}} \tag{1 4}$$

and Sherwood number,

$$\text{Sh} = \frac{\text{KL}}{\text{D}} = \text{N}(1 - \text{F})\frac{\text{L}}{\text{d}\Delta\text{CD}} \tag{1 5}$$

where α_C is the concentration densification coefficient $(\partial\rho/\partial C)$, C_b is the bulk solute concentration, C_i is the interface solute concentration, g is the acceleration due to gravity, L is the characteristic dimension, $\Delta\rho$ is difference in solution density between bulk solution and interface, μ is the viscosity, D is the diffusion coefficient of solute in solution, K is the mass transfer coefficient, N is the flux into crystal surface, d is the fraction of supersaturation and F is the volume fraction of solute at crystal surface

Wilcox et al (1979) discussed in detail the free convection about a rectangular prismatic crystal growing from a solution He used schlieren techniques for visualization He studied the growth kinetics and the plume characteristics and stability The growth rate data were best correlated by $\text{Sh} = 0\ 48\ \text{Ra}^{0\ 25}$ with finite interface kinetics He discussed the threshold Grashoff number for plume instability and the frequency of eddy emission He also (1983) discussed the phenomena of secondary nucleation He observed that the growth rate was increased by convection up to the point where interface kinetics become rate controlling The

compositional inhomogenity and morphological instability were found to be worse for gentle convection than for either no convection or for vigorous stirring

Schlichta (1986) discussed the feasibility of using optical techniques for mapping the convection, temperature, and solute concentration in the solution around a growing protein crystal He concluded that ordinary schlieren and interferometric techniques are marginally sensitive and most displacement making techniques unsuitable therefore, phase-contrast schlieren, ultraviolet solute absorption, and laser anemometry was the most feasible Onuma et al (1988) used the Schlieren technique and Mach-Zehnder interferometry, to visualize the diffusion boundary layer and buoyancy buoyancy driven convection around a growing barium nitrate crystal from the aqueous solution, and their effect upon the growth kinetics of crystals in relation to the bulk supersaturation It was demonstrated that buoyancy driven convection plumes behaved differently depending on the bulk supersaturation, and that their behavior gave a definitive effect upon the growth rates They (1989) also demonstrated how severely the presence and behavior of buoyancy driven convection may affect the surface microtopographs and the growth kinetics of crystals They (1989) used Mach-Zehnder interferometer to directly measure the surface supersaturation, σ_s, on K-alum crystals growing in the aqueous solution, at different flow velocities u They found that the profile of the σ_s distribution over a growing face changes significantly and becomes asymetrical and shows a wider uniform σ_s region as increasing u Masayuki (1991) measured the gradient of refractive index around a crystal growing from a solution, using electronic measurement of fringes of Mach-Zehnder interferometer A very good linear relation was obtained between the gradient and growth rate of a KDP crystal Onuma et al (1992) applied a real time phase shift interferometer to the measurement of the concentration distribution around a growing or dissolving crystal Using the Abel transformation method, a quasi-three-dimensional concentration profile of a solution chlorate crystal was calculated, which made it possible to measure the actual surface concentration

Sunagawa et al (1995) discussed growth, dissolution and perfection of crystals from aqueous solution Both *ex-situ* and *in-situ* investigations were performed to analyze the problems of, solutal transport phenomena and the effect

upon the growth kinetics and perfection of the crystal, relation between bulk and surface supersaturations, effect of supersaturation distribution over a face, growth kinetics of a face, generation and behavior of lattice defects in relation to growth process and fluctuation in concentration, differences in growth mechanisms and lattice defects in different growth sectors, entrapment of mother liquid as inclusions, and differences and similarities between growth and dissolution Rudolph (1998) reviewed the elements of thermodynamics for the understanding and design of the crystal growth process The review concluded with some fundamentals of nonequilibrium states and introduces to the driving force of crystallization, nucleation process, kinetic phase diagrams and linear nonequilibrium (irreversible) thermodynamics

Piano et al (2000) applied electronic speckle interferometry (ESPI) to the observation of physical phenomena in transparent fluids, such as density and concentration gradients during crystal growth in aqueous solution or in gel KDP crystal growth from solution was studied and the data have been analysed to get information on solution dynamics and furthermore, to prove the validity of this technique for crystal growth Bredikhin et al (2000) used a technique based on the optical schlieren method to investigate in situ the growing crystal morphology under real rapid profiling growth conditions It was shown that the structure of growth centers on the growing surface essentially depends on the growth conditions, which provides additional possibility of the crystal quality control Booth et al (2002) developed a real-time phase-shifting interferometer for imaging interfacial morphology It employs a phase-shifting algorithm employing five interferograms and image processing that yield a three dimensional digital representation of the surface relief This method was applied in situ to the (110) face of KDP crystals growing from an aqueous solution They suggested that step-step interactions are likely the major factor for instability

1.3   Objectives of the Present Study

The present study is concerned with quantitative schlieren analysis of convective fields Both laser schlieren and colour schlieren have been implemented and com-

pared Benchmarking experiments have been carried out with Rayleigh-Benard convection as the test case of a 32 16 mm square cross-section and 447 mm length rectangular cavity Working fluid is both air and water Experiments were performed for six different Rayleigh numbers The fluid properties have been evaluated at the average cavity temperature in all the experiments The quantitative schlieren results have been compared with laser interferometry, shadowgraphy and numerical simulations

Subsequently, the transport phenomena during the crystal growth from aqueous solution has been studied Crystal growth experiments were done to analyse the convection pattern for varying ramp rate

Overall, the present work is directed towards achieving the following objectives (a) benchmarking of the algorithm for quantitative analysis of monochrome laser schlieren images, (b) comparison of the quantitative schlieren results with that of interferometry and numerical simulation, (c) analyse the effect of ramp rate on the strength of the concentration-driven convection currents during crystal growth, (d) optimum conditions under which large crystals of good quality can be grown from its aqueous solution, (e) development of colour filter, and colour schlieren applied to visualization of convective flow field

Chapter 2

Apparatus and Instrumentation

The experiments have been conducted with two seperate test facilities, Rayleigh-Benard convection in a rectangular cavity for benchmarking and facility for crystal growth from aqueous solution to study the transport phenomena during crystal growth process Both the test facilities with detailed experimental procedure and uncertainity have been discussed in this chapter

2.1   Test Cell for Rayleigh-Benard Convection

Benchmarking experiments were required to validate the algorithm for quantitative evaluation of schlieren images The classical problem of Rayleigh-Benard convection was selected as the test case for benchmarking the algorithm

A Rayleigh-Benard experimental setup is apparently simple in design It comprises of two horizontal surfaces of high thermal conductivity which are maintained at different constant temperatures The vertical side walls are perfect insulators Though simple in design, various factors are taken into account during the fabrication of the test cell and also while experimentation For example, uniformity and constancy of surface temperatures, parallelism of the walls defining the fluid layer and properties of the insulating surfaces are all factors that determine the quality of the experiments Further, some extraneous factors such as building vibrations, air motion and changes in the ambient temperature strongly
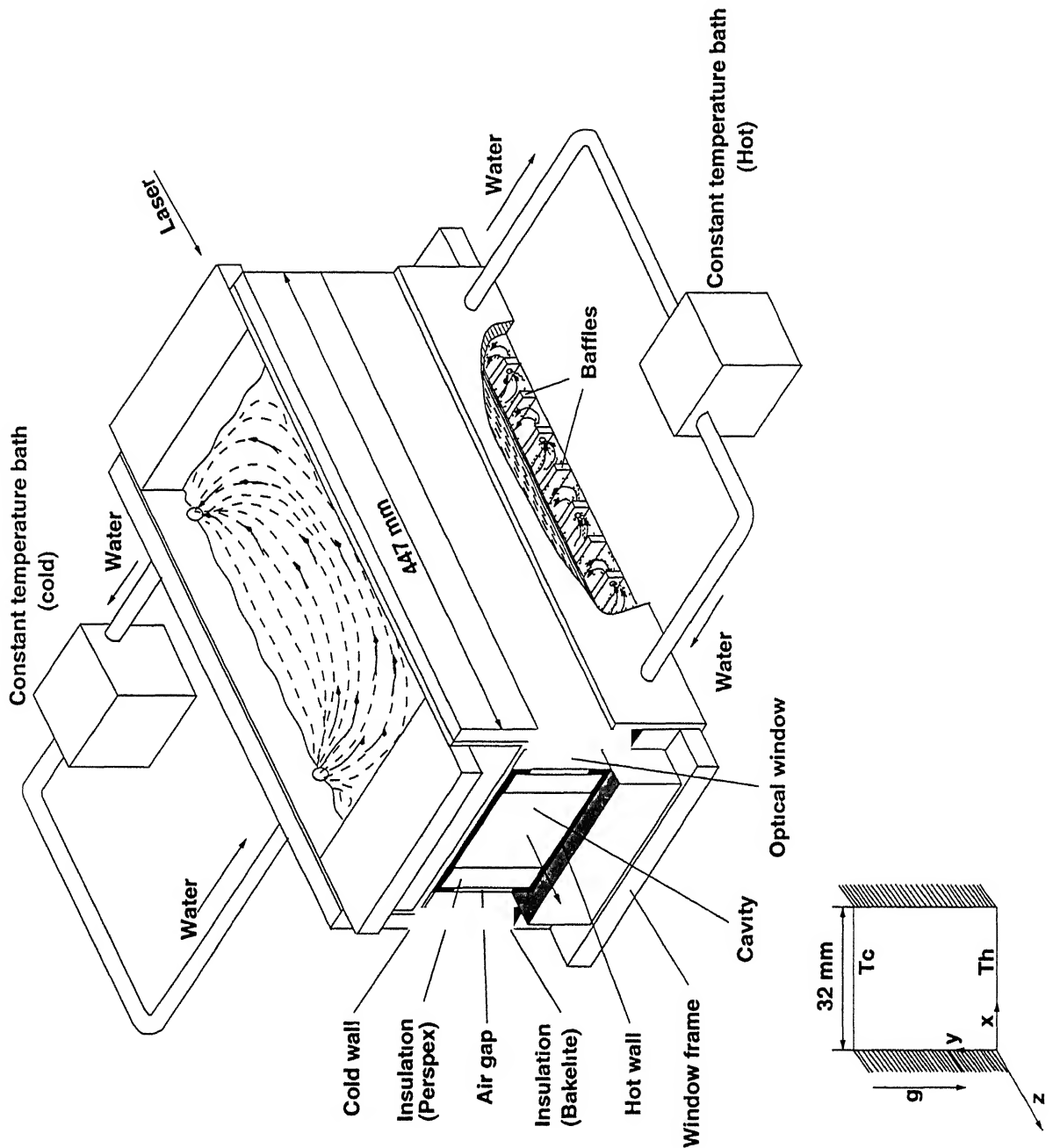
Figure 2 1   Schematic of the Apparatus for Rayleigh-Benard Convection

affect the recorded image Hence these experiments have to be performed with due care and precautions

The apparatus used to study the buoyancy-convection phenomenon in the horizontal layer of fluid is shown schematically in Figure 2 1 The cavity is 44 7 cm in length with a square cross-section of 3 216 cm The test cell consists of three sections namely the **Top Tank, Middle Test Section** and **Bottom Tank** The top and bottom walls of the cavity are made from 3 mm thick i plates The flatness of these plates was manufacturer-specified to be within ± 0 1 mm and was further improved during the fabrication of the apparatus The central portion of the experimental apparatus is the test section containing the fluid medium The side walls of the cavity were made of a 10 mm plexiglas sheet In turn the plexiglas sheet was tightly wrapped with a thick bakelite padding in order to insulate the test section with respect to the atmosphere The height of the test section was 32 16 mm and was measured to be uniform to within ± 0 1 mm A window was provided in the direction of propagation of the laser beam (parallel to the longest dimension of the cavity) and for recording the projected convective filed in the form of two-dimensional images The apparatus was enclosed in a larger chamber made of thermocole to eliminate the influence of external temperature variations

In the experiments, the active surfaces of the fluid layer were maintained at uniform temperatures by circulating a large volume of water over them from constant temperature baths with an accuracy of ± 0 01°C For the upper plate, a tank like construction enabled extended contact between the flowing water and the aluminium surface Special arrangements were required to maintain good contact between water and the lower surface of the plate Baffles were used to introduce a tortuous path to flow, thus increasing the effective interfacial contact area The variation in the surface temperature was monitored by thermocouples connected to a multi-channel temperature recorder to be within ± 0 1°C

The convective field in the test cavity was set up by differentially heating its horizontal surfaces with upper wall being at relatively lower temperature compared to the lower wall, hence giving rise to an unstable stratified fluid flow configuration In the present work, the experiments were started with the fluid layer and the bounding walls, all at the ambient (room) temperature The incre-

ment in Rayleigh number was applied in a single step as follows The upper wall
of the fluid layer was cooled by circulating water from the constant temperature
bath The time elapsed for the upper boundary to attain a constant temperature
was around 15 minutes The convection pattern in the fluid layer stabilized after
around 2 5-3 0 hours of experimental run time

A series of temperature differences have been applied to study the transient
evolution of the thermal field and the long time convection patterns   For air,
the applied temperature differences between the top and the bottom walls of the
cavity are ΔT=5, 10, 20, 30, 40 and 50 K which correspond to Rayleigh numbers
of 1 40 $\times$ 10^4, 2 70 $\times$ 10^4, 5 10 $\times$ 10^4, 8 50 $\times$ 10^4, 1 13 $\times$ 10^5 and 1 40 $\times$ 10^5 In the
experiments with water as the working fluid, relatively lower range of temperature
differences have been selected The applied temperature differences are ΔT= 3, 5,
6, 8, 10 and 13 K The corresponding Rayleigh numbers are 2 50 $\times$ 10^6, 4 40 $\times$ 10^6,
5 40 $\times$ 10^6, 7 50 $\times$ 10^6, 9 80 $\times$ 10^6 and 13 50 $\times$ 10^6 respectively These values of
Rayleigh numbers, both for air and water, are large in comparison to the critical
Rayleigh number for the infinite fluid layer

Convection patterns in the fluid layer have been captured in the present
work by using the three refractive index based optical techniques namely, inter-
ferometry, schlieren and shadowgraph Imaging technique has been chosen on
the basis of the strength of thermal gradients present in the flow field Hence, in
the experiments with air for $\Delta T \leq 20$ K, interferometry and schlieren have been
applied to visualize the flow field and record the convection currents For 30
K$\leq \Delta T \leq$50 K, the imaging techniques are interferometry, schlieren and shadow-
graph In the experiments with water because of the presence of high gradients,
shadowgraph has been used as the imaging tool

2.1.1   Optical Set-up

This subsection describes the optical arrangements for the three imaging tech-
niques used in the present work

A Z-type monochrome schlieren system has been used as the primary in-

strument to record the temperature gradient field in the form of two-dimensional
images   The details on the optical arrangement of schlieren system has been
discussed in detail in the following chapter   Figure 2 2(a) shows the initial in-
tensity distribution on the screen in the absence of any test region   When the
test medium is introduced, part of the image source is displaced and the illumi-
nation of the corresponding part of the image decreases or increases according to
whether the deflection is towards or away from the opaque side of the knife-edge
Figure 2 2(b)shows a candle flame image for near wake and far wake conditions
with a horizontal knife-edge   The knife-edge is set perpendicular to the direction
in which the density gradients are observed   Since in the present study of rectan-
gular cavity, the gradients are predominantly in the upward vertical direction, the
knife-edge is kept horizontal   To take care of the fluctuations in temperatures and
other external factors like floor vibrations etc, the surrounding atmosphere was
kept at an uniform constant temperature during the experimental run time and
the movement of people was strictly prohibited to avoid the vibration problems
at the time of recording of the schlieren images

(a)   (b)

Figure 2 2   (a)Initial schlieren setting, (b)Candle flame near the wake

A Mach-Zehnder interferometer has been used for the interferometric study
of the convective field. The schematic diagram of the set-up is shown in figure
2 3   The coherent light source is a 35 mW, continuous wave (632 8 nm) He-Ne
laser   The mirrors and beam splitters employed in this configuration are of 150
mm diameter. The beam splitter has 50% reflectivity and 50% transmitivity   The
mirrors are coated with 99.9% pure silver and employ a silicon dioxide layer as a
protective layer against oxidation   All the experiments have been carried out in
the infinite fringe setting mode of the interferometer   As the working fluid was

air, ambient conditions were maintained at the reference section and no reference chamber was used
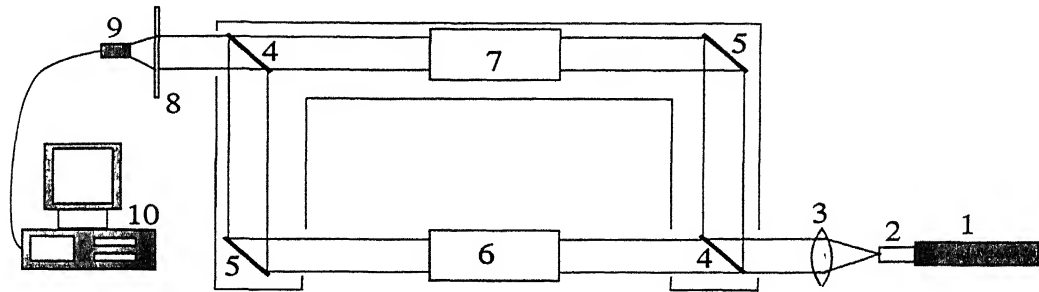
Figure 2 3   Schematic diagram of the Mach-Zehnder interferometry

1 Laser, 2 Spatial filter, 3 Collimating lens, 4 Beam splitter, 5 Plane mirror,
6 Test section, 7 Reference section, 8 Viewing screen, 9 CCD camera,
10 Personal computer

Alignment of the Interferometer

Before the start of the experiment the interferometer has to be aligned All the experiments in the present work are performed with the infinite fringe setting mode of the interferometer. Adjustment of the infinite fringe setting is delicate and requires efforts. The initial field of view is one of complete brightness since the interference is constructive The geometrical and the optical path lengths of the test and reference beams are same in the absence of any thermal disturbances in the path of the test beam As the interferometer approaches the infinite fringe setting the distance between the fringes increases and the number of fringes decreases Figure 2 4(a) infinite fringe setting mode of the interferometer when no temperature gradient has been applied in the flow field In an infinite fringe setting mode, the fringes directly represents the isotherms Figure 2 4(b) shows an candle flame image in the infinite fringe setting mode

Similar set of optics as in the schlieren arrangement has been used to configure the shadowgraph set up The schematic diagram of the shadowgraph technique This is a relatively simpler configuration as compared to interferometry

(a)   (b)
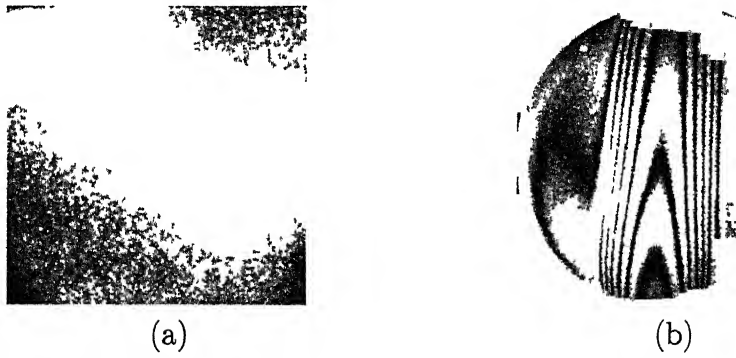
Figure 2 4   (a)Infinite fringe setting, (b)Candle flame at infinite fringe setting

and schlieren as far as alignment is concerned   The position of the screen on which the shadowgraph images are displayed has been optimally chosen so as to get high quality images with the dominant features of the flow field clearly visible and were recorded at the highest possible resolution of the CCD camera   Figure 2 5(a) shows the initial distribution of intensity in the absence of any optical disturbance in a shadowgraph system   After the insertion of the test medium, the illumination on the screen increases in accord with the strength of the gradients present in the flow field   Figure 2 5(b) shows an candle flame image as visualized by the shadowgraph technique

(a)   (b)
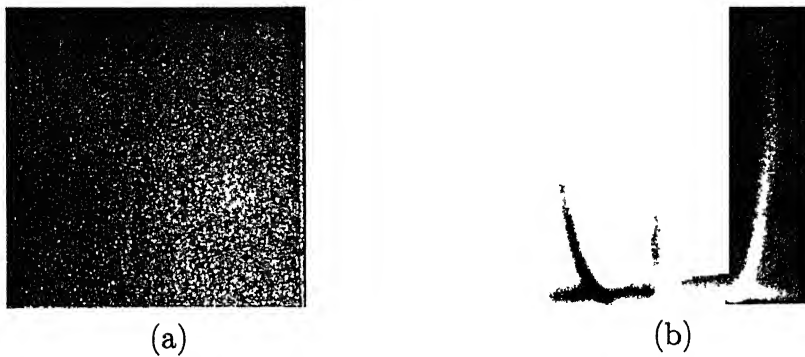
Figure 2 5· (a)Initial shadowgraph image, (b)Candle flame image

2.1.2   Experimental Procedure

Schlieren

Before the start of the experiments, the initial setting of the test cell is recorded
The initial setting is taken so as to get the maximum sensitivity without loss of
any important information   External disturbances like the movement of peoples
was prohibited and the air-conditioner was turned off, so that, they do not affect
the initial setting of the experiment   All the experiments have been performed
to record the long-time convection patterns, so that the steady state is reached
Analysis is done for the steady state schlieren images

Interferometer

Before the start of the experiments, the Mach-Zehnder interferometer is set in the
infinite fringe setting mode   The interferometer lies on the pressurized pneumatic
isolation mounts and this ensures that the floor vibrations and other external
disturbances do not disturb the initial setting of the interferometer   A cross-check
is again made after sometime in order to ensure that the infinite fringe setting in
fact prevails in the experiment and after that only the experiment is started   All
the experiments have been performed to record the long-time convection patterns
prevailing in the test cavity so that the steady state is reached before recording
the interferograms   The experiments are run for a period of 2 to 3 hours at an
stretch to achieve this condition

Shadowgraph

The experimental procedure was similar to that of the schlieren   It was used
to capture high gradients prevailing in the test cavity when schlieren was not
suitable   Shadowgraph was used for high Rayleigh number convective flow con-
ditions

For all the above experiments isothermal conditions on the lower and the
upper plates of the test cell are ensured by circulating a large volume of water

in the lower and the upper tank   Total experimental run time of around 3 hours
enables the plates to acquire a constant and uniform temperature through out
their surfaces and hence leading to isothermal conditions   The whole test cell
is placed inside a thermocole sheet chamber to avoid the effects of external air
currents

The images have been recorded at regular intervals of time in order to show
the transients that the fluid undergoes before reaching the steady state   For
steady state, three to four images have been recorded in a gap of 5 to 10 minutes
to ensure that the steady state condition in-fact prevails in the cavity   The lights
of the room are switched-off at the time of recording of the images

2.1.3   Uncertainty and Measurement Errors

Errors in the experimental data are associated with misalignment of the appa-
ratus with respect to the light beam, noise generated at different stages of the
experiments including the imperfections of the optical components and the in-
trinsic uncertainty in the convection process itself   Furthermore, the nonuniform
scattering at the test cell also contribute to the measurement errors. All experi-
ments were conducted several times to establish the repeatabilty of the convective
patterns   In the experiments with air for which the quantitative results have been
presented, the time-dependent variation of the convective field (the movement of
fringes in the case of interferometry and the change in the intensity field in case
of schlieren) was not found to be the source of uncertainty at the lower values of
Rayleigh numbers   It was partly so at Ra=5 10 $\times$ 10^4 At these Rayleigh num-
bers, the plate-averaged Nusselt number was found to be in good agreement with
published correlation   The steady state temperature profiles plotted as a function
of the vertical coordinate of the cavity also revealed an acceptable match between
the experimental data and the numerically generated solution of the flow field
Hence the results obtained in the present work can be taken to be qualitatively
meaningful

2.1.4   Benchmarking

Steady state was obtained with the experiments with lower Rayleigh number
after 3-4 hours of experimental run time To get meaningful quantitative results
in the form of temperature distribution and average heat transfer rates in terms
of Nusselt number, quantitative analysis of the experimentally recorded images
have been performed at steady state

The degree of complexity involved in data reduction is much lower in in-
terferometry as compared to that in schlieren technique In interferometry, one
directly gets the changes in the refractive index field with respect to the refer-
ence environment once an optical disturbance is applied in the path of the beam
Moreover, the experiments have been performed in an infinite fringe setting mode
of the interferometer, the fringes can be considered as isotherms In an experi-
mentally recorded interferogram, these fringes are bands of certain thickness with
all the useful information concentrated at the center and have been reduced into
thin lines (which represent the points of minimum locations) by applying fringe
thinning algorithm developed by Mishra *et al* [33] Using boundary conditions
in the form of known temperatures at top and bottom walls of the cavity and
temperature change per fringe shift, the absolute fringe temperatures have been
estimated A detailed description of steps involved in data reduction from an
experimentally recorded interferogram was given by Mishra [37] in the context of
Rayleigh-Benard convection case in an intermediate aspect ratio enclosure

Image information in a schlieren system is basically due to the deflection of
light beam towards the region of high refractive index gradient once an optical
disturbance is in the path of the beam The contrast of the schlieren image can be
related with the refractive index gradient by the equation 3.22 given in the next
chapter Integrating of the equation once gives the two-dimensional refractive
index field

The terms of the equation 3 22 have been discretized using a finite differ-
ence scheme Since the images are in the form of two-dimensional matrix of
numbers, maximum number of pixels/grids are known beforehand. Boundary
conditions have been properly defined in terms of the known temperature values

at the top/bottom walls   In contrast to interferometry where the information
is located at the fringes only, quantitative analysis of a schlieren image gives
temperature values at each and every pixel of the image which avoids the inter-
polation/extrapolation errors that are inevitable in the case of interferometry

The dimensional wall heat transfer rate represented by the Nusselt number
has been defined in the present work as

$$Nu = \frac{-h}{T_{hot} - T_{cold}} \left. \frac{\partial T}{\partial y} \right|_{y=0,h} \qquad (2\ 1)$$

Using this definition, the local and average Nusselt numbers at the top and the
bottom walls of the cavity have been calculated   The average Nusselt number for
each of the walls has been captured with the following experimental correlation
for air by Gebhart et al [2]

$$Nu = 1 + 1\ 44 \left[1 - \frac{1708}{Ra} \right] + \left[\left(\frac{Ra}{5830} \right)^{1/3} - 1 \right] \qquad (2\ 2)$$

Equation 2 2 is applicable over a wide range of Rayleigh numbers and is practically
independent of the cavity aspect ratio

A series of cross-checks have been enforced to validate the quantitative
results obtained from the experimental images   In interferometry analysis, the
portion of the image where the fringes are relatively dense have been chosen to
start the fringe temperature calculation steps   Starting from the known lower
wall temperature values, the upper cold wall temperature has been predicted
and the same procedure is repeated with the direction of marching reversed
(At lower temperature differences particularly at $\Delta T=5$ K, the distribution of
fringes was not uniform at the two walls and the number of clear fringes in the
interferograms were also too low   For this reason, only one direction of marching
was followed starting from the wall where fringe density was relatively higher
But here, to cross- check the predicted results, similar procedure was applied at
more than one number of columns along the width of the cavity and the resultant
values have been found to be in acceptable limits with a maximum error of $\approx 5\%$
between any two arbitrarily selected columns in the portion where fringes are
dense.) Similar set of cross-checks have been applied in the quantitative analysis
of schlieren images   An acceptable match between the predicted and the actual

wall temperatures validates the steps involved in data reduction procedure and also makes the experimental results qualitatively meaningful

2.2   Apparatus for Crystal Growth Process

Growth of crystal from its aqueous solution hinges on achieving supersaturation by systematic cooling of the solution Growth of a good quality crystal involves control of various growth parameters which includes the ramp rate, rotation of the seed, pulling of the seed and degree of supersaturation Minor fluctuations in the temperature can lead to the onset of unwanted nucleation Nucleation is the deposition of salt at unwanted positions In the present experiment the crystal growth apparatus has been developed to ensure satisfactory control over the growth parameters The apparatus for the crystal growth process comprises of a growth chamber, a surrounding water-bath to maintain the temperature of the solution and associated instrumentation for control of the ramp rate of the solution It also have provisions for pulling of the seed and its rotation

Figure 2.6 shows the schematic diagram of the crystal growth apparatus The crystal growth apparatus have the following main components 1 Crystal growth chamber, 2 Temperature controller unit, 3 Pulling and rotation assembly, 4 Optical set-up

2.2.1   Crystal Growth Chamber

The crystal growth chamber is shown in figure 2 7 The inner chamber is the growth chamber which holds the solution It is preferable for the crystal to grow uniformly in all the directions i e there is no preffered direction of crystal growth It prohibits asymmetry in the crystal shape So, to ensure that the flow patterns are symmetric about the crystal axis, a cylindrical shape of the growth chamber has been chosen The chamber has a diameter of 14 cm and a height of 21 cm made of glass Glass provides the advantage of a high grade smooth surface, as presence of any roughness in the inner surface may act as a favorable site for nucleation Glass is chemically non reactive to most of the solutions and also

1 Laser
2 Flat mirror
3 Concave mirror
4. Growing crystal
5 Stepper motor
6. Knife edge
7 Screen
8 CCD camera
9. Personal computer
10. Heating coil
11 Thermocouple
12. Temperature controller unit
13. Thyristor unit
14 Temperature controller programmer

O – origin at the center
of the crystal
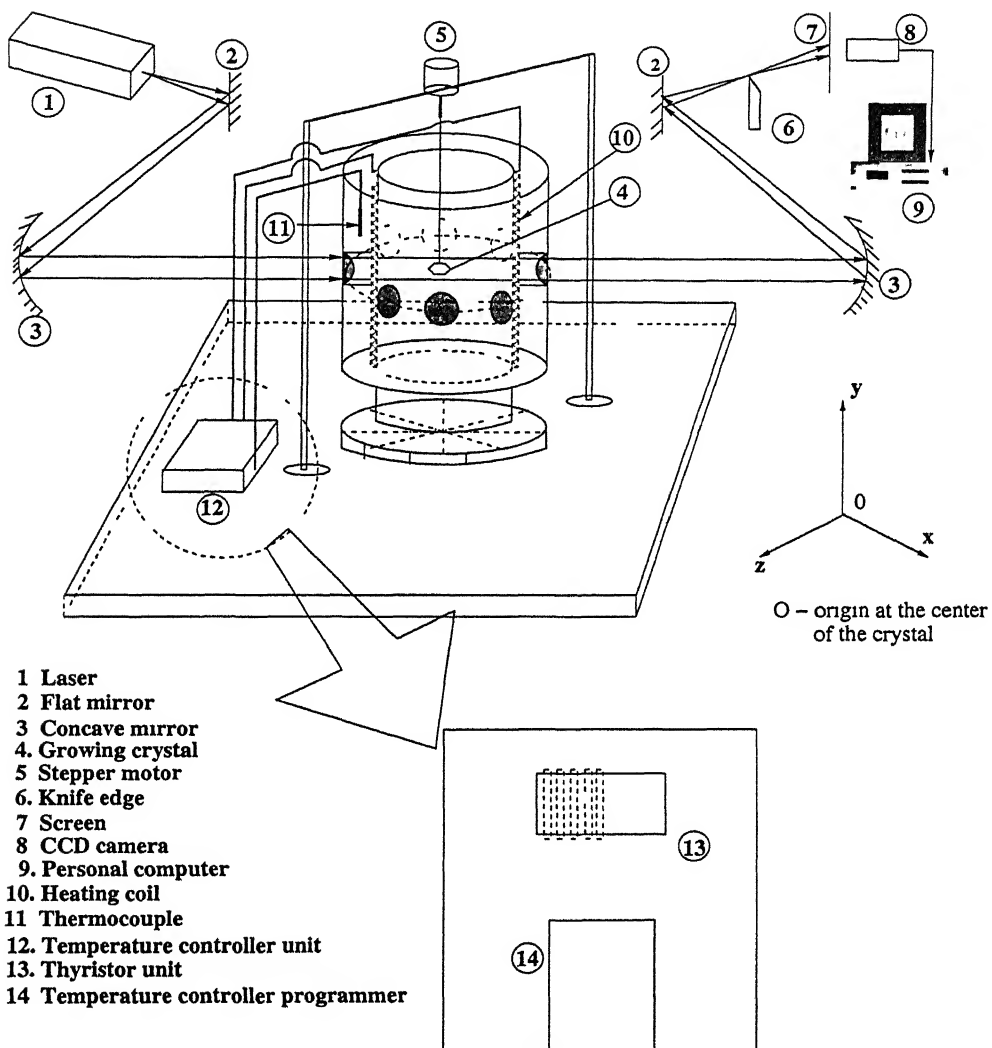
Figure 2 6. Schematic of the crystal growth apparatus with schlieren
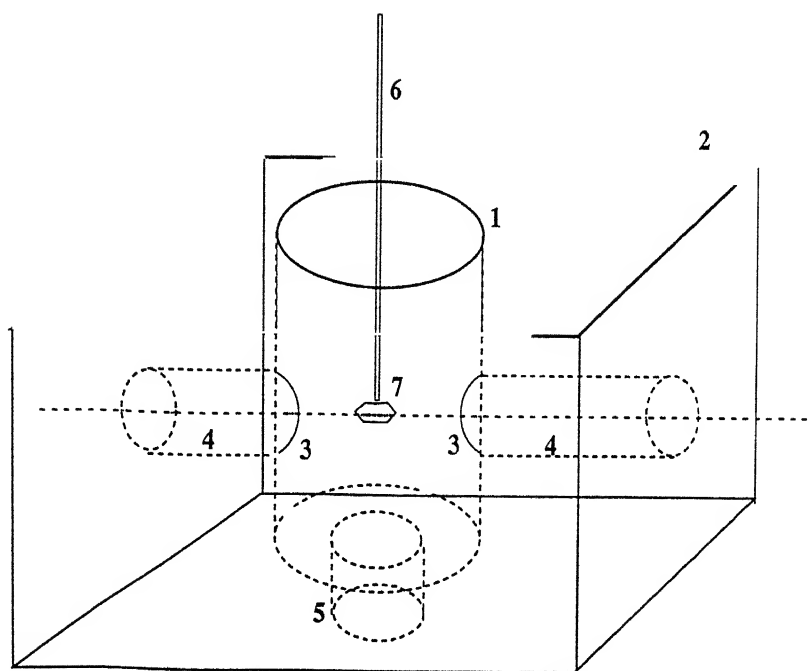
Figure 2 7   Schematic of the crystal growth bath

1 Inner chamber, 2 Outer chamber, 3 Optical window, 4 Connecting tube,
5 Brass base, 6 Seed holder, 7 Growing crystal

for the case of potassium di-hydrogen phosphate (KDP) solution   Glass is also optically transparent, thereby assisting in visual inspection of the crystallization process

The outer chamber consists of water which is cooled at an uniform rate   It maintains the temperature of the solution in the growth chamber   The volume of water is sufficient enough to maintain the temperature of the solution   It was made of square cross section for ease in manufacture   The dimension of the chamber is $37 \times 37 \times 26$ cm.   It is made up of sheets of plexiglas   Plexiglas is thermally insulating, and thus helps in maintaining the temperature of the circulating water   It can also resist high operating temperature   Due to its optical transparency the crystal growth process can also be visually inspected   Proper fabrication ensures its resistance to leakage at high temperature of water

The growth chamber rests on a brass base It ensures circulation of water at the bottom face of the chamber Additional holes are made on the circumference of the base to enhance water circulation

Ordinary glass will disturb the light beam passing through it It will add to errors during quantitative analysis of a schlieren image So high quality optical windows are used in the path of the beam The path is also isolated from the water in the outer chamber by a connecting rod Sufficient care is undertaken in fixing the optical windows to the inner chamber to avoid rough protrusions This assists in the control of unwanted nucleation

The crystal growth chamber is covered by a plexiglas lid to isolate the solution from the ambient atmosphere It is in addition covered by a thermocole casing to enhance the insulation from the atmosphere The casing is removed in the time of recording images

2.2.2   Temperature Controller Unit

Ramp rate is the main parameter which controls the growth rate and the strength of the convection current, which in turn affects the crystal quality In the present case the temperature was controlled by the EUROTHERM temperature controller unit It have two major components, (a)Controller/Programmer and (b)Power Thyristor Unit.

Controller/Programmer

The controller/programmer controls the ramp rate of the crystal growth process Very low ramp rate ($\approx$ 0 1°C/hr) can be programmed by the controller The temperature of the water in the outer chamber is sensed by a thermocouple The power to the heater (or cooler) is controlled depending on the difference of the desired or set temperature to the water temperature The controller can be programmed for ramp rate (both heating and cooling), temperature stepping, maintaining of a constant temperature Several modules can be coupled together to get a complete set of controlled temperature control For our experiments a

very low ramp rate was programmed for systematic cooling of the solution

Power Thyristor Unit

The controller/programmer trips the heater (or cooler) power connections with the help of the power thyristor unit A large amount of heat is usually generated in it It is cooled by natural convection, and have fins in it for heat transfer enhancement

2.2.3   Pulling and Rotation assembly

Provisions are provided for pulling the seed and its rotation When the seed grows to a bigger size, the associated convection currents becomes vigorous This may affect the quality of the optical crystal Pulling of a portion of the seed out of the solution reduces the strength of the convection currents Pulling of the seed is achieved by a lead screw arrangement supporting the seed holder

At the initial state of the growth process, the associated convection currents are essentially two dimensional But for a bigger grown crystal, the convection currents tends to become three dimensional in nature This makes the crystal non-homogeneous To enforce two dimensionality, rotation is given to the seed A stepper motor of 2 kg-cm torque is used for this purpose The seed holder is connected to the stepper motor shaft Accurate rotational speed of very low rpm can be achieved with the stepper motor control circuit assembly

2.2.4   Optical Set-up

A Z-type schlieren optical set-up is used as the visualization technique. The schlieren optical measurement technique has been discussed in great detail in next chapter Due to a very low ramp rate, at a particular instant of time there are essentially no thermal gradients present in the solution So all the convection currents visible by the schlieren technique is due to the concentration gradients

in the solution Hence, in this case, the refractive index gradient can be directly related to the concentration gradient

2.2.5   Experimental Procedure

Crystal growth hinges on achieving supersaturation by systematic cooling of the solution Cooling is done by the temperature controller unit The steps involved in the crystal growth process are as follows

A pure solution of KDP is required to maintain the quality of the optical crystal Thus the solution is prepared in distilled water The solution is prepared at a temperature higher than the room temperature The amount of KDP salt is determined by the degree of supersaturation desired and from its solubility curve After the solutes are completely dissolved, small micro particles remains suspended in the solution Solutes may get dissolved into it and lead to nucleation during the crystal growth process So the temperature of the solution is further increased and maintained at that temperature for a longer period of time This ensures complete dissolution of the solute particles The solution is then filtered using a high quality filter paper to ensure removal of any suspended impurities or solutes

Water at the outer chamber is maintained at the same final temperature of the solution After the solution is filtered, it is poured into the growth chamber The temperature is maintained at that temperature for about 5 hours so that any suspended solute particles get dissolved completely A ramp rate is then programmed The temperature is reduced at a faster rate till the supersaturation temperature

The seed is then inserted into the solution The seed initially gets dissolved, as its affinity of dissolving is more than the affinity of the solute to get dissolved into the seed This dissolution of the seed is partly beneficial as it removes impurities from the surface of the seed After the insertion of the seed the ramp rate is reduced to a lower rate ($\approx 0 1^{\circ}$C/hr) After some time, the affinity of the solute towards the seed dominates the affinity for dissolution, and the crystal

starts growing

Figure 2 8 shows the process of buoyancy induced convection currents due to the concentration difference The black dots are the water molecule and the

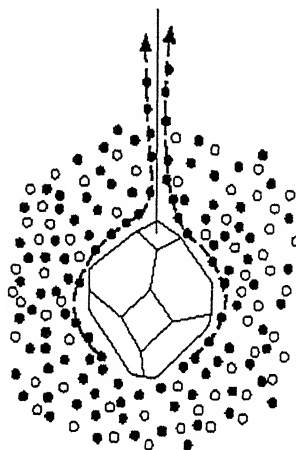Figure 2 8 Concentration convection currents

white dots are the solute molecule Far away from the seed the water and the solute molecules are uniformly mixed But near the seed the solute molecules gets deposited into the seed and the solution is left with only the water molecules Water being lighter will move up Fresh solution will come and occupy the vacant space This process continues to generate the concentration convection currents This convection currents are the main carrier of solutes to the seed Thus, more and more amount of solutes gets dissolved into the seed and the seed starts growing

2.2.6   Uncertainity and Measurement Errors

Errors in the experimental data are associated with misalignment of the apparatus with respect to the light beam, and noise included during the experiments due to the quality of the optical components and the convection process itself Proper care was taken in manufacturing of the set-up to maintain the parallelism of the optical windows The convection may not be purely due to the concentration gradients Water is circulated for a longer period of time and the set-up is properly insulated, so that the temperature gradients gradually die out, before the seed is

inserted to the solution This ensures that the convection is purely due to the concentration gradients present in the vicinity of the seed Errors may also occur due to the diffraction process from the sharp corners of the seed A disturbance was given to the seed and the bright patches was seen moving upwards with the convection plumes This ensured that the higher intensity regions were due to concentration gradients and not by diffraction

Chapter 3

Quantitative Schlieren Technique

This chapter discusses the principles of schlieren and procedures for the quantitative evaluation of the schlieren images. Schlieren is an refractive index based measurement technique which depends on deflection of a ray of light from its undisturbed path when it passes through a medium in which there is a component of the gradient of refractive index normal to the ray. Here the index of refraction or spatial derivative of the index of refraction of the medium is measured and from it some properties i.e. density, temperature and concentration of the flow are determined. Schlieren indicates the first derivative of the index of refraction normal to the light beam. The resulting illumination of the light pattern is determined by the index of refraction. For a homogeneous medium, the index of refraction is a function of the thermodynamic state and therefore can be used to determine density, pressure and or temperature in the flow

3.1   Schlieren Set-up

A variety of schlieren arrangements is possible, all embodying Toepler's design principles. It can be either of the lens-type or mirror-type. While lens-type schlieren instruments can be in-line, and therefore relatively simple, mirror-type instruments are inherently folded thus tending to be rather more difficult to align. The advantages achieved are compactness and higher sensitivity to disturbances

3.1.1   Monochrome Schlieren

Figure 3 1 shows a Z-type 2-mirror monochrome schlieren system   The optics involves concave mirrors of $\approx 1\,30$ m focal length and 0 20 m diameter   A 35 mW, continuous wave (632 8nm) He-Ne laser is employed as an coherent light source   It emits an light beam of 2 5 mm diameter   So the beam is expanded by an spatial filter to get an larger field-of-view   The expanded beam is directed by an flat mirror to the first concave mirror such that the test region is illuminated by a collimated beam of light   A second concave mirror refocuses the beam to an image of the light source and a real inverted image of the test area is formed in the viewing screen   At this point the optical system is merely a projector, imaging opaque objects in the test area as silhouettes on the screen   Transparent schlieren objects are not imaged at all until a knife-edge is added at the focus of the second mirror   Due to the presence of the knife-edge, the displacement of the image of the source is cut off so that the illumination on the screen is reduced uniformly
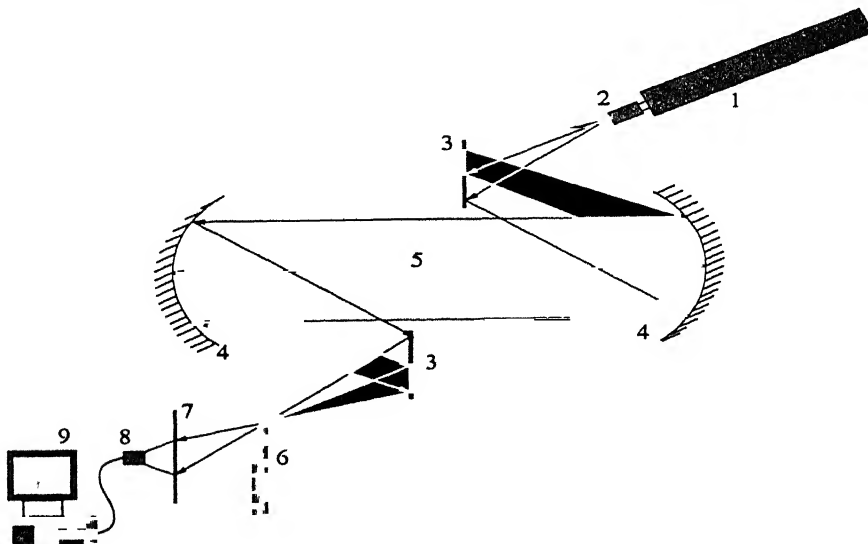

Figure 3 1   Schematic diagram of a Z-type schlieren system

1.Laser, 2 Spacial filter, 3 Flat mirror, 4 Concave mirror, 5 Test section,
6 Knife-edge, 7 Viewing screen, 8 CCD camera, 9 Personal computer.

Figure 3 2 shows the diagram of the knife-edge plane The knife-edge blocks a portion of the rectangular composite light Now, when a optical disturbance is placed at the test section, part of the image source is displaced and the illumination of the corresponding part of the image will increase or decrease according to whether the deflection is towards or away from the opaque side of the knife-edge Now considering the case of a schlieren object in the test area that refracts a certain light ray through an angle ε Thus the unobscured height $a_0 + \Delta a$, passes extra light to a corresponding point in the schlieren image If the y-component of the ray deflection angle is ε_y, then the source image is shifted upward in the knife-edge plane by a distance

$$\Delta a = f_2 \varepsilon_y \tag{3 1}$$

where f_2 is the focal length of the second lens This generates a partial picture of the schlieren object on the screen giving an schlieren effect
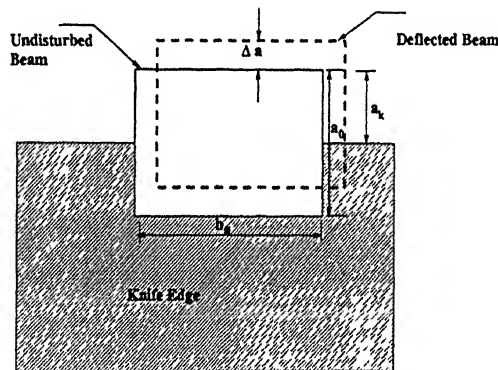
Figure 3 2 View of deflected and undisturbed beams at the knife-edge

Contrast in the schlieren image refers to the ratio of differential illuminance ΔI at an image point to the general background level I,

$$\mathrm{Co} = \frac{\Delta I}{I} = \frac{f_2 \varepsilon_y}{a_K} \tag{3 2}$$

where a_K is the height of the image not cut off by the knife-edge The image contrast is the output of the schlieren instrument Since the sensitivity of any instrument is basically an influence coefficient, i e d(output)/d(input), we can therefore write the schlieren sensitivity or *contrast sensitivity* - as the rate of

change of image contrast with respect to the refraction angle

$$S = \frac{dCo}{d\varepsilon} = \frac{f_2}{a_K} \qquad (3\ 3)$$

It provides a measure of schlieren sensitivity independent of any observing or recording means It also shows that sensitivity is proportional to the focal length of the second concave mirror Further, it reveals that the *unobstructed* height of the source image, a, determine sensitivity and not the overall height

The diffraction affects the accuracy of the quantitative schlieren methods The magnitude and extent of its effects increase as the proportion of the source cut off by the knife-edge is increased It is found that although the illumination on the viewing screen is approximately constant in the absence of the knife-edge, this is no longer the case when knife-edge is present The effects of diffraction then usually results in increased illumination on the viewing screen as the boundaries of the aperture are approached i e near the images of the test section walls and the model under test The illumination does not fall sharply to zero at the boundaries, but dies away gradually

The schlieren image is captured by an CCD (Charge Coupled Device) camera of spatial resolution ranging from 512x512 to 768x574 The CCD camera is coupled to a PC-based image processing system through an 8-bit A/D adaptor card It stores the images in the form of matrix of 256 (i e , 2^8) integers, with intensities varying in the range of 0-255, 0 being the lowest intensity and 255 the highest intensity. The present camera have a image acquisition rate of 30 images per second which assists in study of unsteady behavior of the fluid When the camera reaches its highest limit of 255, it does not sense the difference of the corresponding intensity value with a higher intensity value This is called the camera saturation So, a higher amount of light is needed to be blocked initially with the knife-edge, which may in turn lead to the loss of important informations and induce error due to diffraction effects. Hence, a balance is needed to be achieved between the camera saturation and knife-edge position without loss of important informations.

General Alignment Procedure

The first adjustment of the schlieren apparatus is to locate the light source at the focus of the first mirror An Image of the source will be formed by the reflection of the light from the first optical windows The position of the source is adjusted until this image is in focus in the plane of the source If the light reflected back from the window does not give image, which is brought enough to be clearly visible, a small plane mirror may be held in contact with the window so that the reflecting surface is parallel to it The next adjustment is to set the parallel light beam formed by the first mirror so that it passes through the test cell in a direction perpendicular to the glass side windows In the case of two-dimensional models, the span may not be exactly perpendicular to the glass side walls, so that the light beam may not be truly parallel to the span If this is so, a screen held immediately behind the working section will reveal a bright band running parallel to the model, resulting from the reflection of the light from the surface The position of the light source and the inclination of the first mirror are adjusted until this band disappears, leaving the approximately uniform bright band around the model which arises from the effects of diffraction The second mirror placed after the test section is next moved vertically or laterally such that an image of the model under test gets formed on the viewing screen The knife-edge is then inserted in the focal plane of the second mirror and its position is adjusted until the screen darkens as uniformly as possible when the edge is traversed across the image of the light source. The edge is then set so that the required fraction of the image of the source is cut off The amount of cut-off can be estimated by holding a white card behind the knife-edge so that the parts of the source, which are cut off and unobscured, can be observed

It is found that the appearance of the images of shock waves and boundary layers are more sensitive to the focusing of the apparatus than the sharpness of the geometrical image of the model Thus it is desirable to refocus the apparatus with running experiments so that the phenomena which is of greatest interest are shown as clearly as possible with minimum distortion

3.1.2   Colour Schlieren

Colour schlieren differs from the monochrome schlieren mainly by the replacement of the knife-edge by a colour filter   The spatial variation of filter colour causes light deflected by nonuniformities to produce coloration of the image of the nonuniformities   Figure 3 3 shows the optical set-up of an colour schlieren apparatus   The laser is substituted with a white light source   White light source consists of a halogen lamp of 150 W power   Light energy is carried by an 5 5mm diameter fiber optic cable till the aperture   A pointed light source can be achieved by pinholes having diameters ranging from 5 to 50 microns   A smaller size of the pinholes is preferred to get better sensitivity of the colour schlieren setup   The output of the pinhole or the aperture will be an expanded beam of light   A set of collimating lens are used to lighten the test section with an collimated beam of light   The beam after the test section is refocused with another decollimating lens   The rainbow filter is placed at the focus of the second lens   The image of the optical disturbance is formed at the viewing screen   The image is captured by an coloured CCD camera of resolution 1008×1008   The CCD camera is coupled to the computer by an 8/10 bit card
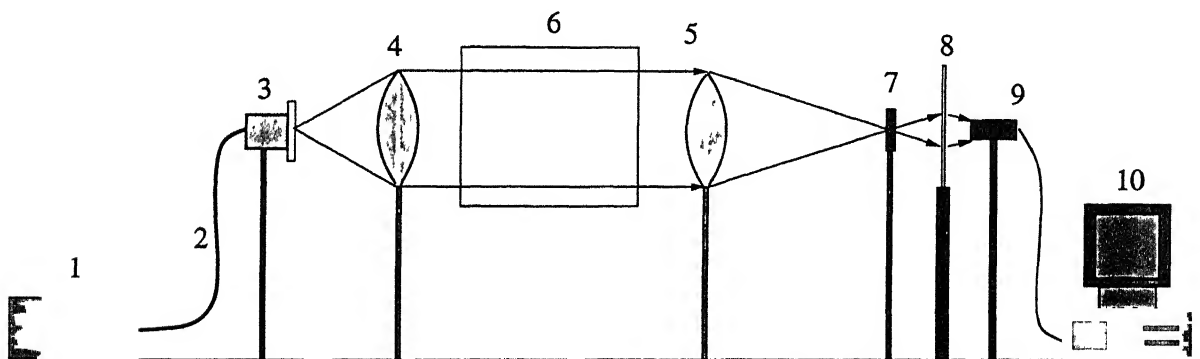

Figure 3 3   Schematic diagram of colour schlieren apparatus

1 White Light Source, 2 Fiber optic cable, 3   Source aperture, 4 Collimating lens, 5.Decollimating lens, 6   Test section, 7 Colour filter, 8 Viewing screen, 9 Colour CCD camera, 10 Personal Computer

There are several advantages to be gained from adding colour to the conventional monochrome schlieren image Colour coding is useful in investigations where additional data, such as gradient magnitudes and directions, are required Colour contrast is similarly useful in distinguishing the features of the schlieren field from one another and from the silhouettes of opaque objects The advantage of the perceived contrast of a colour scale versus that of a gray scale gives the effect of added sensitivity Also with the replacement of the knife-edge with a rainbow filter, diffraction effects are eliminated, which makes it more preferable for quantitative analysis The variation in the deflection of the beam at different locations in the test section is reflected as hue, saturation, and intensity variation of the colours in the screen instead of only the intensity variation as in the case of monochrome schlieren This avoids camera saturation to a greater extent and provides a larger scale of qualitative and quantitative evaluation Thus very high gradients can be effectively captured with this technique The colours also make it easier to refer to particular features of the image, and they sometimes help reconcile the conflicting requirements of high sensitivity and a broad measuring range A colour schlieren image is more evenly illuminated then a black-and-white image. Finally, colour schlieren images often have an aesthetic value in addition to their technical value, making them useful for teaching, demonstration, and a range of possibilities beyond those of a pure diagnostic tool One have to balance these advantages against the disadvantage of added optical complexity, the higher cost of colour image recording and the problems of colour reproduction

In development of a quantitative method, it is sought to produce a filter with colour transmission function at any special location described by a single parameter Additionally, this colour parameter should be insensitive to absolute optical intensities This eliminates numerous complications such as intensity fluctuations of the source, pixel-to-pixel variation in gain within a given detector array or from one detector to another, absorption or scattering of light within the test section, or second-order intensity variations resulting from asymmetric refractive index distributions A colour basis that avoids this difficulty, and the one that was selected for this application, is the hue-saturation-intensity (HSI) representation HSI parameters are obtained from direct transformation of the RGB tristimus values according to the following transformation equations by

Greenberg et al [22]

$$I = \frac{R + G + B}{3} \tag{3 4}$$

$$S = \frac{min(R,G,B)}{I} \tag{3 5}$$

$$H = cos^{-1}\left[\frac{1/2[(R-G) + (R-B)]}{(R-G)^2 + (R-B)(G-B)^{1/2}}\right] \tag{3 6}$$

A schematic representation of the relationship between the RGB and HSI colour-space models is shown in Figure 3 4   The vertex of the HSI cone is anchored at the intersection of the R, G, and B axes, and the projections of the central axis of the cone onto the R, G, and B axes are identical   An inspection of equation 3 6 confirms that the hue is independent of the absolute intensity   This can also be seen from figure 3 4, the hue, which is given by the polar angle relative to pure red, is unaffected by the total length (intensity) of the colour-space vector   Thus the RGB output of a conventional colour imaging array can be readily transformed in such a fashion as to produce a suitable one parameter measure of colour
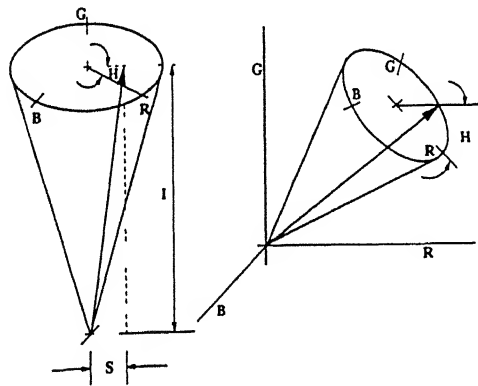

Figure 3 4. Graphic representation of the HSI colour space and its relationship to the R, G, B tristimus vectors

To describe a HSI filter, one must map the polar angle onto a one-dimensional coordinate. When this is done on one of the lateral dimensions of the filter plane, a cartesian or band like filter is produced   Similar to a conventional knife-edge stop, such a filter is sensitive to only the horizontal (or vertical) components of deflection   When mapped onto the radial coordinate, an axisymmetric, or circular filter is produced   A filter of this type responds to the absolute magnitude to

the resulting deflections but not to the orientation as the hue will be constant at every angles for the same radius

Filter Fabrication and Optimization

The colour filter should have a rainbow colour variation with a linear hue variation   Although H(R, G, B) is single valued and independent of I, it is a nonlinear function of its arguments   So the standard VIBGYOR colour distribution is used to achieve a distribution that is a linear function of position   The R, G, B components of the VIBGYOR colour distribution as downloaded from the net are as follows

Colour	Arguments		
	Red	Green	Blue
Violet	238	130	238
Indigo	75	0	130
Blue	0	0	255
Green	0	255	0
Yellow	255	255	0
Orange	255	165	0
Red	255	0	0

Table 3 1 R, G, B values of the VIBGYOR colour distribution

The R, G, B values of the VIBGYOR components are then linearly interpolated to get a array of 1200 rainbow colour variation   This array of R, G, B values are used to generate an one-dimensional cartesian filter   Figure 3 5(a) shows the colour one-dimensional cartesian filter   Figure 3 5(b) and 3 5(c) shows the RGB and the hue variation along the position   It can be seen that the hue variation is not a linear function of the position   But for an ideal filter it is desirable to remove this distortion   Specifically, the final filter should posses the property such that,

$$\frac{\partial H}{\partial x} = \text{constant} = -\frac{2\pi}{X_{max}}, \tag{3 7}$$

where x is the traverse coordinate in the filter plane over which H varies and X_{max} is the overall dimension of the filter   Departure from this behavior result in a detection sensitivity that is nonuniform over the measurement range
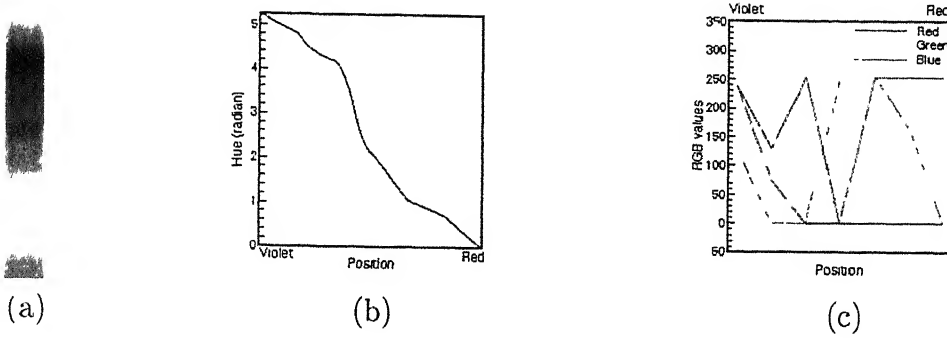
Figure 3 5   (a)Original filter, (b)Hue variation, (c)RGB variation

The optimized or the modified filter is then produced in the following manner   From equation 3 7 it follows that the desired value of hue at any position x on the final filter is given by

$$H(x) = 2\pi \left[1 - \frac{1}{X_{max}} |x| \right] \quad (3\ 8)$$

So the corrected input value of hue is now selected from the set of known output
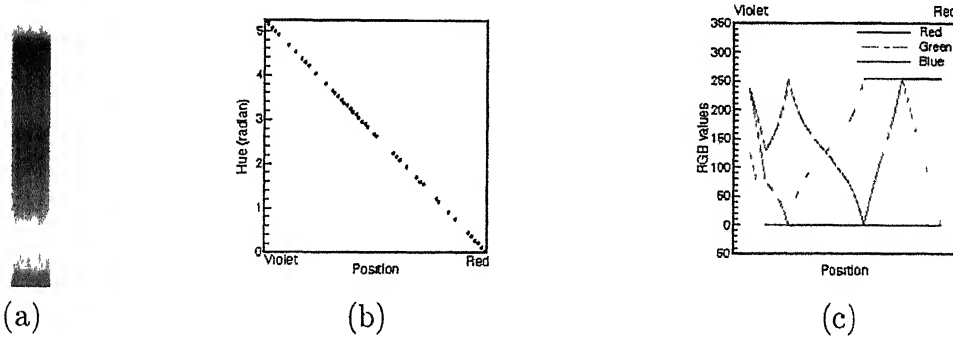

Figure 3 6   (a)Modified filter, (b)Hue variation, (c)RGB variation

values from the initial filter   Because the location corresponding to the occurrence of this measured values is known in absolute coordinates, the original magnitudes of R, G, B used to produce this values can now be retrieved and assigned to this spatial location on the optimized filter   This procedure is then repeated for each value of hue until the entire range from 0 to 2π had been completed   Because the RGB components at any position on the filter now correspond to actual measured values of hue, adherence to the behavior specified by equation 3 7 is now guaranteed   This is illustrated in figure 3 6   This array of modified rainbow colours can be manipulated to obtain different filters, like, cartesian, circular, square etc

The filter is then fabricated by displaying the filter image on a screen and taking the photograph of it on a colour slide film (Kodak Daylight Ektachrome, ASA 64) The room was maintained dark and the exposure along with the focus is varied to ensure the best possible resolution   Different size of the filter was obtained by varying the display size of the image and keeping the focusing of the camera constant

As the filter is ultimately rendered onto photographic film, the parametric relationship that provides a constant linear variation of hue becomes distorted in the development process Thus some imperfections may occur in the linearity of the hue verses position curve, attributed to the variations occurring in the photographic development process, or in roll-to-roll variations of the photographic emulsion itself. Furthermore, the occurrence of these imperfections places a boundary on the degree of linearity that can be achieved with this method The filter can also be remodified to improve the linearity

3.2   Schlieren Analysis

Schlieren image carries the information of the first derivative of the refractive index gradient. The index of refraction of a homogeneous medium is a function of the thermodynamic state, often only the density According to the Lorentz-Lorentz relation, the index of refraction of a homogeneous transparent medium can be obtained from

$$\frac{1}{\rho}\frac{n^2-1}{n^2+2} = \text{constant} \tag{3 9}$$

when $n \simeq 1$, this reduces to the Gladstone-Dale equation

$$\frac{n-1}{\rho} = Gl \tag{3.10}$$

or

$$\rho = \frac{n-1}{Gl} \tag{3.11}$$

The constant Gl, called the *Gladstone-Dale Constant*, is a function of the particular gas Instead of using Gl directly, the index of refraction at a standard condition n_0 is given by

$$n-1 = \frac{\rho}{\rho_0}(n_0-1) \tag{3 12}$$

or

$$\rho = \rho_0 \frac{n-1}{n_0-1} \qquad (3\ 13)$$

When the first derivative (let it be y) is determined in a schlieren apparatus, then using equation 3 11 and 3 12,

$$\frac{\partial \rho}{\partial y} = \frac{1}{Gl} \frac{\partial n}{\partial y} = \frac{\rho_0}{n_0-1} \frac{\partial n}{\partial y} \qquad (3\ 14)$$

3.2.1   Monochrome Schlieren

To study the schlieren systems, the path of a light beam in a medium whose index of refraction is a function of position must be analyzed   If the Z-axis is the direction of the undisturbed ray then the total angular deflection measured beyond the working section of the test section in XZ and YZ planes are denoted respectively as ε_x and ε_y are

$$\varepsilon_x = \frac{1}{n_0} \int \frac{\partial n}{\partial x} dz \qquad\qquad \varepsilon_y = \frac{1}{n_0} \int \frac{\partial n}{\partial y} dz \qquad (3\ 15)$$

where n_0 is the refractive index of the air surrounding the test section   It can be noted that the light beam is turned in the direction of increasing index of refraction   In most media this means that the light is bent towards the region of higher density

If no disturbance is present, then ideally the light beam at the focus of second concave mirror would be as shown in figure 3 2, with dimensions a_0 by b_0 which are related to the initial source dimensions a_s by b_s by

$$\frac{a_0}{a_s} = \frac{b_0}{b_s} = \frac{f_2}{f_1} \qquad (3\ 16)$$

where f_1 and f_2 are the focal lengths of the first and second concave mirror, respectively   The knife-edge is adjusted, when no disturbance is present, to cut off all but an amount a_K of the height a_0 The illumination at the screen when no knife-edge is present is I_0, and with the knife-edge inserted in the focal plane is

$$I_K = \frac{a_K}{a_0} I_0 \qquad (3.17)$$

The light passing from through each section of the test region comes from all parts of the source Thus, at the focus not only is the image of the source composed of light coming from the whole field of view, but light passing through every point in the field of view gives an image of the source at the knife-edge If the light beam at a position x, y in the test region is deflected by an angle ε, then, the image of the source coming from that position will be shifted at the knife-edge by an amount

$$\Delta a = \pm f_2 \varepsilon \qquad (3\ 18)$$

where the sign is determined by the orientation of the knife-edge It is positive when $\varepsilon > 0$ gives $\Delta \varepsilon > 0$, and negative if the knife-edge is reversed so that $\varepsilon > 0$ leads to $\Delta \varepsilon < 0$ The illumination at the image of position x,y on the screen will be

$$I_d = I_K \frac{a_K + \Delta a}{a_K} = I_K \left(1 + \frac{\Delta a}{a_K}\right) \qquad (3\ 19)$$

where Δa is positive if the light is deflected away from the knife-edge, and negative if the light is deflected towards the knife-edge The relative intensity or contrast is

$$\text{Contrast} = \frac{\Delta I}{I_K} = \frac{I_d - I_K}{I_K} = \frac{\Delta a}{a_K} = \pm \frac{\varepsilon f_2}{a_K} \qquad (3.20)$$

using equation 3 18

Combining equation 3 15 and 3 20 gives

$$\text{Contrast} = \frac{\Delta I}{I_K} = \pm \frac{f_2}{a_K n_0} \int \frac{\partial n}{\partial y} dz \qquad (3\ 21)$$

Assuming a two-dimensional field with $\partial n / \partial y$ constant at a given x, y position over the length L in z direction,

$$\text{Contrast} = \pm \frac{f_2}{a_K} \frac{1}{n_0} \frac{\partial n}{\partial y} L \qquad (3.22)$$

This equation holds for every x, y position in the test section and gives the contrast at the equivalent position in the image of the screen For a gas, equation 3 21 can be rewritten, using equation 3 14,

$$\frac{\Delta I}{I_K} = \pm \frac{f_2}{a_K n_0} \frac{n_0 - 1}{\rho_0} \int \frac{\partial \rho}{\partial y} dz \qquad (3\ 23)$$

and equivalent to equation 3 22

$$\frac{\Delta I}{I_K} \simeq \frac{f_2}{a_K} \frac{n_0 - 1}{\rho_0} \frac{\partial \rho}{\partial y} L \qquad (3\ 24)$$

taking $n_0 \simeq 1$

For a gas at constant pressure,

$$\frac{\Delta I}{I_K} \simeq \mp \frac{f_2}{a_K} \frac{n_0 - 1}{\rho_0} \frac{P}{RT^2} \frac{\partial T}{\partial y} L \qquad (3.25)$$

The equations can be solved using partial differential equations Since n and its derivatives vary somewhat with wavelength, it is preferable that the light source is monochromatic

Analysis of Schlieren Image

At the beginning of an experiment an initial image is captured with the CCD camera and its associated softwares, when no optical disturbance is present in the test section The A/D adaptor card digitizes the image in the scale of 0-255 GIMP is an Linux based image processing software which converts the image to its corresponding intensity value for an monochrome image Thus we get an matrix of numbers containing the intensity information of the initial image There will be a change in intensity when an optical disturbance is placed in the test section A final intensity distribution is obtained in the screen as an image The image captured by the CCD camera can be converted to an matrix of the final intensity values Now the matrices can be operated on to extract the information of the properties

Thus, equation 3 22 can be used to get the refractive index field when one of the boundary condition is known Equation 3.24 can be used to directly get the density information Gas equation can now be used to get the temperature values from the density information

3.2.2   Colour Schlieren

In colour schlieren, the deflection of the light beam leads to a variation in the hue instead of the intensity as in the case of monochrome schlieren From figure 3 7, if the light beam at any position x, y in the test section is deflected by an angle

ε, then the shift in the light beam at the position of the colour filter will be by an amount given by

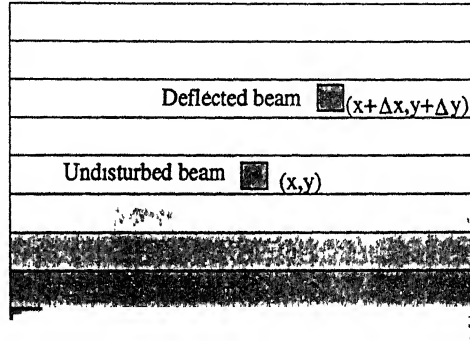$$\Delta a_x = f_2 \varepsilon_x \qquad\qquad \Delta a_y = f_2 \varepsilon_y \qquad\qquad (3\ 26)$$

Figure 3 7 View of deflected and undisturbed beams at the colour filter

The quantities Δa_x and Δa_y can be obtained from the variation of hue at the x, y position of the image A two-dimensional filter would be required to capture both these components A one-dimensional cartesian filter can be used to get any one of the components Once the colour filter is calibrated, the position of the light can be related to the hue variation of the image Thus a difference in the hue will give the absolute deflection in any of the directions

Now from equation 3 15,

$$\Delta a_x = \frac{f_2}{n_0} \int \frac{\partial n}{\partial x} dz \qquad\qquad \Delta a_y = \frac{f_2}{n_0} \int \frac{\partial n}{\partial y} dz \qquad\qquad (3.27)$$

Assuming a two-dimensional field with $\partial n/\partial y$ constant at a given x, y position over the length L of the test section in the z direction,

$$\Delta a_x = \frac{f_2}{n_0} \frac{\partial n}{\partial x} L \qquad\qquad \Delta a_y = \frac{f_2}{n_0} \frac{\partial n}{\partial y} L \qquad\qquad (3.28)$$

For a gas, the above equation can be rewritten, using equation 3 14

$$\Delta a_x = \frac{f_2}{n_0} \frac{n_0 - 1}{\rho_0} \frac{\partial \rho}{\partial x} L \qquad\qquad \Delta a_y = \frac{f_2}{n_0} \frac{n_0 - 1}{\rho_0} \frac{\partial \rho}{\partial y} L \qquad\qquad (3.29)$$

For a gas at constant pressure,

$$\Delta a_x = \frac{f_2}{n_0} \frac{n_0 - 1}{\rho_0} \frac{P}{RT^2} \frac{\partial T}{\partial x} L \qquad \qquad \Delta a_y = \frac{f_2}{n_0} \frac{n_0 - 1}{\rho_0} \frac{P}{RT^2} \frac{\partial T}{\partial y} L \qquad (3\ 30)$$

Calibration of Colour Filter

Calibration of the colour filter is done to set up the relationship between the hue variation and the corresponding position Thus, a difference in the initial and the final hue correlate to the absolute displacement of the light beam This section discusses the calibration of an one dimensional cartesian filter The same method can be applied also for calibrating a two dimensional filter The calibration is carried without the presence of any optical disturbance in the test section so that a single value of hue variation is obtained at the viewing screen

First the colour schlieren apparatus is set up The colour filter is placed in the focus of the decollimating lens It is mounted on a filter holder which have provision for traversing in a two-dimensional plane using graduated screw The least count for traversing was 0 02 mm When power is supplied to the light source, it emits light beam at high power, which is collimated by a collimator lens system The decollimating lens focusses the beam at the colour filter A coloured image is formed at the viewing screen behind the filter The image is captured by a CCD camera The averaged hue value is recorded, and the corresponding position of the filter is specified as the zeroth or the initial position Now the filter is given a vertical movement (for a vertical filter, else give a horizontal movement) of 0 02 mm with the micrometer arrangement There will be an change in the hue for the image, as light passes through a different position and colour in the filter The hue value is recorded corresponding to the 0 02 mm displacement of the filter. Now, a new vertical displacement can be given and this steps can be repeated until the next extreme colour limit is approached Now the hue and position information can be used to get a hue vs position calibration curve for the filter For an ideal filter, this curve should vary linearly But, there will be minor perturbations in the calibration curve due to the errors included in developing the filter on a photographic film The calibration curve can be used to generate an modified filter with the perturbations linearized. All the filters will

have their own calibration curve and hence should be calibrated separately Once the calibration curve is obtained, a change in the hue variation can be directly related to the corresponding change in the absolute position of the light beam

Chapter 4

Results and Discussion

In the present work, quantitative analysis of the schlieren images has been carried out for the convection in a rectangular cavity. The results have been benchmarked with similar Mach-Zehnder interferometry experiments. The benchmarked algorithm was used to study convection currents around an KDP crystal growing from its aqueous solution. The convection currents were related to the quality of the crystal. Colour schlieren was used to visualize similar convection currents in the crystal growth process

4.1   Convection in Rectangular Cavity

The benchmarking experiments in the present work have been performed at six Rayleigh numbers namely 1.40×10^4, 2.70×10^4, 5.10×10^4, 8.50×10^4, 1.13×10^5 and 1.40×10^5 with air as the working medium and at Rayleigh numbers of 2.50×10^6, 4.40×10^6, 2.50×10^6, 2.50×10^6, 2.50×10^6 and 2.50×10^6 with water as the working medium. The value realized in the present experiments were quite large in comparison to the critical Rayleigh number of 1707 for the infinite fluid layer at the onset of convection by Gebhart et al [2]

In the present work, experiments in a long two-dimensional differentially heated fluid cavity have been performed to study the transients and steady state behavior of the flow field. This section discusses the transient evolution and

steady state nature of the thermal field, the inter-relation among the three imaging technique in the context of the steady state images, qualitative interpretation of the thermal field observed in the experiments Quantitative analysis of the steady state images has also been discussed for the lower range of Rayleigh numbers (corresponding to $\Delta T \leq 20$ K) for experiments with air as the working fluid and interferometry and schlieren as the imaging technique The results obtained in terms of temperature profiles and average Nusselt numbers from the two imaging techniques have been compared with the numerical solution obtained using commercial CFD package FLUENT 5 5 Qualitative interpretation of the steady state images has been discussed for the experiments in air with interferometry, schlieren and shadowgraph as the imaging technique and compared with the artificially generated schlieren and shadowgraph images using numerical solution In the experiments with water, transient evolution of the thermal field has been visualized using shadowgraph as the imaging technique and the qualitative comparison with numerically generated shadowgraphs has been made and discussed in the present section

4.1.1 Experiments with Air

As mentioned earlier, fringes in an interferogram can be considered as isotherms when the interferometric experiments are performed in infinite fringe setting mode Hence a direct measure of temperature/ refractive index field can be had from an interferogram In contrast, intensity distribution in a schlieren image corresponds to the gradient of the refractive index from which temperature/refractive index field can be deduced In the present work, schlieren images for three Rayleigh numbers (Ra = $1 40 \times 10^4$, $2 70 \times 10^4$ and $5 10 \times 10^4$) have been quantitatively analysed to recover the temperature field as discussed in the following section

Convection at low Rayleigh numbers

At low Rayleigh numbers, steady state convection pattern is achieved after 3-4 hours of experimental run time Figure 4 1 shows the schlieren images for
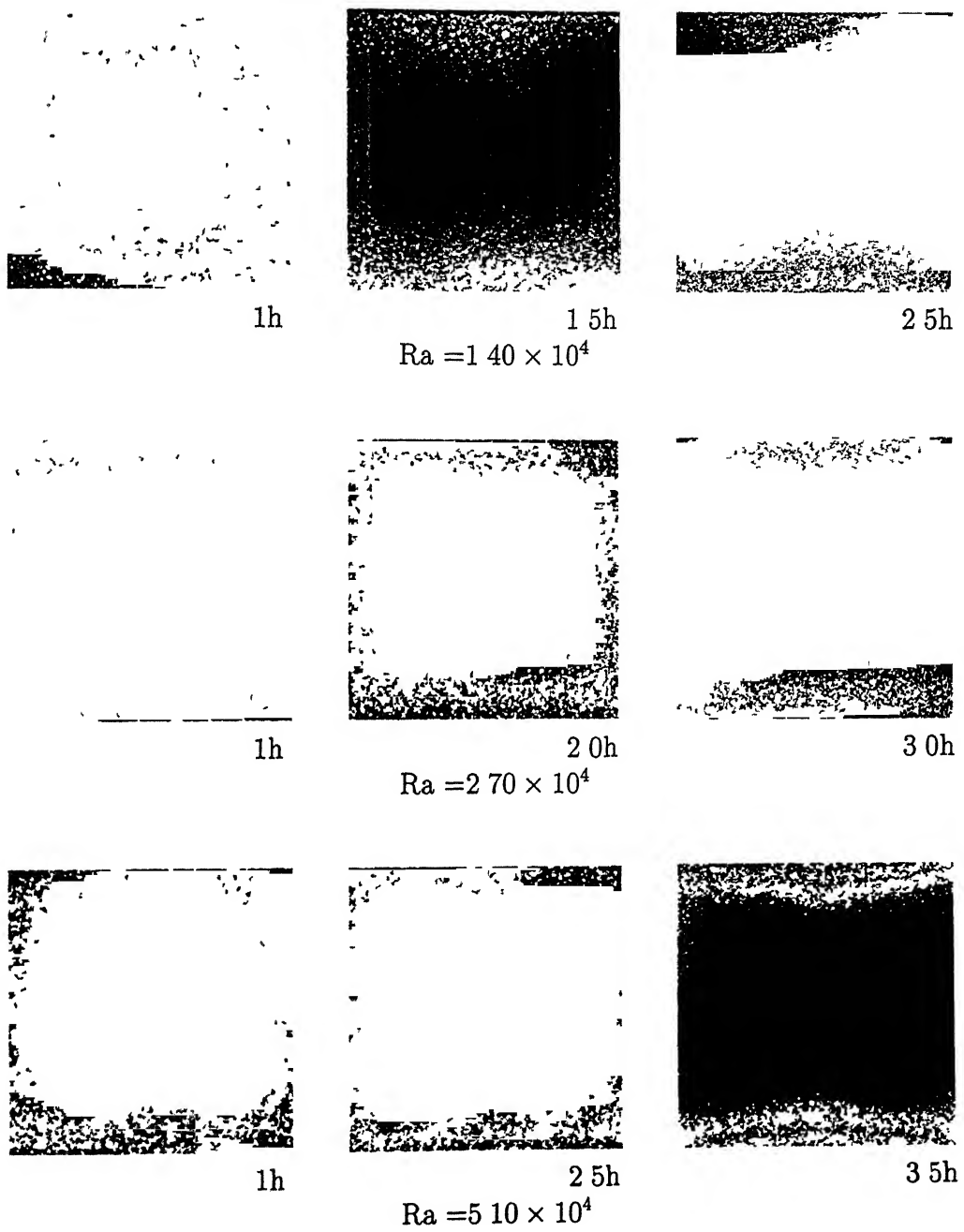
transient evolution of the flow field

$$Ra = 1 40 \times 10^4$$

$$Ra = 2 70 \times 10^4$$

$$Ra = 5 10 \times 10^4$$

Figure 4 1   Schlieren image for transient evolution of flow field

5K   10K   20K

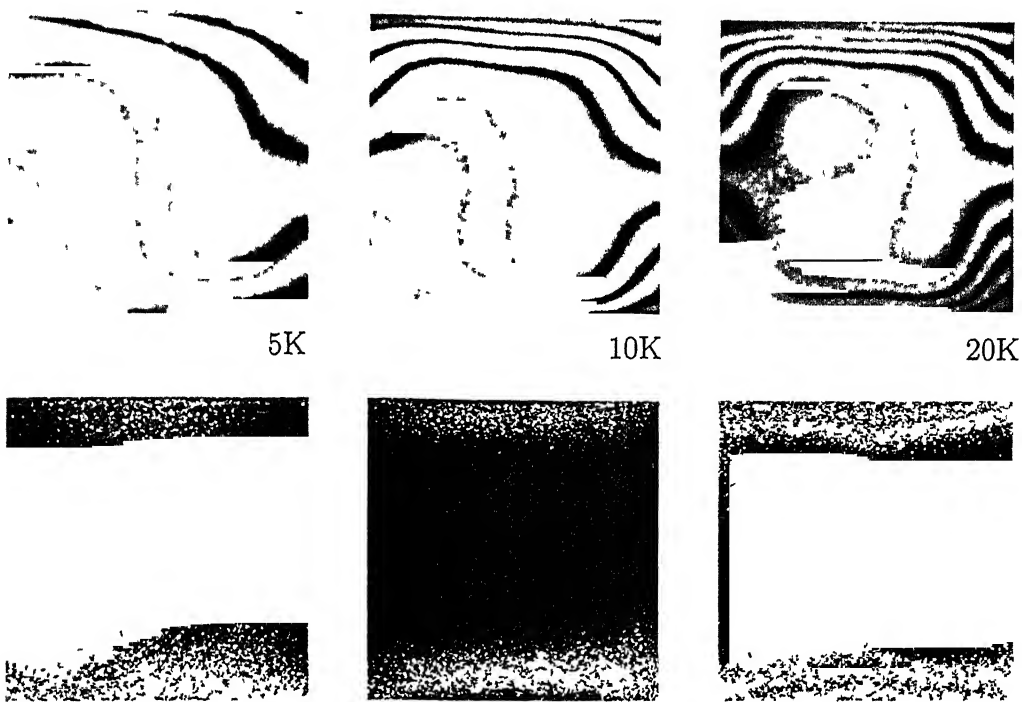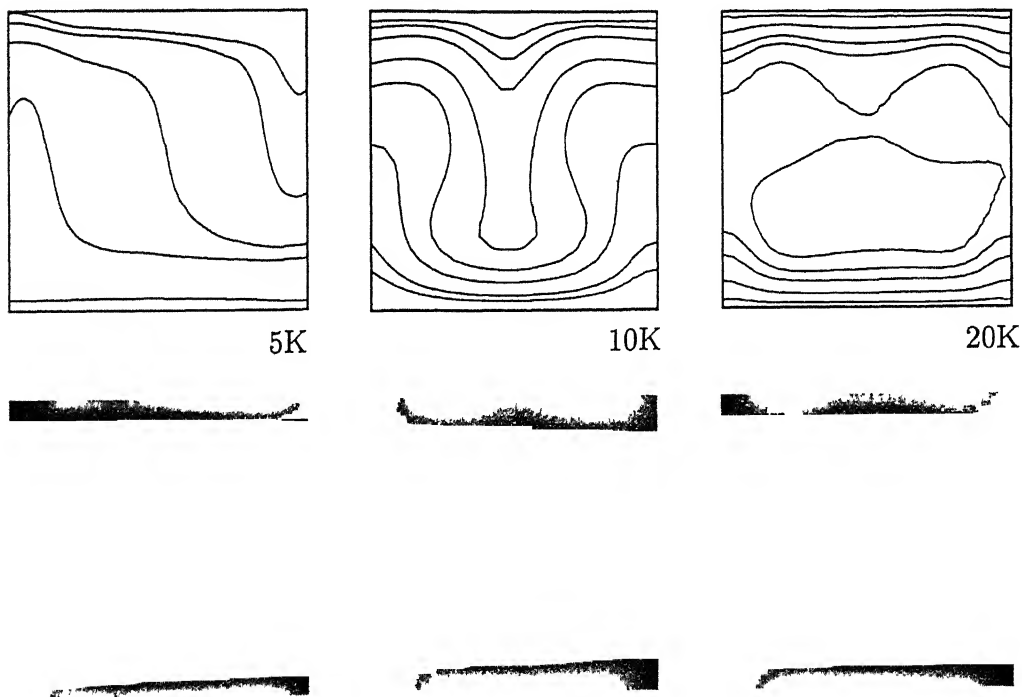Figure 4 2 Experimental interferometry and schlieren Image

5K   10K   20K

Figure 4 3 Numerical interferometry and schlieren Image

Figure 4 2 shows the steady state long time interferometric and schlieren images for the lower range ($1\,40 \times 10^4$ to $5\,10 \times 10^4$) of Rayleigh numbers At $Ra = 1\,40 \times 10^4$, the interferogram reveals that the number of fringes are quite low and the spacing between the fringes is almost uniform resulting into uniform thermal gradients existing in the entire cavity The fringe patterns were observed to be quite steady in the experiments Similar trend can be depicted from the schlieren image where comparatively brighter regions correspond to the regions of high thermal gradients Though these regions are mainly concentrated near the top and bottom walls, one can see the spread of high intensity in the core region also (a feature which was absent at higher Rayleigh numbers) This can be attributed to the thermal gradients prevailing in the entire cavity, a fact also reflected by the interferogram where an uniform fringe spacing was observed The numerically generated schlieren image also reveals the similar behavior of the flow field Qualitatively a good match can be seen between the experimental and numerically generated schlieren images as far as distribution of high intensity regions is concerned. As the Rayleigh number is increased, a definite increase in the number of fringes can be seen from the interferometric images The fringe spacings near the top and bottom walls of the cavity is less than the spacing in the central region This is expected, because near the boundaries heat transfer rates are higher, in the central region of the test section, heat transfer is practically absent Corresponding schlieren images (experimental as well as numerically generated) indicate the presence of high thermal gradients near the horizontal walls in the form of comparatively brighter zones and a darker central core region where the gradients are practically absent. During the experiments, the convective field was observed to be almost steady at $Ra = 2.70 \times 10^4$ whereas mild unsteadiness was seen at $Ra = 5\,10 \times 10^4$ with the fluid showing some lateral movement.

Figure 4.4 shows the distribution of temperature field in the form of contours recovered from the experimentally recorded schlieren images The dominant features of the convective field extracted from a schlieren image reasonably match with those in the interferograms and the comparison looks qualitatively meaningful. At lower Rayleigh number ($Ra = 1\,40 \times 10^4$ to $5\,10 \times 10^4$), the temperature contours generated from schlieren image reflect the fact that the thermal field is almost unicellular with the fluid reaching maximum at one side of the cavity and
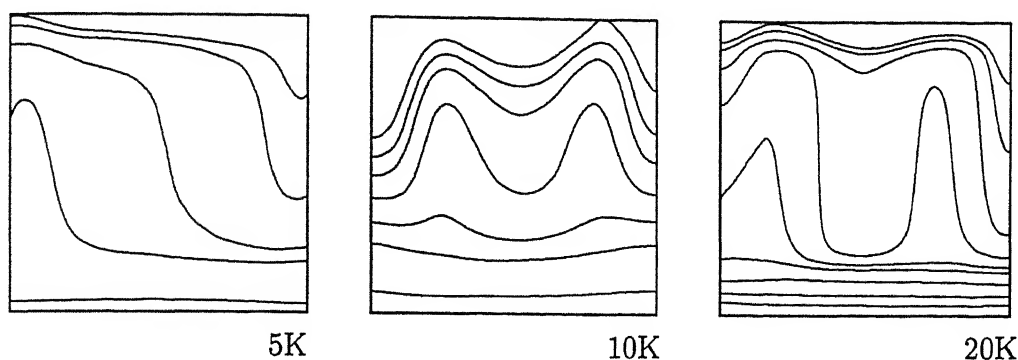
5K   10K   20K

Figure 4 4 Temperature contours from the schlieren image

minimum on the opposite side As the Rayleigh number increases, temperature contours show a definite increase in the number of fringes and relatively straight fringes start to deform giving a wavy appearance similar to that observed in the interferometric images with fluid reaching maximum on the two sides of the cavity and minimum at the mid-plane thus implying the bicellular nature of the thermal field High thermal gradient regions near the horizontal walls of the cavity have been revealed by comparatively denser temperature contours indicating the regions of high heat flux Similar trend can be observed in the interferometric images with the fringes being denser near the walls and gradually moving apart as one reaches the core region of the cavity

Local and average heat transfer rates at the bounding walls of the cavity have been calculated in terms of Nusselt number defined by equation 2.1 Figure 4 5(b) shows the variation of Nusselt number at the upper and lower walls as a function of width of the cavity calculated from experimentally recorded interferometric and schlieren images for three values of Rayleigh numbers Variation in the local values of Nusselt numbers calculated from an interferometric image is comparatively larger at lower values of Rayleigh numbers This can be attributed to the presence of very few fringes in the interferogram, hence making the quantitative analysis more error-prone Wavy appearance of the variation of local Nusselt numbers with peaks and valleys can be associated with the heat transfer from the lower to the upper plate by the buoyancy-driven convective fluid Regions of high heat transfer on one wall correlate well within acceptable limit with those of low heat transfer on the other
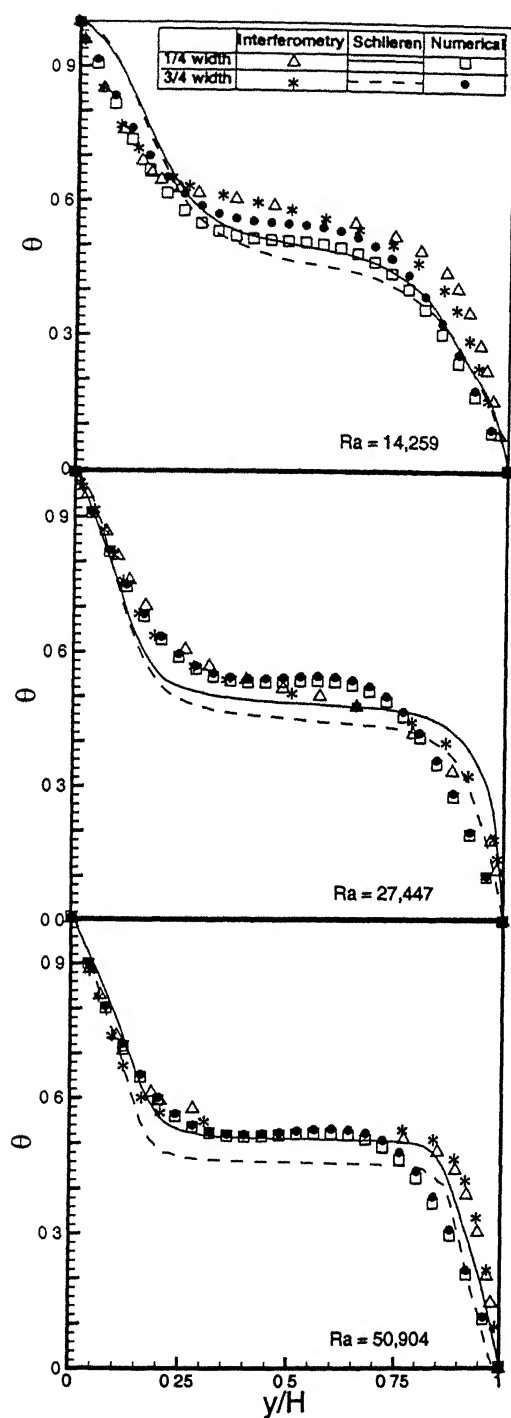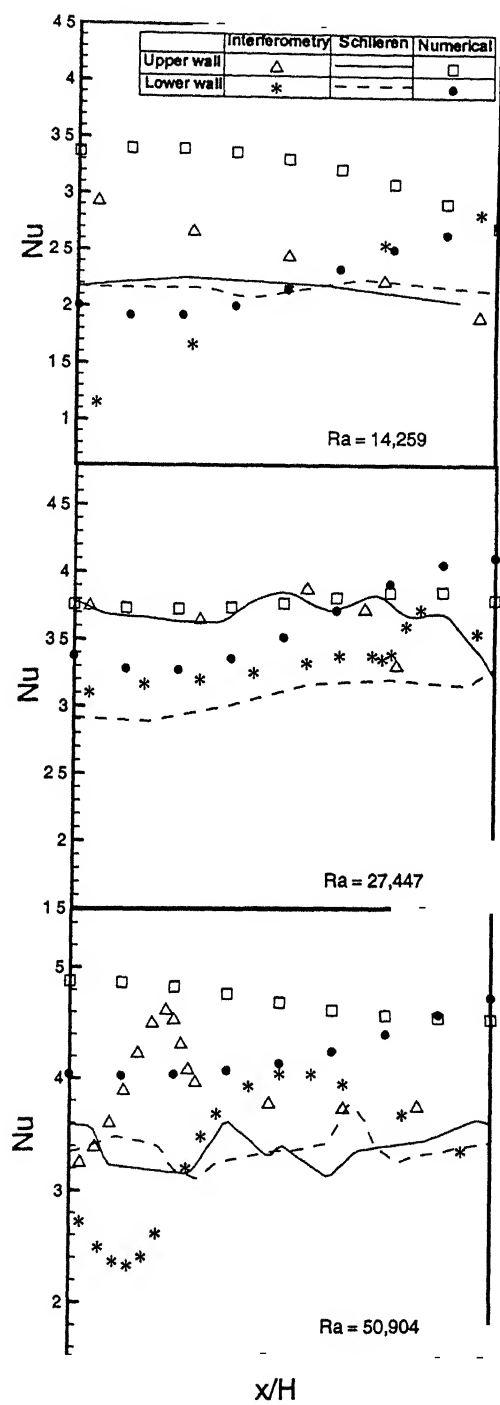
Figure 4 5   (a)Temperature profile, (b)Nusselt number of the rectangular cavity

Table 4 1 summarizes the wall-averaged Nusselt numbers calculated from the two optical techniques and using the correlation given by Gebhart et   al (equation 2 2)   As can be seen, the average Nusselt numbers calculated using the two optical techniques reasonably match with each other with a maximum error of $\pm 5\%$ which occurs at lower value of Rayleigh number (Ra = 1 40 × 10^4) mainly because of the lesser number of fringes in the interferometric image   Table 4 1 also shows the average Nusselt number of the correlation with an uncertainty level of ± 20 %   The Nusselt number calculated in the present experiments is within the uncertainty limits of the published correlation

Ra	Nu (Cold)		Nu (Hot)		Reference
(Air)	Interferometry	Schlieren	Interferometry	Schlieren	
1 40 × 10^4	2.38	2 28	1 965	2.07	2 615
2 70 × 10^4	3 32	3 5	3 13	3.1	3.03
5 10 × 10^4	3 56	3 37	3 51	3 38	3 45

Table 4.1 Heat transfer rates in terms of Nusselt numbers

Figure 4 5(a) shows the steady state non-dimensional temperature profiles plotted as a function of the vertical coordinate for two columns (1/4 and 3/4 of the cavity width) for the three Rayleigh numbers   Temperature profiles obtained from the two optical techniques and numerical simulation have been considered and compared with each other   The inverted S-shaped profile, a characteristic of buoyancy-driven convection is reflected from all the three approaches   The slopes of the individual curves near the walls give a measure of the net heat transfer across the cavity at steady state from the hot surface to the cold   It has to be noticed here that these temperature profiles have been shown for two different columns located near the opposite walls of the cavity, hence there is a slight difference in the individual profiles as far as slopes near the walls are concerned. On the other hand, the wall-averaged Nusselt numbers summarized in Table 4 1 have been calculated by averaging the local Nusselt number values at several closely spaced columns along the width of the cavity, hence a reasonably good match has been observed in the average heat transfer rates at the walls A comparatively good match in the profiles obtained from schlieren analysis and numerical simulation can be observed whereas the profiles calculated from the

interferometric images shows slight variations This can be attributed to the fact that one gets a field values at each and every pixel of a schlieren image and from numerical simulation whereas in interferometric image, the information is located on the fringes only and one has to use interpolation schemes to get the field values at intermediate points inducing a source of error Moreover at low Rayleigh numbers, the presence of fewer number of fringes also make the calculations error-prone

Convection at higher Rayleigh numbers

Previous subsection discussed the quantitative behavior of the convective field in terms of wall heat transfer rates and non- dimensional temperature profiles at lower range of Rayleigh numbers In the present section, convective field at higher Rayleigh numbers (Ra $=8 50 \times 10^4, 1 13 \times 10^5$ and $1 40 \times 10^5$) have been considered and qualitatively analyzed in terms of the features like unsteadiness in the flow, onset of periodicity etc. At these Rayleigh numbers, the flow was seen to be unsteady making it difficult to quantitatively analyse the convective field Also refraction effects were observed to be so high that the boundaries of the fluid cavity were seen to be deformed when imaged on the computer screen Hence a qualitative comparison has been made among the three optical techniques and the long time convective field images have been compared with the numerically generated ones in terms of the dominant features of the flow field Apart from interferometry and schlieren, shadowgraph imaging technique has also been employed because of the presence of high thermal gradients in the flow field

Figure 4 6 shows long time convective field images recorded using the three optical techniques Corresponding numerically generated schlieren/ shadowgraph images have been shown in Figure 4 7 At Ra $=8 50 \times 10^4$, the interferometric image shows nearly straight fringes parallel to the horizontal walls The flow field is symmetric about the centerline of the cavity Near the cold wall, the fringes are denser near the mid-plane of the cavity and the spacing between the fringes gradually decreases as the fluid approaches the side walls These two locations correspond to the high (near the mid-plane) and low (near the side walls) thermal gradient regions
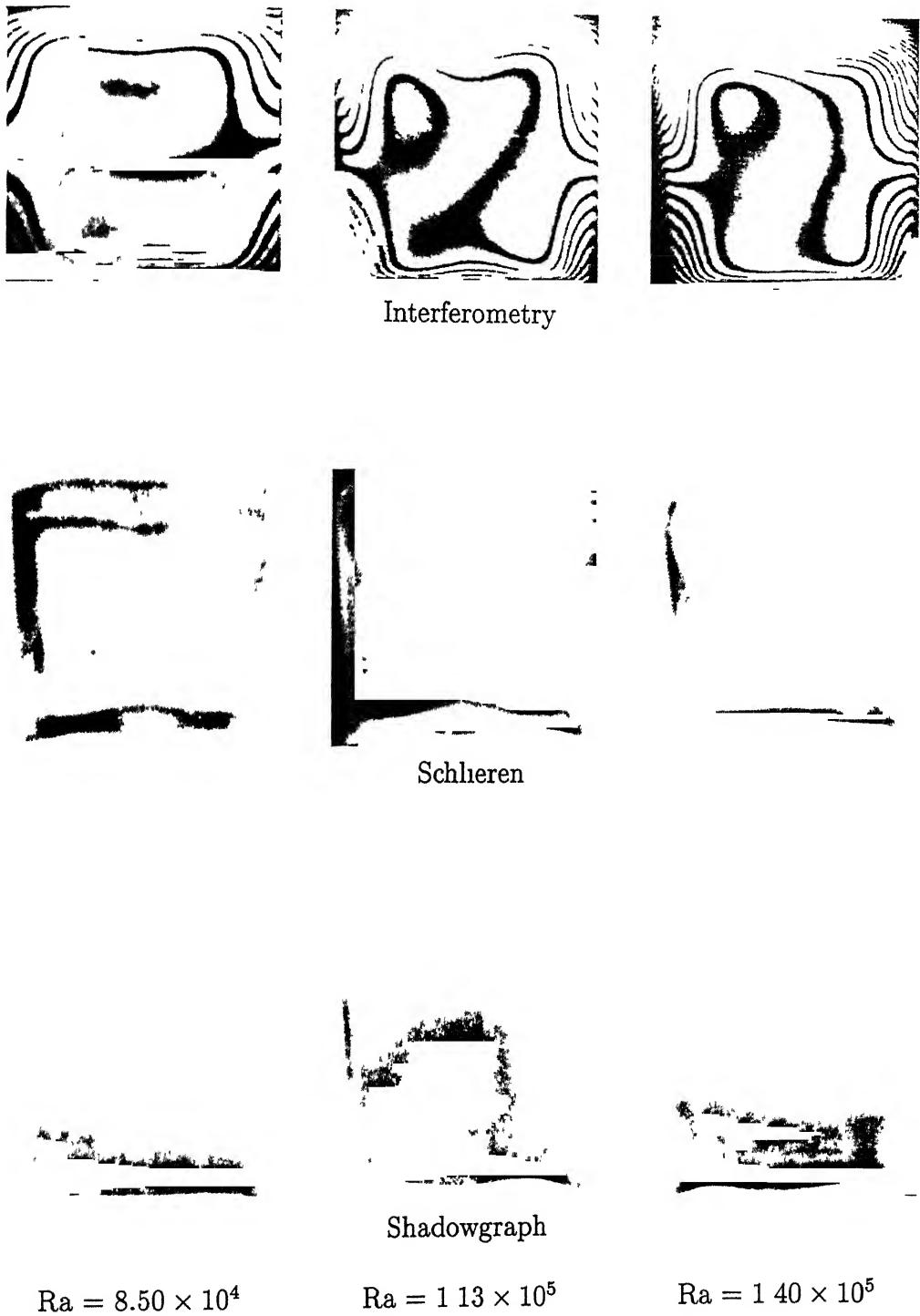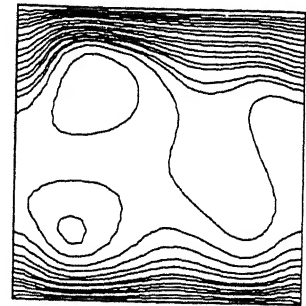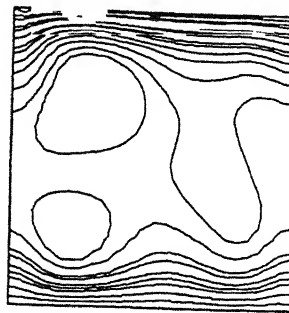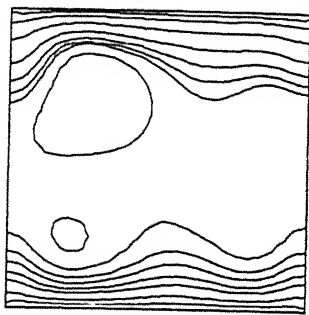
Interferometry

Schlieren

Shadowgraph

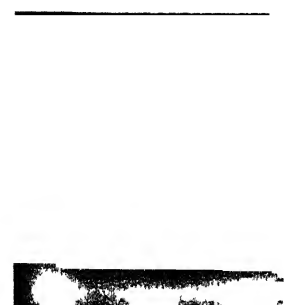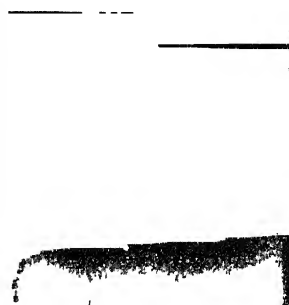| Ra = 8.50×10^4 | Ra = $1\,13 \times 10^5$ | Ra = $1\,40 \times 10^5$ |

Figure 4 6   Experimental Interferometry, Schlieren and Shadowgraph image

Interferometry

Schlieren

Shadowgraph

Ra = 8 50 × 10⁴   Ra = 1 13 × 10⁵   Ra = 1 40 × 10⁵

Figure 4 7 Numerical Interferometry, Schlieren and Shadowgraph Image

Towards the higher values of Rayleigh numbers, a definite deformation in the shape of the fringes in the case of interferometry and intensity patterns in schlieren and shadowgraph images was observed The fringes in an interferogram deform to form two peaks near opposite side walls of the cavity and a trough at the mid-plane, hence a roll can be identified as the locations where the fringe slope is zero Corresponding schlieren and shadowgraph images reveal the presence of rolls in the form of relatively darker patches near the two side walls of the cavity at higher Rayleigh numbers Using the three optical methods, the roll sizes were calculated with respect to the cavity size for the three Rayleigh numbers and have been quoted in Table 4 2 The roll size can be determined directly from the optical images since the fringes as well as the intensity fields should turn along at corners with the local velocity vector A monotonous decrease in the dimension of the roll can be observed as one approaches higher values of Rayleigh numbers This trend is qualitatively meaningful because at low Rayleigh numbers, the patterns reflected by the three imaging techniques are relatively straighter along the width of the cavity giving indications of the flow field being unicellular with fluid accelerating on one side of the cavity and descending near the opposite side With an increase in the Rayleigh number, the fluid shows a dip near the mid-plane of the cavity and again rises as it approaches the opposite side wall with the unicellular patterns starting to bifurcate to result into bicellular convective field, giving rise to a decrease in the roll size Table 4 2 also shows the roll sizes calculated from the numerical simulation A reduction in size was also observed with the increase in Rayleigh number

Rayleigh number (Air)	Roll size (relative to cavity depth)			
	Interferometry	Schlieren	Shadowgraph	Numerical
8.50×10^4	0.270	0 278	0 310	0 304
$1 13 \times 10^5$	0 258	0 252	0 252	0 296
$1 40 \times 10^5$	0 210	0 242	0 220	0 256

Table 4 2. Non-dimensional roll size from the three optical techniques

In the range ($8 50 \times 10^4$ to 1.40×10^5) of Rayleigh numbers, the flow was seen to be unsteady and the convective field exhibited some time dependence. This time dependence was more pronounced at the two higher values of Rayleigh

numbers where a definite periodicity was observed in the flow field To get a clear picture of the flow field, a sequence of convective field images at Ra =1 13×10^5 and 1 40 × 10^5 were followed and the oscillations in the flow were carefully observed The time period of these oscillations have been calculated (by visual inspection at Ra =1 13 × 10^5 and by following the intensity variation at a particular region in the flow field at Ra =1 40 × 10^5) and has been non-dimensionalised using thermal diffusion time (h^2/α). In case of numerical simulation, the variation of temperature is plotted with respect to time for a region in the flow field The dominant frequency was extracted by plotting the data The plots are shown in appendix-A A comparison of these non-dimensional time period in terms of Fourier number has been made with those quoted by Krishnamurti for comparable values of Rayleigh numbers and is shown in Table 4 3 It can be seen that the period of oscillation calculated from the present study are slightly lower than the published values This difference can be attributed to the difference in the cavity size used in the respective studies Present work makes use of a cavity which is 44 × 3 216 cm in plan whereas the corresponding dimensions in the study made by Krishnamurti were 51 × 49 cm Comparatively lower values of time period of oscillations observed in the present study are mainly because of the lower size of the cavity wherein the boundary walls play significant role in deciding the strength of these oscillations

Rayleigh number (Air)	Non-dimensional time period		
	Present Study	Numerical	Krishnamurti (1970)
1.13 × 10^5	0 038	0 0461	0 055
1.40 × 10^5	0 015	0 0346	0 030

Table 4 3 Non-dimensional time period for two Rayleigh numbers

4.1.2 Experiments with Water

Experiments with the test cell filled with water are reported in the present section Rayleigh numbers employed are Ra =2 50 × 10^6, 4 40 × 10^6, 5 40 × 10^6, 7.50 × 10^6, 9.80 × 10^6 and 13.50 × 10^6 Figure 4 8 and 4 9 shows the experimental and numerically generated interferometry and schlieren images for a higher value of Rayleigh number The presence of high thermal gradients leading to

high refraction effects makes it difficult to visualize the flow field using schlieren techniques as the boundaries of the cavity deform severely   Hence a shadow-

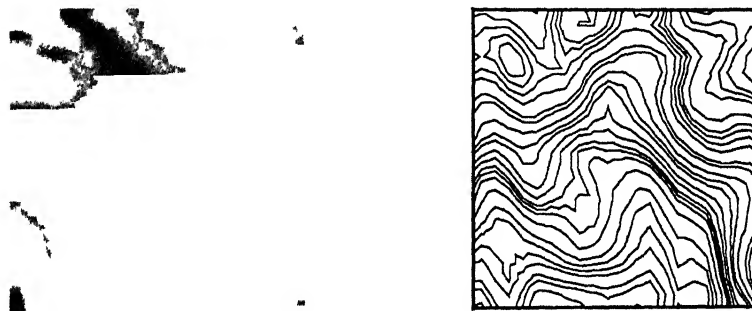Figure 4 8   Experimental schlieren and interferometry image at high Rayleigh number (Ra = 13 50 × 10^6)

Figure 4 9   Numerical schlieren and interferometry image at high Rayleigh number (Ra = 13 50 × 10^6)

graph system was employed as the imaging technique in these experiments   Long time convection patterns were recorded to let the initial transients die out   The experimentally recorded shadowgraph images have been qualitatively compared with those artificially generated from the numerical solution for Ra =2 50 × 10^6 and 13 50 × 10^6

Figure 4 10 shows long time convection patterns for the entire range of Rayleigh numbers   It was observed that at Ra =2 50 × 10^6 the thermal field was almost steady with the passage of time. Uniform distribution of intensity in the core region of the cavity was seen in the shadowgraph images   Relatively higher intensity narrow strip parallel to hot wall of the cavity represent the localized high thermal gradients that result in nonuniform deflection of light beam in the downward direction   The thickness of the bright band near the bottom plate was

seen to increase towards higher range of Rayleigh numbers   At Ra =4 40 × 10⁶

| 2 50 × 10⁶ | 4 40 × 10⁶ | 5 40 × 10⁶ |

| 7 50 × 10⁶ | 9 80 × 10⁶ | 13 50 × 10⁶ |
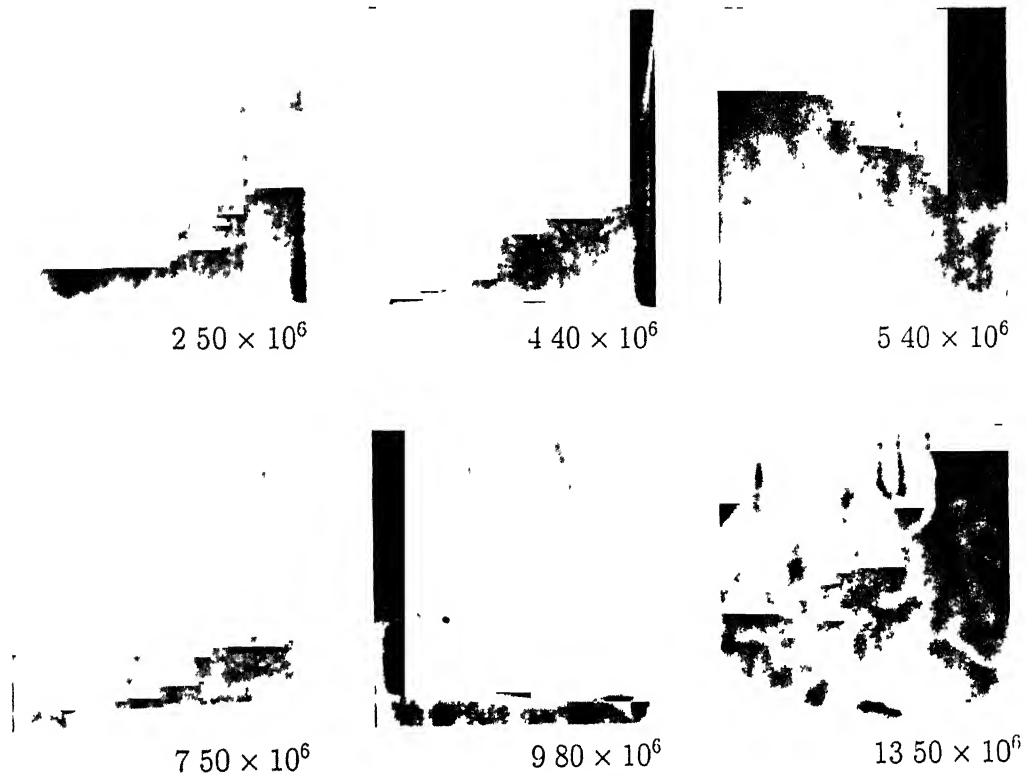
Figure 4 10 Shadowgraph images for entire range of Rayleigh numbers

signs of mild unsteadiness in the flow field were observed with a convective plume
arising from the bottom plate and advancing towards the cold top plate   This
phenomenon was more pronounced at higher (5 40 × 10⁶ to 7 50 × 10⁶) Rayleigh
numbers wherein more than one number of convective plumes were observed The
flow field showed high degree of unsteadiness in the form of random movement
of the convective fluid   Shadowgraph images corresponding to these Rayleigh
numbers shown in the figure indicate the presence of these strong plumes in the
form of random distribution of bright and dark patches   Just after the onset
of unsteadiness, weak periodicity was observed in terms of the origin of these
convective plumes from the lower wall of the cavity for Ra≤7 50 × 10⁶ in some
of the experiments Visual inspection was made to calculate the non-dimensional
time period of this periodic origin of the plume and was found to be of the order of
≈ 1 10 × 10⁻³ At higher range (9 80 × 10⁶ to 13 50 × 10⁶) of Rayleigh numbers,
the flow field was seen to be completely turbulent with the movement of the
plumes being quite vigorous and completely random This can be treated as an

intermediate step towards the chaotic flow with an increase in Rayleigh number
Corresponding shadowgraph images show random distribution of the intensity
field Bright intensity streaks can be considered to represent relatively higher
thermal gradients With an increase in the Rayleigh number, the shadowgraph
images show an increase in the thickness of thermal boundary layer (represented
by the bright strip) near the bottom plate of the cavity which in turn reflect the
extent of the spread of thermal gradients from the hot to the cold wall of the
cavity Numerically generated shadowgraph images have also been shown in the
Figure 4 11 for Ra $=2$ 50×10^6 and 13 50×10^6 Qualitatively, a good match
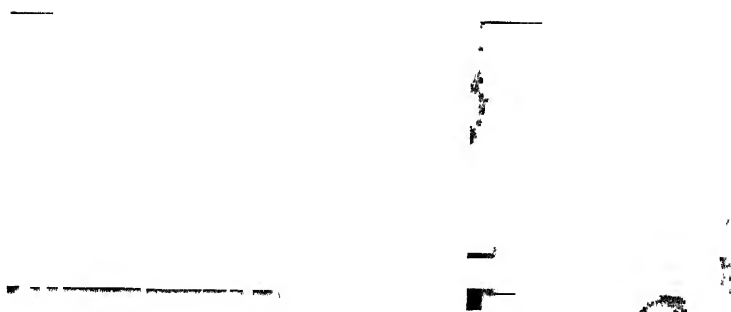
Figure 4.11 Numerical shadowgraph at two Rayleigh numbers

can be seen in the two approaches in terms of intensity distribution with almost
uniform intensity variation at the lower value of Rayleigh numbers and a random
distribution of intensity as the Rayleigh number is raised

4.2   Growth of Optical Crystal from its Aqueous Solution

Crystal growth experiments have been performed at two ramp rates The degree
of supersaturation was kept constant The salt material was potassium dihy-
drogen phosphate (KDP). The experiments were done on a three dimensional
axysymmetric cylindrical growth chamber to study the transients and steady
state behavior of the convection currents for small and big crystals This section
discusses the transient evolution of the convection currents, and the relation of
the schlieren and shadowgraph techniques in context of the qualitative and quan-
titative interpretation. Quantitative analysis have been performed for smaller

crystals having steady state convection and those with smaller unsteady convection plumes The results have been obtained in terms of concentration profiles Qualitative interpretation have been carried out for the experiments with bigger crystals, using schlieren and shadowgraph as the imaging techniques
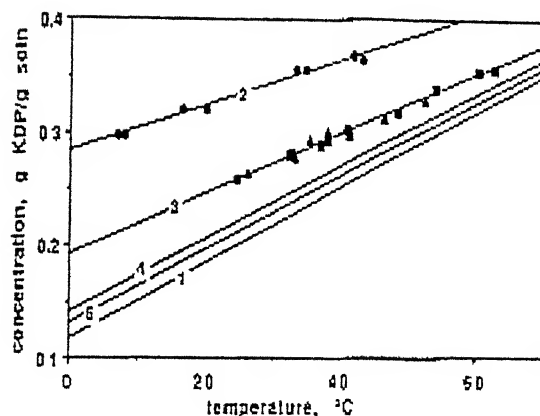

Figure 4 12 Solubility curve of supersaturated KDP solutions, Ref Zaitseva et al (1995)

Figure 4 12 shows the solubility curve of KDP salt The amount of salt that is to be dissolved is determined from this solubility curve and the temperature A supersaturated solution was prepared at 40°C The solution temperature was increased to 60°C and maintained at that temperature for 3-4 hours to dissolve any suspended solute particles Figure 4 13 shows the schlieren and shadowgraph image of the solution when it is poured to the growth chamber Initially severe

Schlieren   Shadowgraph
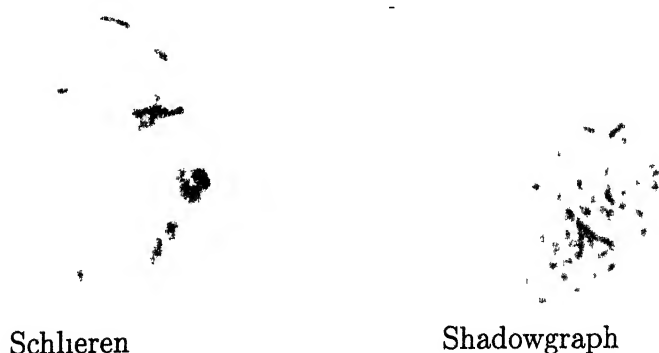
Figure 4.13 Convection currents of solution without seed

convection plumes are seen The convection plumes are due to the presence of thermal gradients in the solution The thermal gradients gradually dies out by

circulation of large volume of constant temperature (as the ramp rate is very low, the solution temperature can be considered constant instantaneously) water in the outer chamber A ramp rate of 5°C/hr is given to bring the solution to the saturation temperature Solution is brought to 35°C and maintained at this temperature for an hour till the temperature gradients dies out Figure 4 14 shows the schlieren image of the solution at the initial stage after the thermal gradients dies out The seed is now dipped into the solution Figure 4 15 shows the initial

Figure 4 14 Schlieren image after the thermal gradients dies out

schlieren and shadowgraph images when the seed in dipped into the solution It is

Schlieren   Shadowgraph
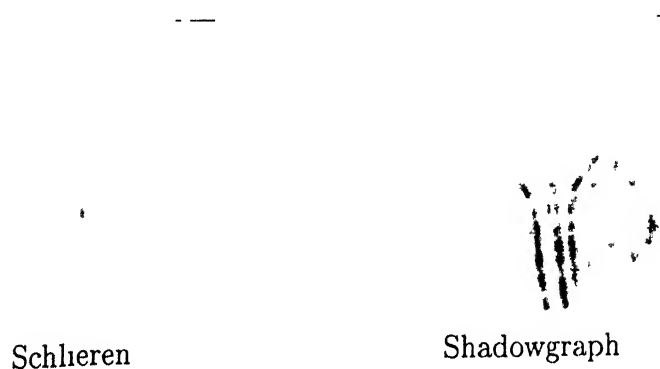
Figure 4 15 Convection currents when seed is dipped into the solution

seen that the seed starts dissolving It happens due to higher affinity of the seed to get dissolved, then the affinity of the solutes towards the seed This process is partly beneficial as it takes away any impurities present in the surface of the seed After sometime the affinity of the solutes towards the seed dominates, and concentration driven buoyancy currents evolves These convection currents are the main source of fresh solutes in the vicinity of the seed

4.2.1 Small Growing Crystal

When the crystal is smaller in size, the associated convection currents are steady in nature. Steady state convection currents can be maintained by giving a very low ramp rate to the solution. The ramp rate in our case was 0.1^OC/hr. Figure 4.16 shows the steady state convection currents of a small growing crystal for three different time period.
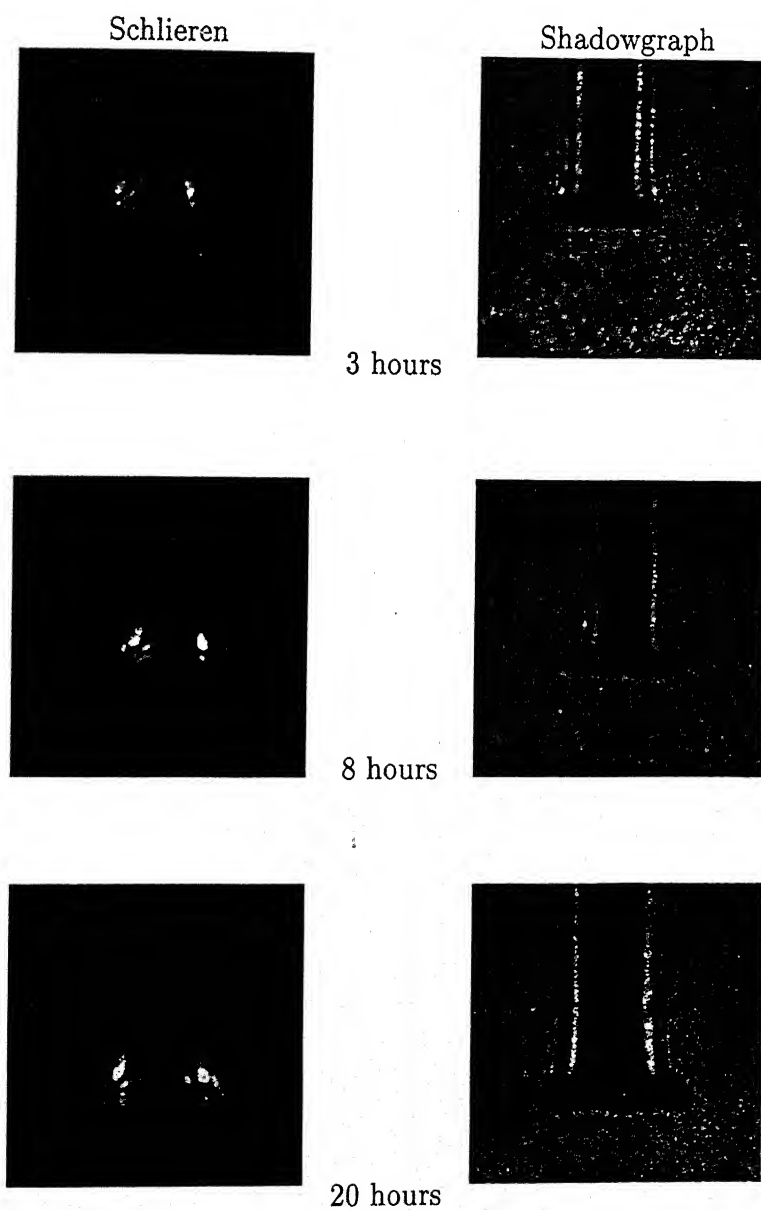

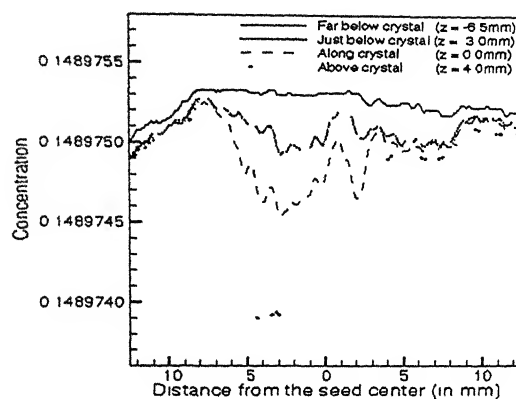
Figure 4.16: Steady state convection of a growing crystal.

Figure 4 17 Concentration profiles after 3 hours of growth
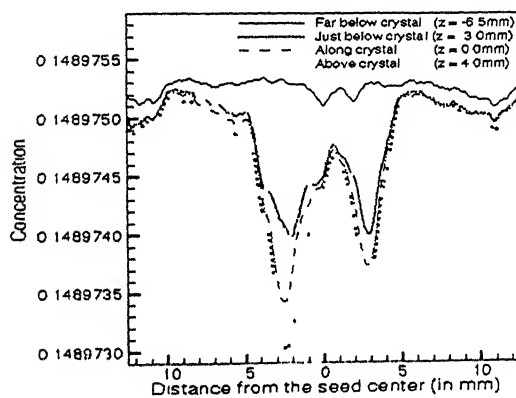
Figure 4 18. Concentration profiles after 8 hours of growth
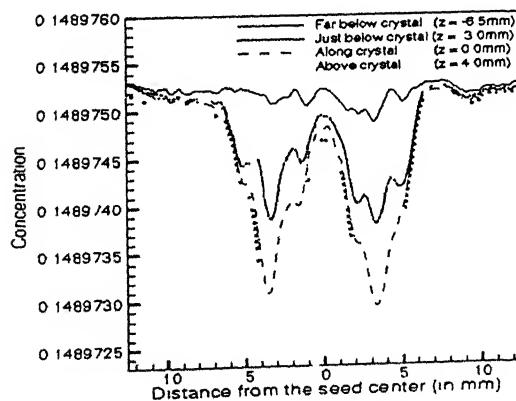
Figure 4.19 Concentration profiles after 20 hours of growth

All of the images shows steady state convection currents There is an increase in the size of the crystal with time indicating the growth of the crystal After a growth of 3 hours, steady state plumes can be seen moving upwards Bright patches in the schlieren image at the surface of the crystal are due to the presence of high concentration gradient at the vicinity of the crystal The area far away from the crystal is uniformly illuminated This shows that there are essentially no gradients present in the solution far away from the crystal Shadowgraph images is a better visualization tool as it directly projects the shadow of the moving plumes.

Figure 4.17 shows the concentration profiles at four different vertical positions in the image To remove any unwanted noice inherent in the steady state image, 4 number of steady state images were averaged for an instant of time It is seen that far below the crystal the solute concentration is uniformly distributed, which is almost equal to the saturated solution Just below the crystal, the concentration is reduced which drives in the solute towards the crystal Along the plane of the crystal, there is an abrupt change in the concentration, which is due to the presence of the concentration boundary layer. Above the crystal buoyancy driven convection plumes are present The concentration of solutes at the plumes are small. So two sharp peaks are seen dropping down indicating the low concentration regions Far away from the crystal, for all the vertical positions the concentration are uniform that is equal to the concentration of the saturated solution

Figure 4.18 and 4.19 shows the concentration profiles after 8 hours and 20 hours respectively. The concentration profiles shows similar variation The concentration values at the plumes reduces with time indicating an increase in the strength of the convection current as the crystal grows in its size

Figure 4.20 shows the experimental results after 30 hours of growth for a higher value of ramp rate Different convection patterns of the two images after the same growth time shows that the convection plumes are unsteady and three dimensional in nature. It affects the quality of the optical crystal.

Figure 4.21 shows the corresponding concentration profiles. The concentra-
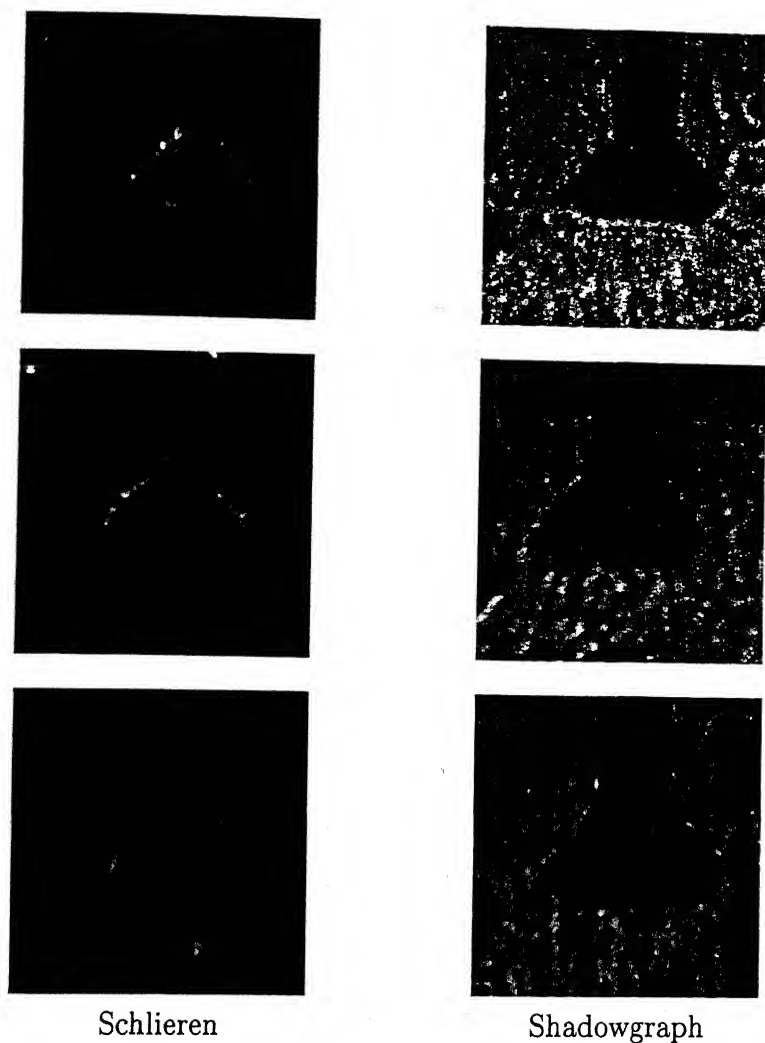
Schlieren   Shadowgraph

Figure 4.20: Crystal after 30 hours of growth.

tions are arbitrarily distributed indicating the unsteadiness of the convective flow field. Nonuniform distribution of the concentration field and the associated turbulence will generate inclusions and make the crystal inhomogeneous. It may also lead to unwanted nucleation of small seeds at the base of the growth chamber. All the seeds will have its own associated convection currents, and the convection in the solution becomes vigorous. The solute deposited at the base goes as a waste and it reduces the quantity of solutes available at the crystal. Ramp rate thus becomes an important parameter for controlling the quality of the optical crystal and the growth of bigger crystal.
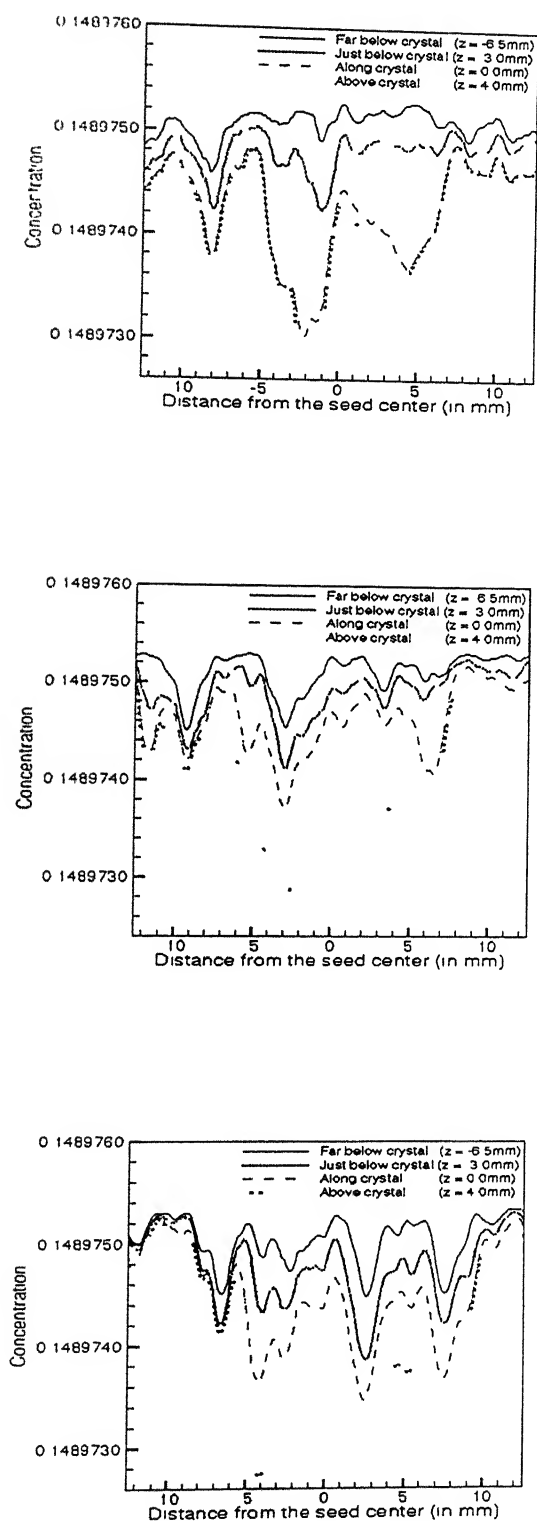
Figure 4.21   Concentration profiles after 30 hours of growth

4.2.2   Large Growing Crystal

As the crystal increases in size, the associated convection currents becomes vigorous. The strength of the convection currents will depend on the degree of supersaturation and the ramp rate. Figure 4.22 shows a large grown crystal.

Figure 4.22: Crystal after 72 hours of growth.

Figure 4.23: Crystal after 120 hours of growth.

The convection currents increases with the increase in size. Thus vigorous convection currents occurs in the vicinity of the crystal. These convection currents can be controlled by a very low ramp rate, so that, very small amount of solutes comes out from the solution.

Figure 4.23 shows a grown crystal after 120 hours of experimental time. After a long period of time the convection currents gradually dies out. The amount of extra solutes present in the solution reduces as it gets deposited into the crystal. Thus the strength of the convection currents is reduced substantially.

Figure 4.24 shows the schlieren images for the complete range of experimental time. Figure 4.25 shows the corresponding shadowgraph images at the same experimental run time. The images shows the beginning of unsteady convection plumes after 48 hours of growth. It was the beginning of unwanted nucleation at the bottom surface.
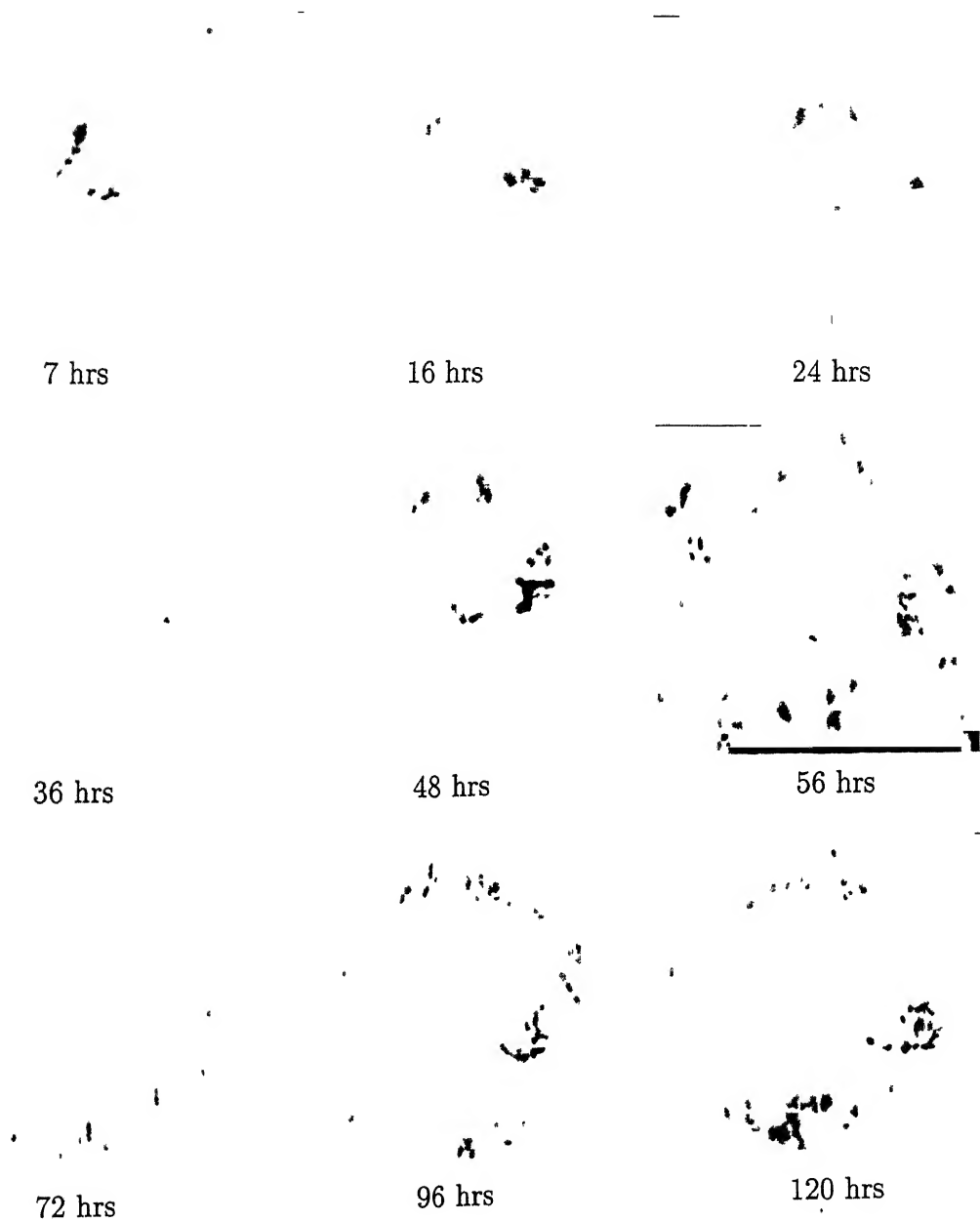
7 hrs

16 hrs

24 hrs

36 hrs

48 hrs

56 hrs

72 hrs

96 hrs

120 hrs

Figure 4 24 Time sequence showing growth of crystal

(Optical technique Schlieren)

7 hrs   16 hrs   24 hrs

36 hrs   48 hrs   56 hrs
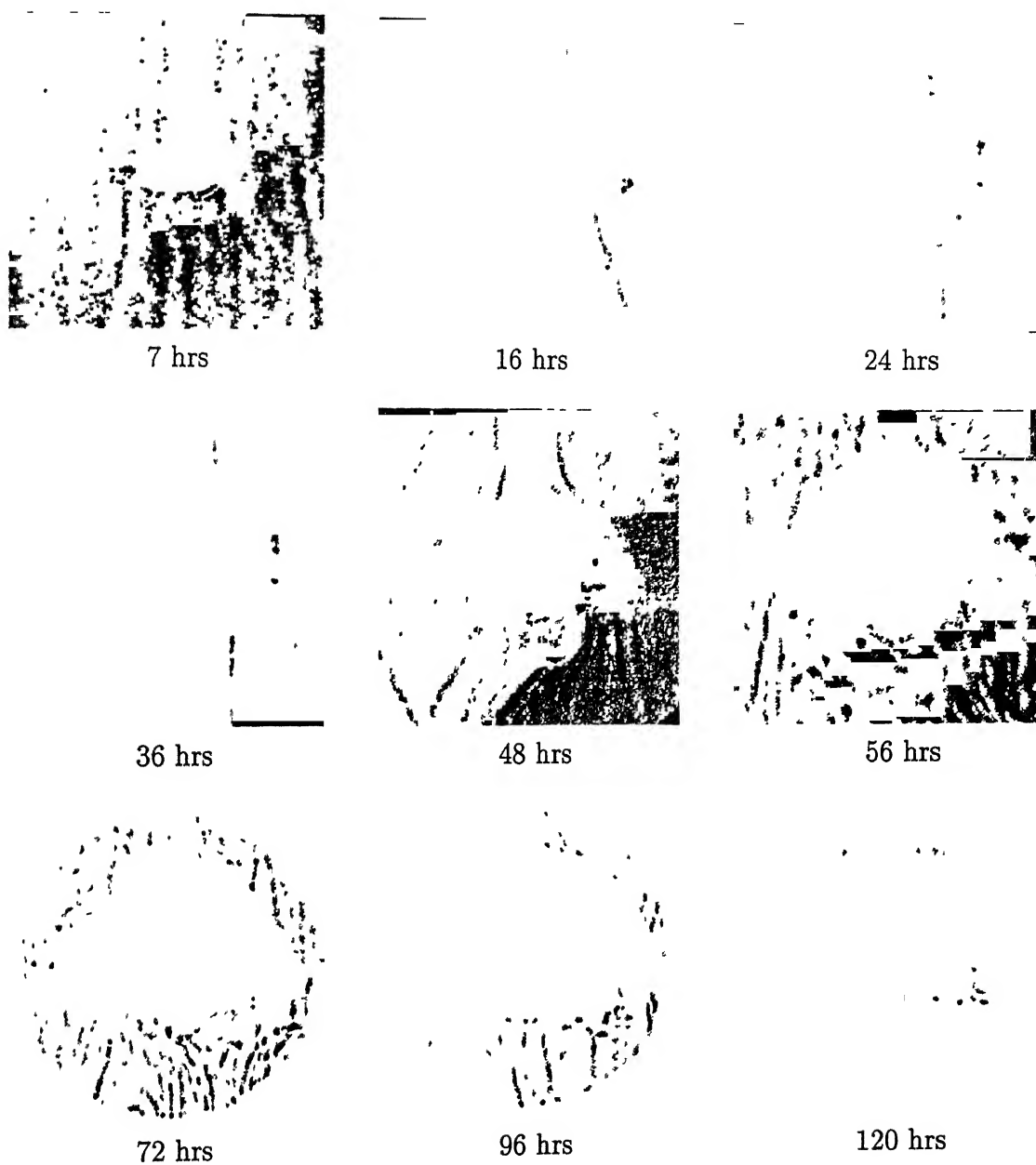
72 hrs   96 hrs   120 hrs

Figure 4 25   Time sequence showing growth of crystal

(Optical technique· Shadowgraph)

The figure 4 26 shows the % growth rate with respect to the time period in both the horizontal and the vertical direction The percentage growth rate is
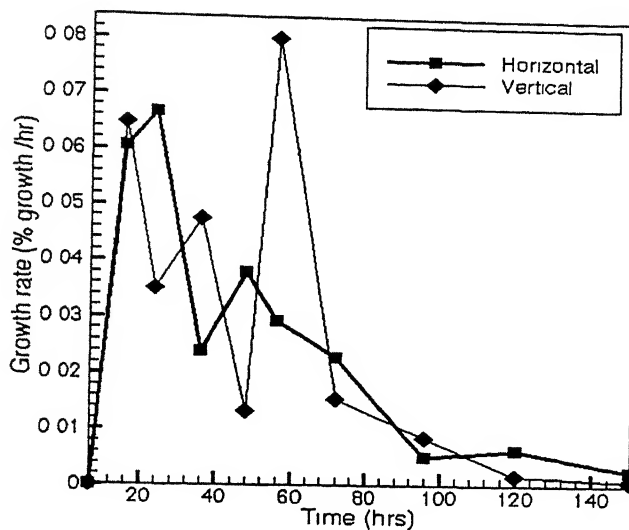
Figure 4.26 Plot of growth rate vs time

calculated by,

$$\frac{\text{size}_{final} - \text{size}_{initial}}{\text{size}_{initial} \times T} \tag{4.1}$$

where $\text{size}_{initial}$ is the crystal size at the preceding time, size_{final} is the crystal size at the present time and T is the time period between the present and the preceding time. The growth rate is similar in both the direction. As the initial size of the crystal is small and large amount of solutes are present in the solution, the growth rate is high at the beginning There is an abrupt increase in the vertical growth rate. This can be attributed to the beginning of unsteady convection plumes. So due to the associated turbulence, a larger amount of solutes is carried to the crystal. At longer period of time the amount of solutes in the solution gets reduced and the convection currents weaken out to give an reduction in the growth rate

Figure 4.27 shows the concentration gradient in the vicinity of the crystal in the lateral and the vertical direction with respect to the experimental time. The variation in the graph is similar to figure 4 26, thereby showing that the growth rate is dependent on the strength of the convection current
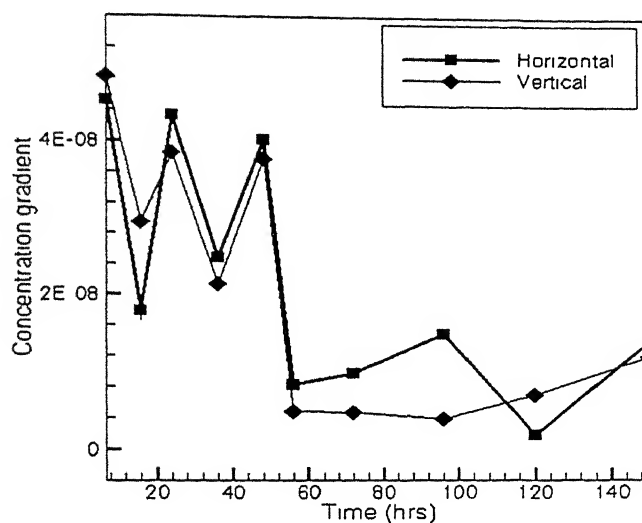
Figure 4 27 Plot of concentration gradient vs time in the vicinity of the crystal

Figure 4.28 shows an grown crystal The quality of the crystal can be visually inspected by its optical transparency

Figure 4.28 Grown Crystals.

4.3 Colour Schlieren

Colour schlieren experiments have been performed to visualize convective fields using an one dimensional cartesian colour filter Sensitivity of the filter have been checked by varying the size of the filter The images have been analysed qualitatively Experiments have been performed to study the convective fields around a burning candle, ice-cubes dissolving in water and Rayleigh Benard convection in an rectangular cavity

4.3.1 Candle Flame

Figure 4 29 shows the monochrome and colour schlieren image of a candle flame The temperature gradient is more dominant in the horizontal direction where

Figure 4 29 Monochrome and colour schlieren image of candle flame

there is an abrupt change in the temperature from the candle flame to the ambient Hence, the filter was positioned, with the variation of colour in the horizontal direction

For the monochrome schlieren image, the high gradient regions is seen as a region of higher intensity due to the bending of light beams towards the region of high refractive index gradient Similarly, the colour schlieren image shows the variation of the refractive index gradient in the field of view as a variation of colours The colour varies strongly in the vicinity of the candle flame due to the presence of high gradients of temperature

4.3.2   Ice Cube Dissolving in Water

Figure 4 30 shows the colour schlieren images of an ice cube dissolving in water
The cold convection plumes, being heavier, moves downwards due to the force

0 0 sec   5 0 sec
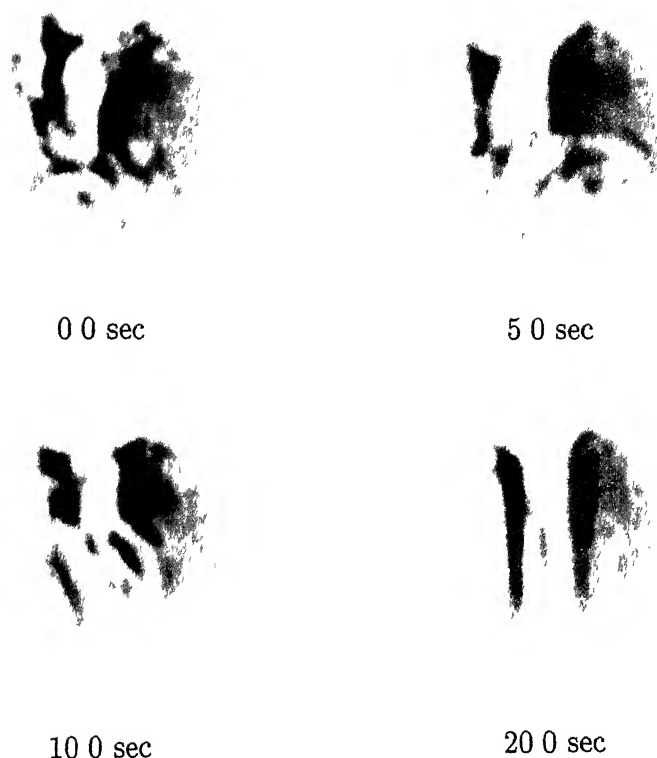
10 0 sec   20 0 sec

Figure 4 30   Colour Schlieren Image of an Ice Cube Dissolving in Water

of buoyancy When the ice cube is suddenly dipped into water, the plumes were
unsteady and turbulent due to the sudden disturbance applied in the field The
plumes gradually stabilizes and the steady plume, with a relatively smaller width,
persisted to remain

The colour schlieren technique can be made more sensitive to the gradients
by varying the size of the colour filter Figure 4 31 shows the colour schlieren
image of an ice cube dissolving in water using a smaller filter. The figure shows
larger range of hue variation Thus colour schlieren provides the flexibility to
capture various range of refractive index gradient, and the size of the colour filter
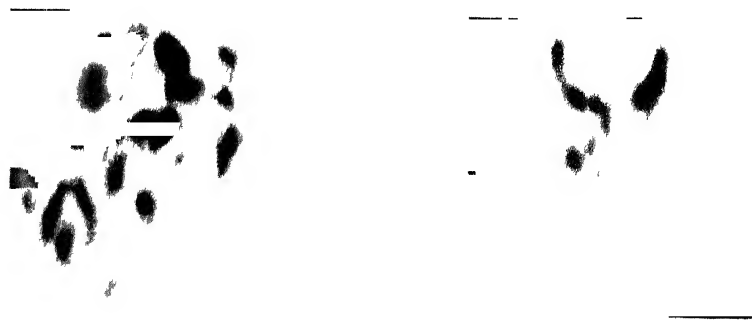can be changed accordingly as per the requirement

Figure 4 31   Colour Schlieren Image using a Smaller Filter

4.3.3   Rayleigh Benard Convection in Rectangular Cavity

Rayleigh Benard convection is the motion of layer of fluid confined between two horizontal walls, heated from below and cooled from above, the side walls of the enclosure being adiabatic   The same rectangular cavity of the monochrome schlieren experiments was used for the colour schlieren experiments   Figure 4 32 shows the monochrome and colour schlieren image of the Rayleigh Benard convection in an rectangular cavity at an four Rayleigh numbers   As the gradient of the temperature is dominant in the vertical direction, so the colour filter was kept vertical   High intensity bands near the upper and the lower wall indicated concentration of high temperature gradients at the top and the bottom walls of the cavity   Thus the light beam passing through this region was deflected in the coloured filter towards the region of lower hue i e   red (or the higher hue depending on the orientation of the filter)   The colour schlieren image shows a definite transformation of the colour bands from yellow,orange to red   The central region which have very low ($\approx$negligible) thermal gradients is in the higher hue region of green   Thus colour schlieren forms a strong tool for qualitative visualization of convective flow fields   Any smaller gradients present at the central zone of the cavity can also be captured as an hue variation by varying the size of the colour filter

Once the colour filter is calibrated, the deflection of the light beam at the filter can be directly related to the change in the hue   This deflection can be related to the gradient of the refractive index, and quantitative analysis can be performed on the colour schlieren images
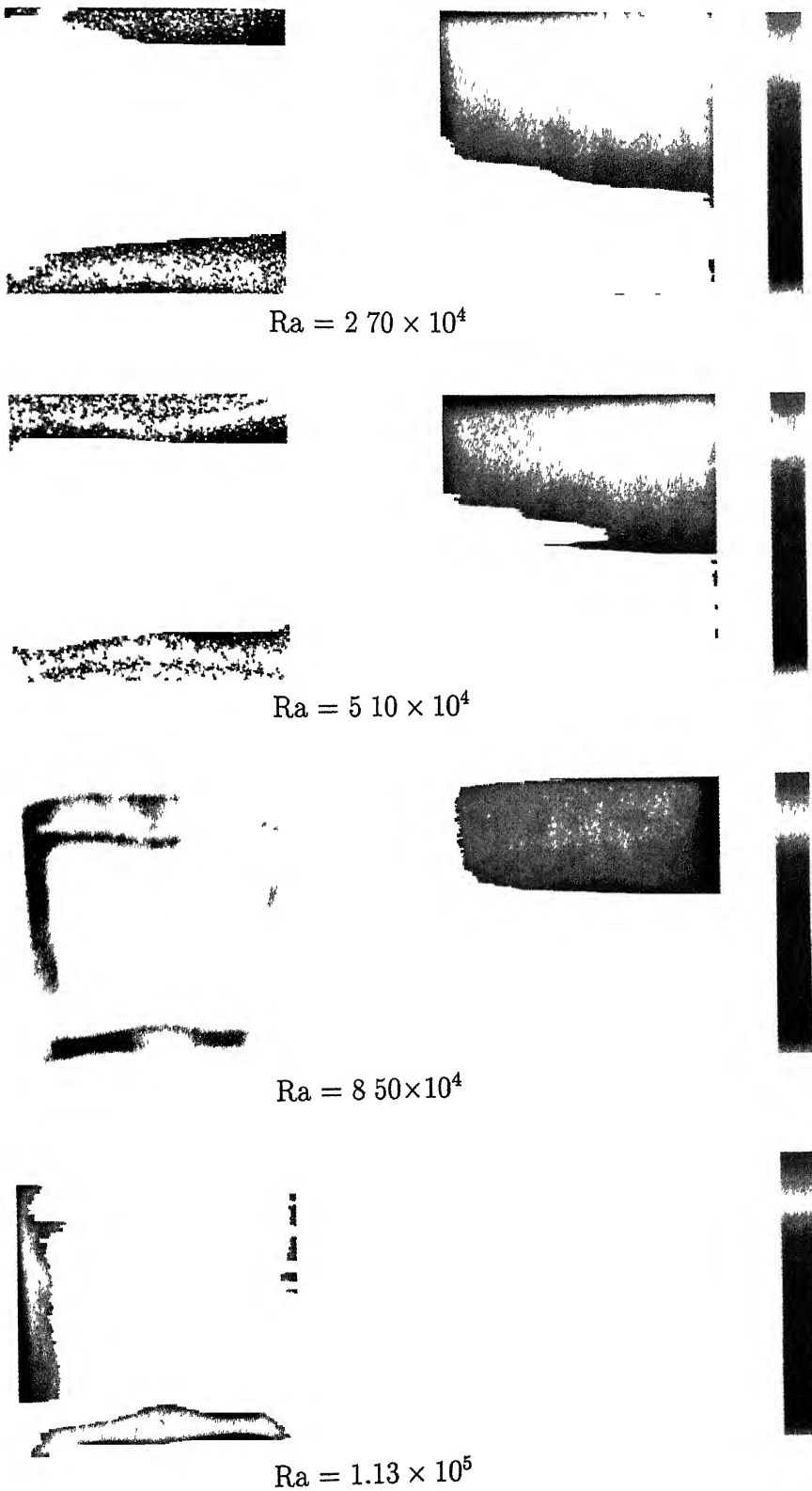
$$Ra = 2\ 70 \times 10^4$$

$$Ra = 5\ 10 \times 10^4$$

$$Ra = 8\ 50 \times 10^4$$

$$Ra = 1.13 \times 10^5$$

Figure 4 32 Monochrome and colour schlieren image of Rayleigh-Benard convection

Chapter 5

Conclusions and Scope for Future Work

5.1   Conclusions

The schlieren technique for both qualitative and quantitative evaluation of temperature and concentration field have been implemented in this work   Both monochrome and colour schlieren technique have been compared   The algorithm for quantitative analysis of schlieren image have been benchmarked with the Mach-Zehnder interferometry, for Rayleigh-Benard convection in an rectangular cavity   A comparison has been carried out against the prediction of a numerical study using a commercial CFD package   Experiments have been done with both air and water   Rayleigh number for air were $1\,40 \times 10^4$, $2\,70 \times 10^4$, $5\,10 \times 10^4$, $8\,50 \times 10^4$, $1\,13 \times 10^5$ and $1\,40 \times 10^5$ Experiments in water have been performed for the Rayleigh numbers of $2\,50 \times 10^6$, $4\,40 \times 10^6$, $2\,50 \times 10^6$, $2\,50 \times 10^6$, $2\,50 \times 10^6$ and $2\,50 \times 10^6$ The benchmarked algorithm have been used to study the convection pattern during growth of optical crystal from its aqueous solution   Some significant conclusion from this work are

1   Benchmarking of the schlieren technique revealed that it can also be used as a tool for quantitative analysis of temperature and concentration field, and not merely as an visualization tool

2 For Rayleigh-Benard experiments with rectangular cavity, steady state patterns were achieved after 3 hours of experimental run time for lower Rayleigh numbers (Ra$\leq$ 8 50 $\times$ 10^4) in air The gradients were seen to be concentrated near the horizontal boundaries of the cavity and a definite increase in the number of fringes was noticed with an increase in Rayleigh number The quantitative results extracted from the interferometry, schlieren and the numerical simulation are in agreement with each other, the maximum deviation between each other being equal to 10% Wall heat transfer rates calculated in terms of Nusselt numbers revealed a good agreement between the experiments and correlation

3 In the higher range of Rayleigh numbers, the flow field was seen to be in a periodic state with a definite frequency of oscillation The experimental images revealed the presence of high thermal gradients near the walls and all the three optical techniques predicted well the dominant features of the flow field Qualitatively, a meaningful agreement was observed between the experimentally recorded schlieren and shadowgraph images with the numerically generated ones

4 At higher value of Rayleigh numbers, presence of roll can be identified as deformation of the shape of fringes in interferometry and intensity patterns in schlieren and shadowgraph images A monotonous decrease in the dimension of roll sizes was observed with increasing Rayleigh numbers

5 Interferometry was found best suited for study of convective flow fields with small gradients Higher gradients in water was qualitatively captured by the shadowgraph techniques The onset of unsteadiness and a further transition to the chaotic flow was clearly observed with an increase in the Rayleigh number The dominant features of the flow field at the two extreme values of Rayleigh numbers (Ra$=$ 2 50 $\times$ 10^6 and 13 50 $\times$ 10^6) were clearly predicted in the experiments and in the numerically generated shadowgraph images

6 In the crystal growth experiments, the quality of the crystal was largely dependent on the strength of the convection currents Increased ramp rate resulted in unwanted nucleation at the bottom surface of the growth chamber The strength of the convection currents can be controlled with the ramp

late

7 Colour schlieren has a superior aesthetic values for qualitative visualization
In addition the resolution for quantitative analysis can be easily controlled
by suitable preparation of filters A reduction in the size of the colour filter
increases the resolution of the colour schlieren technique to capture smaller
gradients

5.2   Scope for Future Work

There are quite a few important issues that can be addressed in the future as far
as visualization and analysis of convective flow field is concerned These are

1 Reconstruct three-dimensional field during the crystal growth process by
   using the tomographic algorithms,

2 study the effects of rotation and pulling of the seed on the associated con-
   vection currents, and the quality of the optical crystal,

3 calibrate the colour filter for quantitative analysis of colour schlieren images,

4 extract the spatial features due to the fluctuation present in the flow field
   by application of multi-resolution wavelet analysis,

5 extract the velocity field and compare with the numerical simulation for
   better understanding of flow physics

References

Bibliography

[1] Goldstein R J , *Fluid Mechanics Measurements*, Hemisphere Publishing Corporation, 1983

[2] Gebhart B , Jaluria Y, Mahajan R L and Sammakia B , *Buoyancy-Induced Flows and Transport*, Hemisphere Publishing Corporation, 1988

[3] Settles G S , *Schlieren and Shadowgraph Techniques*, Springer, 2001

[4] Moubray D E ,The use of schlieren and shadowgraph techniques in the study of flow patterns in density stratified liquids, Journal of Fluid Mechanics, Vol27, Part 3, pp 595-608, 1967

[5] Brackenridge J B and Peterka J , Criteria for Quantitative Schlieren Interferometry, Applied Optics, Vol 6, No 4, pp 731-735, 1967

[6] Davis M R., Measurements in a subsonic turbulent jet using a quantitative schlieren technique, Journal of Fluid Mechanics, Vol 46, pp 631-656, 1971

[7] Davis M R , Quantitative schlieren measurements in supersonic turbulent jet, Journal of Fluid Mechanics, Vol 51, pp 435-447, 1972

[8] Kosugi S., Maeno K., and Honma H , Measurement of Gas temperature Profile in Discharge Region of Excimer Laser with Laser Schlieren Method, Jpn. J Appl Physics, Vol 32, No 3, pp 4980-4986, 1993

[9] Cook S.P. and Chokani N., Quantitative results from focussing schlieren technique, 31st Aerospace Science Meeting, Jan 11-14, Reno, 1993.

[10] Koreeda H., Yanagisawa H., Maeno K , Honna H , Bystrov S A , Ivanov V.I., and Shug aev F V , Front Structures of shock waves in Air, S Waves, pp 263—268, 1995

[11] Tanda G , Experiments on natural convection from two staggered vertical plates, Int J Heat Mass Transfer, Vol 38, No 3, pp 533-543, 1995

[12] Tanda G and Devia F , Application of schlieren technique to heat transfer measurents in free-convection, Experiments in Fluids, Vol 24, pp 285-290, 1998

[13] Kleine S , Enckovort W J P van, and Derix J , A dark field-type Schlieren microscope for quantitative, in situ mapping of solute concentration profiles around growing crystals, Journal of Crystal Growth, Vol 179, pp 240-248, 1997

[14] Bystrov S A , Honna H , Ivanov V I , Koreeda J , Maeno K , Shugaev F V , and Yanagisawa H , Density Reconstruction from Laser Schlieren Signal in Shock Tube Experiments, Shock Waves, Vol 8, pp 183-189, 1998

[15] Fu S , and Wu Y , Quantitative Analysis of Velocity Distribution from Schlieren Images, 8th Intl Symp on Flow Visualization, 1998

[16] Garg S., Cattafesta III L N , Kegerise M A , and Jones G S , Quantitative Schlieren Measurements of Coherent Structures in Planer Turbulent Shear Flows, 8th Intl Symp on Flow Visualization, 1998

[17] Bredikhin V I , Galushkina G L , and Kuznetsov, Schlieren technique to in situ monitor rapidly-growing KDP crystal surface, Journal of Crystal Growth, Vol 219, pp 83-90, 2000

[18] Hikmet R A M , In situ observation of ion concentration profiles in lithium ion-conducting gels, Solid State Ionics, Vol 127, Issues 3-4, pp 199-205, 2000

[19] Chashechkin Y D , and Mitkin V V , Experimental study of fine structure of 2D wakes and mixing past an obstacle in a continuously stratified fluid, Dynamics of Atmospheres and Oceans, Vol 34, Issue 2-4, pp 165-187, 2001

[20] Howes W L., Rainbow Schlieren and its Applications, Applied Optics, Vol. 23, No 14, pp 2449-2460, 1984

[21] Settles G S , Colour-coding Schlieren technique fir the optical study of heat and fluid flow, Int J Heat and Fluid Flow, Vol 6, No 1, pp 3-14, 1985

[22] Greenberg P S , Klimek R B , and Buchele R , Quantitative Rainbow Schlieren Deflectometry, Applied Optics, Vol 34, No 192, pp 3811-3822, 1995.

[23] Al-Ammar K ,Agrawal A K , Gollahalli S R , and Griffin D , Application of rainbow schlieren deflectometry for concentration measurements in an axisymmetric helium jet, Experiments in Fluids, Vol 25, pp 89-95, 1998

[24] Agrawal A K , Butak N K , Gollahalli S R , and Griffin D , Three dimensional rainbow schlieren tomography of a temperature field in gas flows, Applied Optics, Vol 37, No 3, pp 497-485, 1998

[25] Shenoy A.K , Agrawal A K , Gollahalli S R , Quantitative evaluation of flow computations by rainbow schlieren deflectometry, AIAA Journal, Vol 36, No. 11, pp 1953-1960, 1998

[26] Agrawal A K , Albers B.W , and Griffin D W , Abel inversion of deflectometric measurements in dynamic flows, Applied Optics, Vol 38, No 15, pp 3394-3398, 1999

[27] Albers B W and Agrawal A K , Schlieren Analysis of an Oscillating Gas-Jet Diffusion Flame, Combustion and Flame, Vol 119, pp 84-94, 1999

[28] Krishnamurti R , On Transitions to Turbulent Covection, Part 1, The Transitions from two to three dimensional Flow, Journal of Fluid Mechanics, Vol 42, Part 2, pp 295-307, 1970a

[29] Krishnamurti R , On the Transitions to Turbulent Convection, Part 2, The Transitions to Time-Dependent flow, Journal of Fluid Mechanics, Vol. 42, Part 2, pp 309-320, 1970b

[30] Gollub J P and Benson S.V , Many Routes to Turbulent Convection, Journal of Fluid Mechanics, Vol 100, Part 3, pp 449-470, 1980

[31] Michael Y C and Yang K T, Three-dimensional Mach-Zehnder Interferometric Tomography of the Rayleigh-Benard Problem, ASME Journal of Heat Transfer, Vol 114, pp 622-629, 1992

[32] Busse F H., Transition to Turbulence in Rayleigh-Benard Convection in Topics in Applied Physics, Hydrodynamic Instabilities and Transition to Turbulence, Edited by Swinney H L and Gollub J P, Springer-Verlag, Berlin, 1985. Rolls in a

[33] Mishra D, Muralidhar K, and Munshi P, Performance Evaluation of Fringe Thinning Algorithms for Interferometric Tomography, Optics and Lasers in Engineering, Vol 30, pp 229-249, 1998

[34] Mishra D, Muralidhar K, and Munshi P, Interferometric Study of Rayleigh-Benard Convection using Tomography with Limited Projection Data, Experimental Heat Transfer, Vol 12(2), pp 117-136, 1999

[35] D Mishra, K Muralidhar and P Munshi, Isotherms in a Horizontal Differentially Heated Cavity at Intermediate Rayleigh Numbers, International Communications in Heat and Mass Transfer, Vol 26(5), pp 729-738 1999

[36] Mishra D., Muralidhar K, and Munshi P, A Robust MART Algorithm for Tomographic Applications, Numerical Heat Transfer B (Fundamentals) Vol 35 (4), pp 485-506 1999

[37] Mishra D, Muralidhar K, and Munshi P, Interferometric Study of Rayleigh-Benard Convection at Intermediate Rayleigh Numbers, Fluid Dynamics Research, Vol 25(5), pp 231-255, 1999

[38] Mishra D., Muralidhar K, Munshi P, Laser Interferometry for Measurement of Three Dimensional Temperature Fields in Fluids using Tomography, Defence Science Journal, Vol 49, pp 243-355, 1999

[39] Mukutmoni D and Yang K T, Flow Transitions and Pattern Selection of the Rayleigh-Benard Problem in Rectangular Enclosures, Sadhna, Vol 19, Part 5, pp 649-670, 1994

[40] Mukutmoni D and Yang K T, Thermal Convection in Small Enclosures: An Atypical Bifurcation Sequences, Int Journal of Heat and Mass Transfer, Vol 38, Part 1, pp113-126, 1995a

[41] Mukutmoni D and Yang K T, Pattern Selection for Rayleigh-Benard Convection in Intermediate-aspect-ratio Boxes, Numerical Heat Transfer, Part A, Vol 27, pp 621-637, 1995b

[42] Wilcox W R, Chen P S, and Shlichta, Free Convection about a rectangular prismatic crystal growing from a solution, Int J Heat Mass Transfer, Vol 22, pp 1669-1679, 1979

[43] Wilcox W R, Influence of convection on the growth of crystals from solution, Journal of Crystal Growth, Vol 65, pp 133-142, 1983

[44] Shlichta P.J, Feasibility of mapping solution properties during the growth of protien crystals, Journal of Crystal Growth, Vol 76, pp 656-662, 1986

[45] Onuma K, Tsukamoto T, and Sunagawa I, Role of buoyancy driven convection in aqueous solution growth, a case study of $Ba(NO_3)_2$ crystal, Journal of Crystal Growth, Vol 89, pp 177-188, 1988

[46] Onuma K, Tsukamoto K, Sunagawa I, Measurements of surface supersaturations around a growing K-alum crystal in aqueous solution, Journal of Crystal Growth, Vol 98, pp 377-383, 1989

[47] Onuma K., Tsukamoto K, and Sunagawa I, Effect of buoyancy driven convection upon the surface microtopographs of $Ba(NO_3)_2$ and CdI_2 crystals, Jpurnal of Crystal Growth, Vol 98, pp 384-390, 1989

[48] Mantani M, Sugiyama M, and Ogawa T., Electronic measurement of concentration gradient around a crystal growing from a solution by using Mach-Zehnder interferometer, Journal of Crystal Growth, Vol 114, pp 71-76, 1991

[49] Onuma K, Tsukamoto K, and Nakadate S, Application of real time phase shift interferometer to the measurement of concentration field, Journal of Crystal Growth, Vol 129, pp 706-718, 1993

[50] Sunagawa I., Tsukamoto K, Maiwa K, and Onuma K, Growth and perfection of crystals from aqueous solution Case studies on Barium Nitrate and K-Alum, Prog Crystal Growth and Characterization, Vol 30, pp 153-190, 1995

[51] Zaitseva N P, Ranhkovich L N, and Bogatyreva S V, Stability of KH_2PO_4 and $K(H,O)_2PO_4$ solution at fast crystal growth rates, Journal of Crystal Growth, Vol 148, pp 276-282, 1995

[52] Rudolph P, Elements of Thermodynamics for the Understanding and Design of Crystal Growth Process, Materials Science Forum, Vols 276-277, pp 1-26, 1998

[53] Piano E, Dall'Aglio G A, Crivello S, Chittofrati R, and Puppo F, New optical techniques for crystal growth from fluids, Materials Chemistry and Physics, Vol. 66, pp 266-269, 2000

[54] Booth N A, Chernov A.A, Vekilov P G, Characteristic length scales of step bunching in KDP crystal growth in situ differential phase-shifting interferometry study, Journal of Crystal Growth, Vols 237-239, pp 1818-1824, 2002

Appendix

Appendix A

Numerical Simulation of Rayleigh-Benard Convection Problem in Rectangular Cavity

The present appendix is concerned with the numerical solution of the buoyancy-driven flow in an Rectangular cavity Simulations were done using an commercial CFD package, FLUENT 5.5 FLUENT is a state-of-the-art computer program for modeling fluid flow and heat transfer in complex geometries All functions required to compute a solution and display the results are accessible through an interactive, menu-driven interface

GAMBIT is the preprocessor for geometry modeling and mesh generation Once the grid has been read into FLUENT, all the remaining operations are performed within the solver These include setting boundary conditions, defining fluid properties, executing the solution, refining the grid, and viewing and postprocessing the results

The dimensions of the test cell are the same as considered in the experimental work Fluid considered was both air and water Simulations for air was done for Rayleigh numbers = $1 40X10^4$, $2 70X10^4$, $5 10X10^4$, $8 50X10^4$, $1 13X10^5$ and $1 40X10^5$ corresponding to the temperature difference of $\Delta T = 5, 10, 20, 30, 40, 50K$ Simulations in water was done for two Rayleigh numbers A lower value of $2 50X10^6$ and a higher value of $13.50X10^6$ was selected corresponding to the temperature difference of ΔT=3K and 10K

A.1   Governing Equations

The natural convection in any configuration is governed by the laws of conservation of mass, momentum and energy These are mathematically represented by the continuity equation, Navier-Stokes equation and the energy equation In FLUENT which in general form are as follows

Continuity

$$\frac{\partial \rho}{\partial t} + \frac{\partial}{\partial x_i}(\rho u_i) = S_m \tag{A 1}$$

It is the general from of the mass conservation equation and is valid for both incompressible as well as compressible flows. The source S_m is the mass added to the continuous phase from the dispersed second phase from any user-defined sources.

Momentum

$$\frac{\partial}{\partial t}\rho u_i + \frac{\partial}{\partial t}\rho u_i u_j = \frac{\partial p}{\partial x_i} + \frac{\partial \tau_{ij}}{\partial x_j} + \rho g_i + F_i \tag{A 2}$$

It is the conservation of momentum in the i direction in an inertial (non-accelerating) reference frame, where, p is the static pressure, τ_{ij} is the stress tensor, and ρg_i and F_i are the gravitational body force and external body force in the i direction respectively

Energy

FLUENT solves the energy equation in the following from

$$\frac{\partial}{\partial t}(\rho E) + \frac{\partial}{\partial x_i}(u_i(\rho E + p))$$

$$= \frac{\partial}{\partial x_i}\left(k_{eff}\frac{\partial T}{\partial x_i} - \sum_{j'} h_{j'}J_{j'} + u_j(\tau_{ij})_{eff}\right) + S_h \tag{A 3}$$

where k_{eff} is the effective conductivity and $J_{j'}$ is the diffusion flux of species j' The first three terms in the right-hand side represent energy transfer due to conduction, species diffusion, and viscous dissipation, respectively S_h includes heat of chemical reaction, and any other volumetric heat sources defined

For solving natural convection problem, the Boussinesq model is applied By Boussinesq approximation, $\rho = \rho_0(1 - \beta \Delta T)$ The Boussinesq model

treats density as a constant value in all solved equations, except for the buoyancy term in the momentum equation

$$(\rho - \rho_0)g \cong -\rho_0\beta(T - T_0)g \qquad (A\ 4)$$

where ρ_0 is the (constant) density of the flow, T_0 is the operating temperature, and β is the thermal expansion coefficient

A.2 Geometrical Modeling and Grid Formation

GAMBIT is the preprocessor for geometry modeling and mesh generation A rectangular three-dimensional geometry is generated with the dimensions similar to the experimental cavity The geometry is meshed uniformly The grid size selected was $25 \times 25 \times 354$ The grid size was limited by the memory consideration and the computational time.

All the boundaries are specified as wall As the simulations are to be done for the fluid inside the cavity, the continum type for the generated volume was defined as fluid The three-dimensional mesh was then exported to a mesh file This mesh file can be exported to FLUENT for simulations

A.3 Solver

An **segregated** solver was used to solve the equations Using this approach, the governing equations are solved sequentially (i e , segregated from one another) Because the governing equations are non-linear (and coupled), several iterations of the solution loop must be performed before a converged solution is obtained The formulation was **implicit** Thus for a given variable, the unknown values in each cell is computed using a relation that includes both existing and unknown values from neighboring cells It was selected due to its better convergence The space was **three-dimensional.** Both steady and unsteady calculations have been performed The pressure equations were body force weighted while the momentum and the energy

equation were discretized using the second order upwind scheme   SIM-PLE algorithm has been used for pressure-velocity coupling   The under-relaxation factor can be varied depending on the convergence requirement

For the simulations in air, the flow field has been considered in the laminar regime from our experimental experience   Simulations with higher Rayleigh number in water was considered to be in the turbulent region   The turbulence equations were solved by the two-equation **k-epsilon model**

The size of the flow structures form the basis of the convergence criterion Thus when the residual of the velocity components reduces below the size of the mesh, the simulations were stopped

A.4   Material Properties

The simulations were performed for both air and water   The following material properties were selected for both the fluids

A.4.1   Air

Density = 1.225 ($\frac{kg}{m^3}$), the fluid was Boussinesq approximated
C_p = 1006 43 ($\frac{J}{kg-K}$), constant
Thermal conductivity = 0 0242 ($\frac{W}{m-K}$), constant
Viscosity = 1.7894e^{-5} ($\frac{kg}{m-s}$), constant
Thermal expansion coefficient = 0 00333 (K^{-1}), constant

A.4.2   Water

Density = 998.2 ($\frac{kg}{m^3}$), the fluid was Boussinesq approximated
C_p = 4182 ($\frac{J}{kg-K}$), constant
Thermal conductivity = 0 6 ($\frac{W}{m-K}$), constant
Viscosity = 0 001003 ($\frac{kg}{m-s}$), constant
Thermal expansion coefficient = 0 00333 (K^{-1}), constant

A.5 Operating, Boundary and Initial Conditions

A.5.1 Operating Conditions

The following operating conditions have been used

Operating pressure = The operating pressure was taken to be atmospheric

Operating Temperature = It was the ambient temperature in which the experiments were performed.

Gravity = The gravity force was enabled which was taken to be 9 81 m/s^2 in the downward direction

A.5.2 Boundary Conditions

The boundary conditions identical to those of in the experiments have been employed. The upper and the lower surfaces were taken to be prescribed temperatures, while all the other boundaries were thermally insulated Mathematically,

Upper and Lower wall:

$$T_{wall} = \text{constant} \tag{A 5}$$

Other walls:

$$\frac{\partial T_{wall}}{\partial n} = 0 \tag{A 6}$$

where n is the direction perpendicular to the wall

A.5.3 Initial Conditions

The following initial conditions have been applied

Temperature:
$$T_{initial} = \frac{T_{upperwall} + T_{lowerwall}}{2} \tag{A 7}$$

Velocity:
$$Velocity_{initial} = 0 \tag{A 8}$$

A.6 Data Reduction

The numerical solution of the cavity flow yields the field of the temperature Experimental results gives us the depth averaged temperature values in the direction of propagation of light beam So, the numerically simulated temperature field has been averaged over 30 number of planes concentrated at the core region

FLUENT stores the data in its own format The temperature information at all the planes were extracted by the XY plots The FLUENT format of the XY data file is converted into a user friendly data file The temperature values were stored in a matrix The temperatures of all the planes can now be averaged The averaged temperature field was used to compare the numerical simulations with the experiment in terms of temperature contours and temperature profiles

By numerical integrating the thermal field along the longer dimension of the cavity, equivalent schlieren and shadowgraph images could be generated The thermal field required for constructing the schlieren pattern is the first derivative of the temperature For a shadowgraph, the starting point is the Laplacian of the temperature field Finite difference schemes were used to derive the first and the second derivative The resulting data is scaled over the range of 0-255 An image processing software, GIMP, is used to derive monochrome images from this data with a gray scale variation in the intensity This numerical images can be used for qualitative comparison of the experimental and the numerical data

A.7 Results

Results have been discussed in terms of the temperature contours, temperature profiles, velocity contours and velocity vectors Simulations for lower value of temperature differences in air and water is being solved by steady state simulations. Unsteady simulations were done for higher value of Rayleigh number in air

A.7.1   Simulations for Air

Simulations in air have been done for six values of Rayleigh numbers i e , Ra = 1 40×10⁴, 2.70×10⁴, 5 10×10⁴, 8 50×10⁴, 1 13×10⁵ and 1 40×10⁵ which correspond to the temperature difference of $\Delta T = 5, 10, 20, 30, 40$ and $50K$ respectively   Steady state simulations were done for temperatures $\leq 30K$ Figure A 1 shows the temperature contours for the whole range of Rayleigh numbers   It shows an gradual conversion of unicellular flow pattern to the bicellular flow   The Unsteadiness of the flow is visible at Higher value of Rayleigh numbers
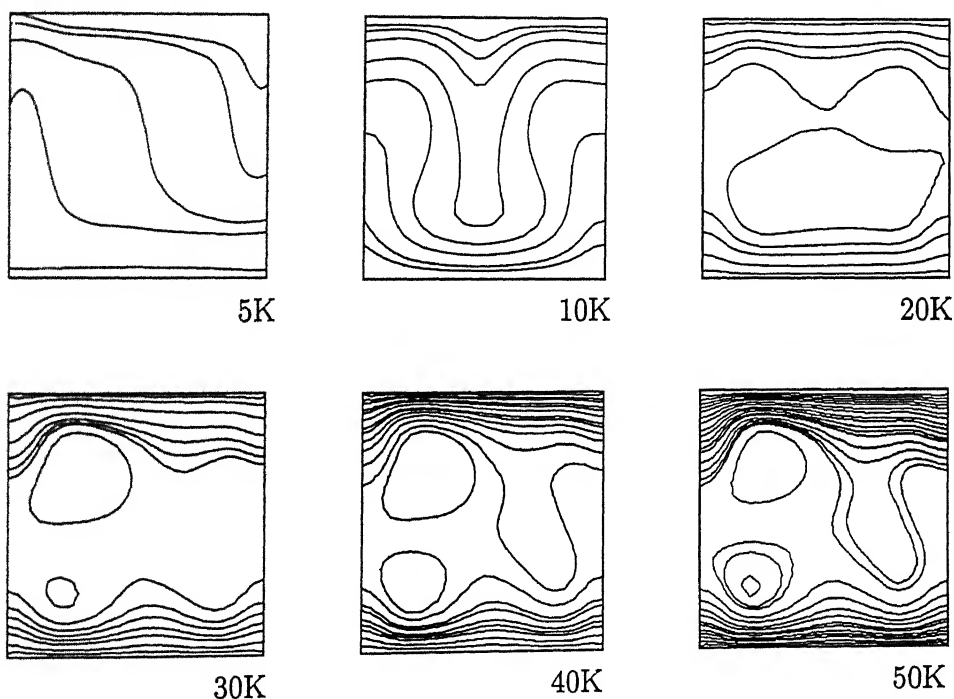
Figure A 1 Depth averaged temperature contours for air

Figure A 2 shows the numerically generated schlieren images for the complete range of Rayleigh numbers. At the Rayleigh number of 1 40 × 10⁴ the intensity is uniformly distributed over the height due to the presence of uniform gradients throughout the cavity height But for higher value of Rayleigh numbers, the high gradients are concentrated at the boundaries, which is reflected by high intensity bands near the upper and the lower wall of the cavity The band width reduces with increasing Rayleigh number, as, the gradients are more concentrated towards the wall.
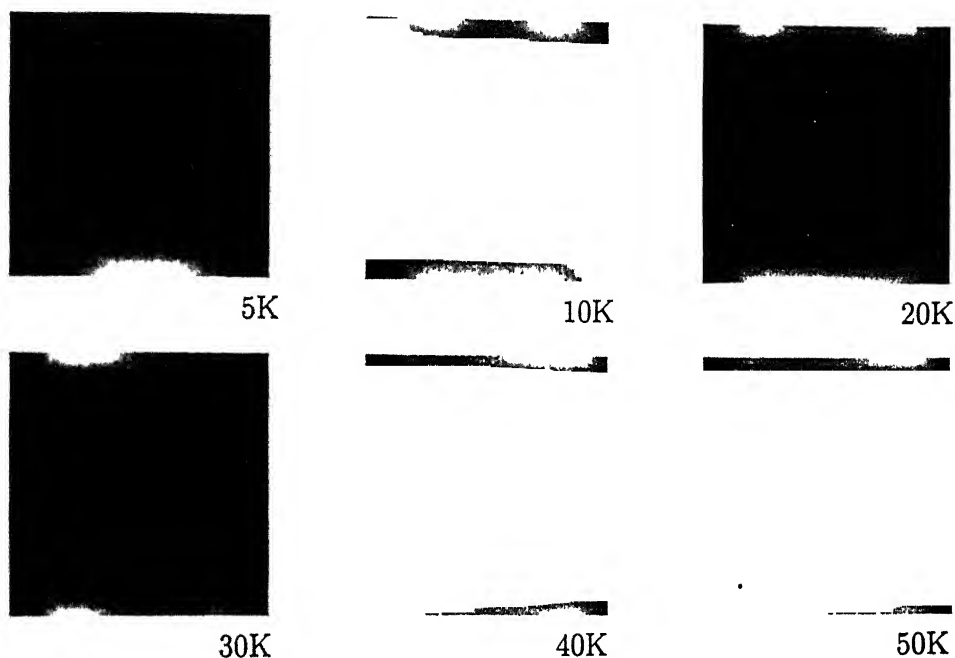
Figure A 2   Numerical Schlieren image for air
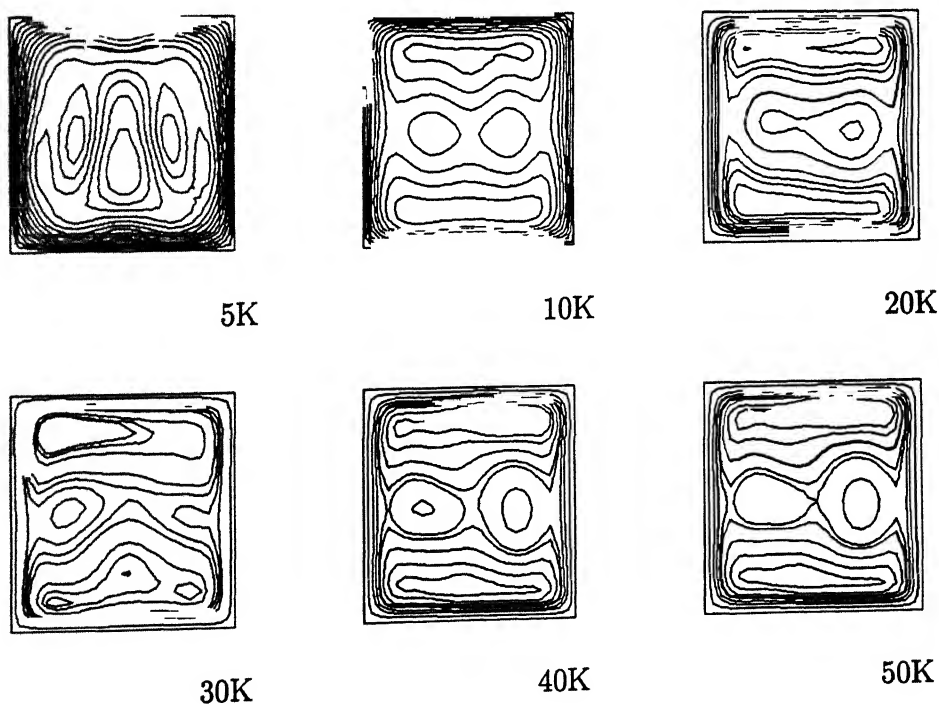
Figure A 3   Depth averaged velocity contours for air

Figure A.3 shows the depth averaged velocity contours for the entire range
of temperature differences. The flow is seen to be symmetric till the $\Delta T \leq$

| 5K | 10K | 20K |

| 30K | 40K | 50K |
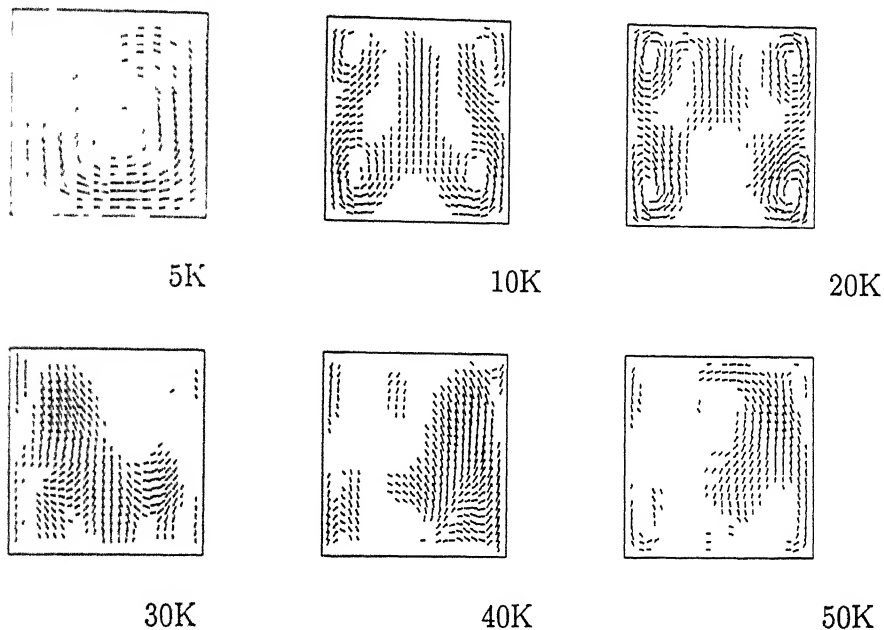
Figure A 4 Depth averaged velocity vectors for air

20K. The symetricity breaks down at higher Rayleigh numbers due to unsteadiness in the flow field   The velocity vectors shown in figure A 4 reflects the flow direction   The flow is essentially unicellular at Ra=1 40 × 10^4. But it gradually changes to bicellular and then to unsteady flow with increasing Rayleigh number

Unsteady simulations were done for higher Rayleigh numbers of 1 13 × 10^5 and 1 40 × 10^5 respectively Figure A 5 and A 6 shows the transient behavior of the flow field in terms of the depth averaged temperature contours Similar unsteadiness was also observed in the experiments conduced for similar Rayleigh numbers. The simulations were performed for 10 seconds of real time   The frequency of oscillation was determined by plotting the temperature variation with time for a region of the flow field   Figure A 7 and A.8 shows the plot of variation of temperature with respect to time for both the temperature difference   The values are quoted in table 4 3 and compared with the experimental values.

Figure A 9, A 10 and A 11 shows the temperature contours, velocity contours and velocity vectors for the longitudinal section of the cavity.
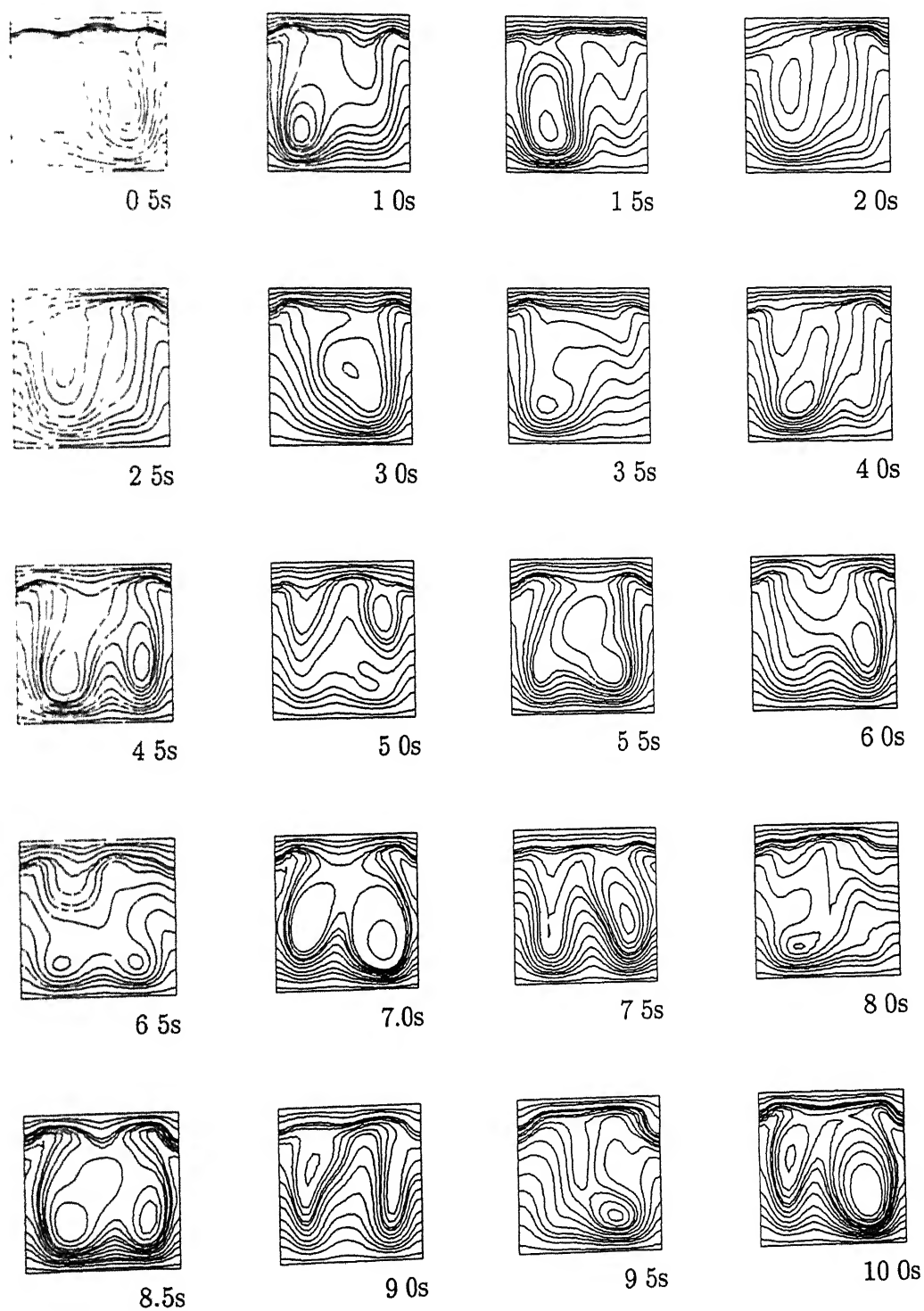
Figure A.5· Unsteady temperature contours for air at 40K (Δt for simulation = 0.1 sec)
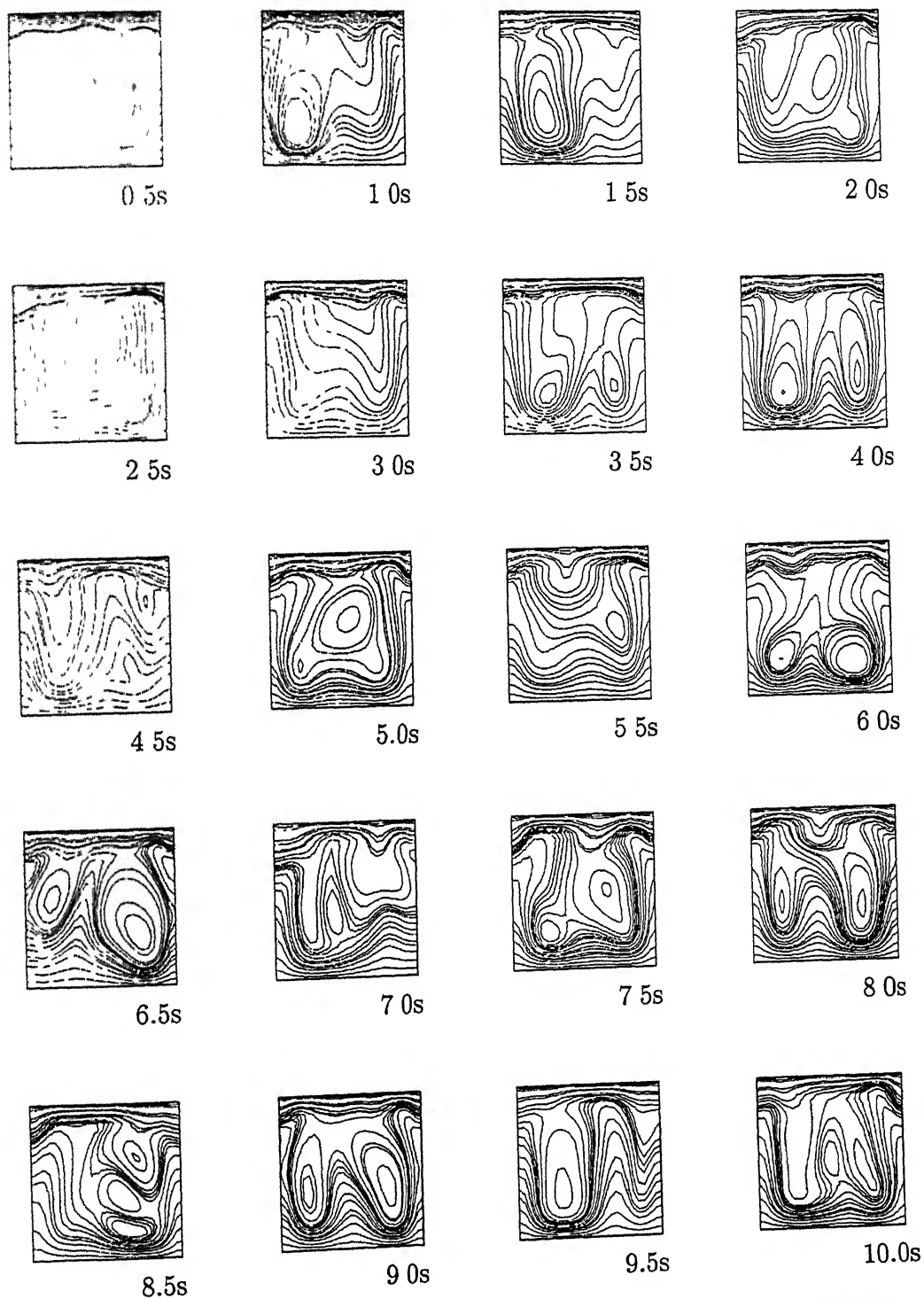
Figure A 6 Unsteady temperature contours for air at 50K (Δt for simulation = 0 1 sec)
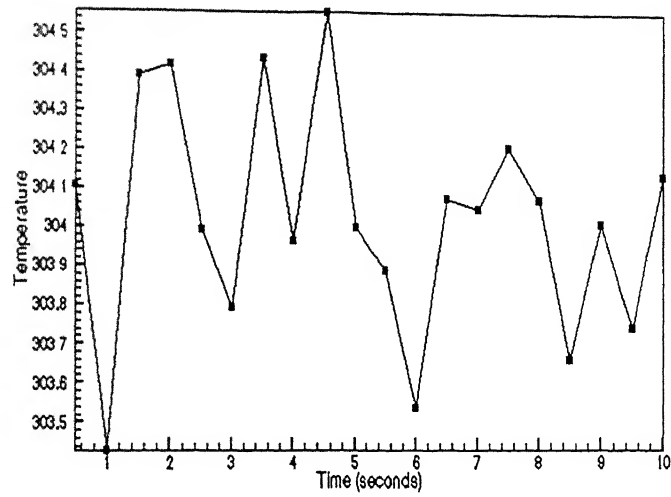
Figure A.7   Unsteady temperature fluctuation for air at 40K
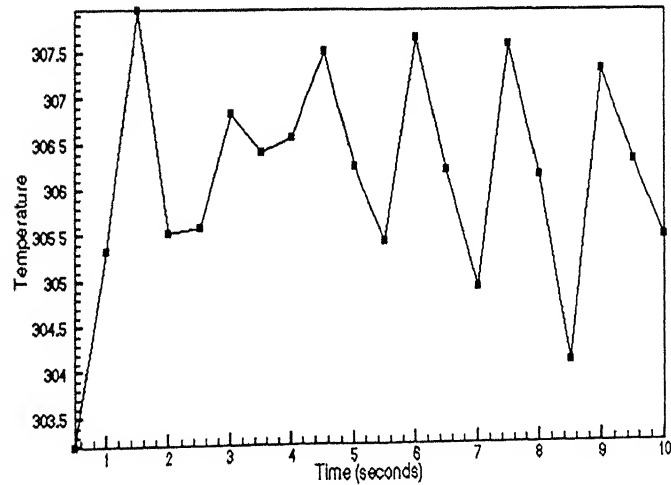
Figure A 8   Unsteady temperature fluctuation for air at 50K

5K

10K

20K
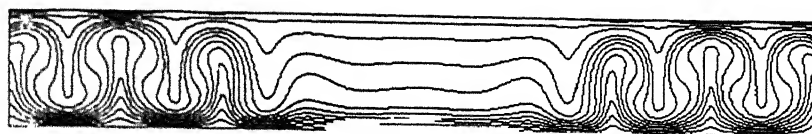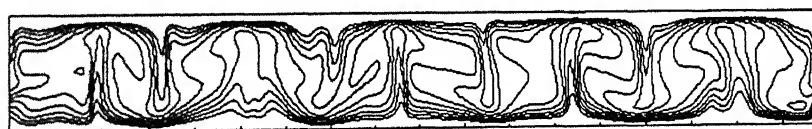
30K

40K

50K

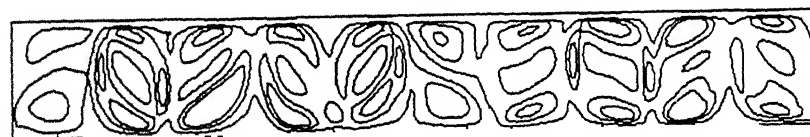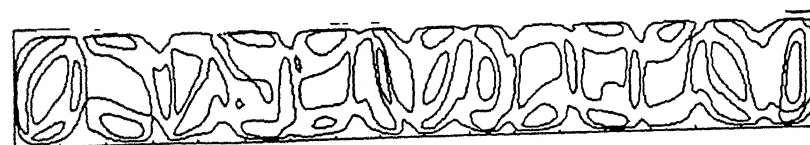Figure A 9   Temperature contours along the longitudinal plane for air
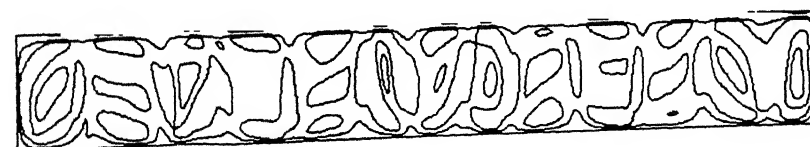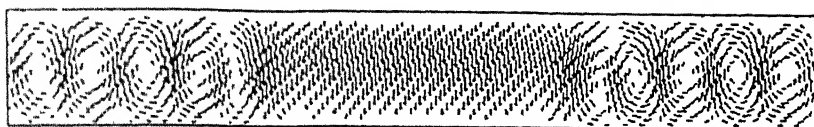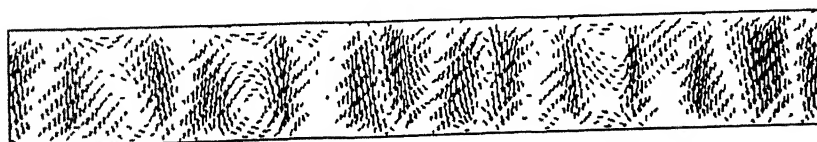
5K

10K

20K
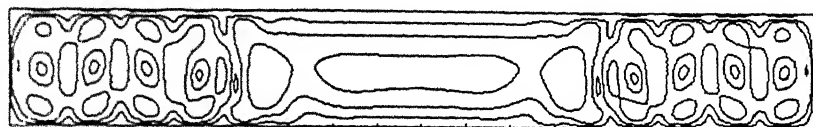
30K

40K

50K

Figure A 10 Velocity contours along the longitudinal plane for air

5K

10K

20K

30K

40K

50K

Figure A 11   Velocity vectors along the longitudinal plane for air

At Ra=1 4 × 10⁴ the flow is symmetric and the rolls are concentrated near the optical windows The flow seems to be not developed completely At Ra=2 7 × 10⁴ and 5 1 × 10⁴ the flow is symmetric in nature The number of rolls is almost similar to the aspect ratio of the cavity which is at per with the theory The flow starts to become unsteady at Ra=8 5 × 10⁵ But the flow patterns are still symmetric At higher value of Ra i e at Ra=1 13 × 10⁵ and 1 40 × 10⁵ the flow shows a complete unsteady behavior

The rolls and the flow patterns can also be seen from the plot of the velocity contours and the velocity vectors in figures A.10 and A 11

A.7.2   Simulations for Water

Simulations for water was done for two values of Rayleigh numbers A lower value of 2 50 × 10⁶ and a higher value of 13 50 × 10⁶ was selected Due to the higher values of Rayleigh numbers, the flow is essentially turbulent So turbulence models was used for simulating the flow field. Figure A 12 shows the velocity contours and the numerical shadowgraph image for the lower Rayleigh number. The flow is less turbulent A thin bright band in the lower wall can be due to the presence of the boundary layer The top portion near the wall is having the darkest intensity and the middle is intermediately intensified

Figure A.13 shows the velocity contours and numerical shadowgraph image for the higher Rayleigh number of 13 50 × 10⁶ The flow is completely turbulent and the shadowgraph images reveals turbulent flow patterns randomly distributed over the flow field. Similar flow field was also visualized in the experiments

Figure A 14 and A.15 shows the velocity contours and the velocity vectors for the two values of Rayleigh number Similar turbulent behavior was also revealed from the plots. The contours were unsymmetrical showing the unsteadiness of the flow

Figure A.16, A 17 and A 18 shows the temperature contours, velocity contours and velocity vectors respectively in the longitudinal plane Similar behavior was also observed in this plane
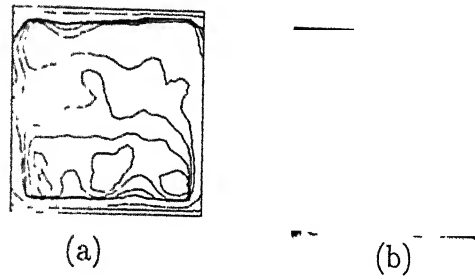
(a) (b)

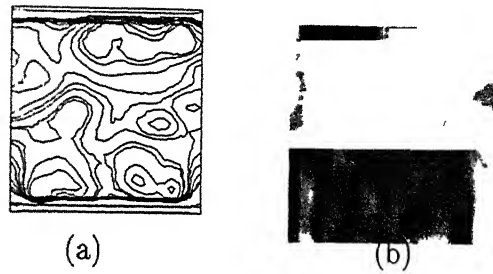Figure A 12 ΔT=1K (a)Temperature contours, (b)Numerical shadowgraph

(a) (b)

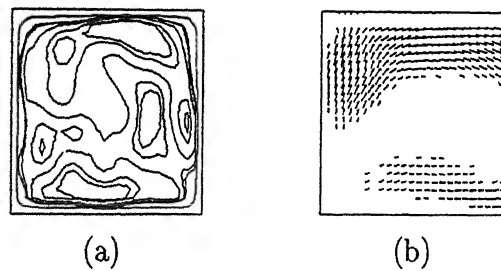Figure A 13 ΔT=10K (a)Temperature contours, (b)Numerical shadowgraph

(a) (b)

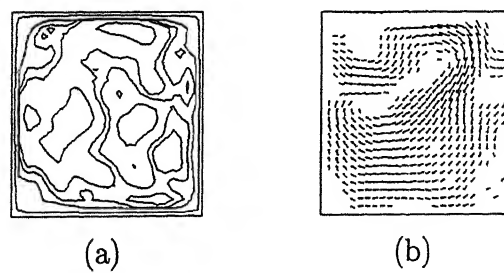Figure A 14. ΔT=1K (a)Velocity contours, (b)Velocity vectors

(a) (b)

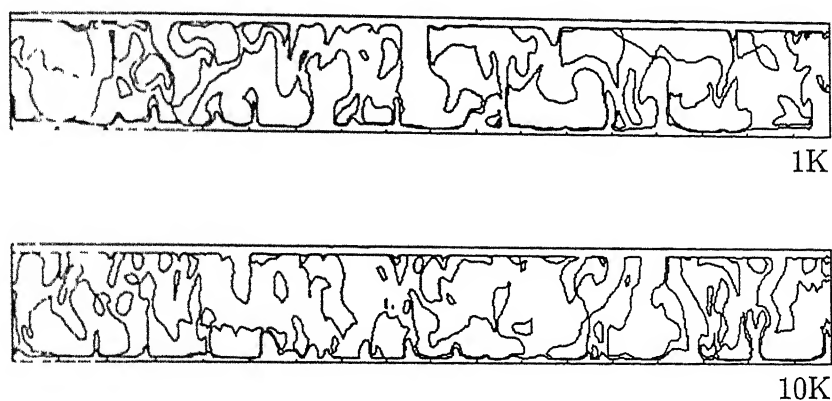Figure A 15· ΔT=10K (a)Velocity contours, (b)Velocity vectors

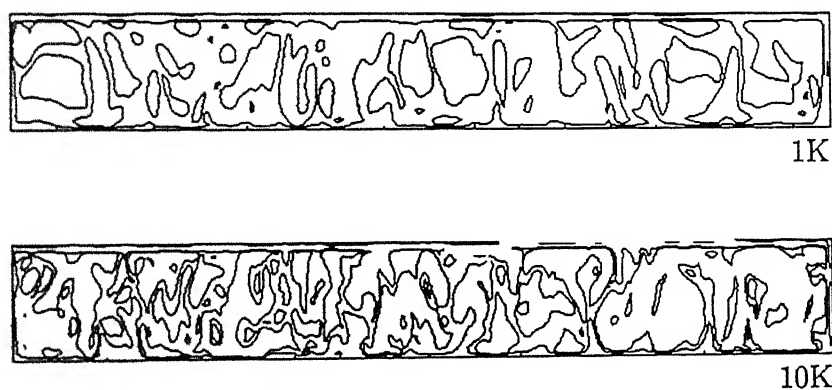Figure A 16 Temperature contours along the longitudinal plane for water

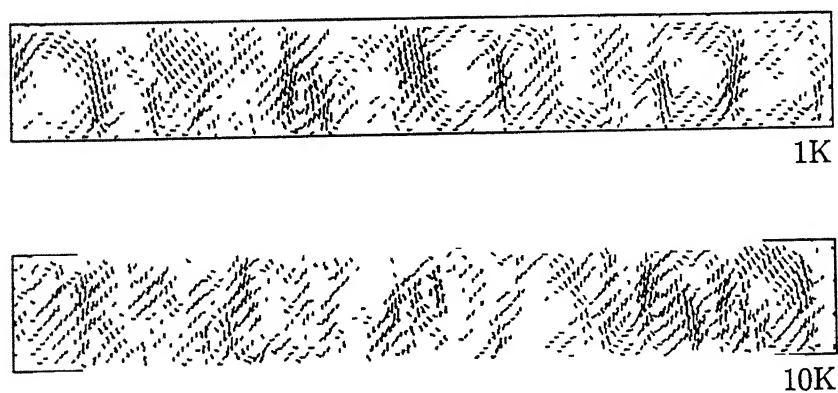Figure A.17 Velocity contours along the longitudinal plane for water

Figure A 18· Velocity vectors along the longitudinal plane for water